DISS. ETH NO. 29962

Evaluating the effect of vegetation in urban microclimate using remote sensing technologies

A thesis submitted to attain the degree of
DOCTOR OF SCIENCES
(Dr. sc. ETH Zurich)
presented by

Maria Angela Dissegna
MSc. In Geoformation and Earth Observation for Environmental Modelling and Management.
Lund University and ITC

born 10.09.1990

accepted on the recommendation of

Prof. Dr. Adrienne Grêt-Regamey, examiner
Prof. Dr. Tiangang Yin, co-examiner
Prof. Dr. Leslie Norford, co-examiner

2024

Contents

Summary

At present time, more than half of the world's population lives in cities, and many regions of the world are experiencing rapid urbanization. The increasing urbanization combined with the effects of climate change have resulted in the intensification of urban heat islands. Urban heat islands decrease outdoor thermal comfort and create feedback loops on energy consumption. Furthermore, the more frequent temperature extremes directly impact human health, particularly in the hot regions of the world.

Microclimatic models are often used to improve the understanding of the influence of the complex interactions between urban surfaces and their impact on thermal comfort. Thus contributing to guide the development of thermally comfortable cities. Increasing urban green cover is often proposed as a mitigation strategy to decrease the urban heat island effect and enhance outdoor thermal comfort. However, urban microclimatic models have not fully addressed the quantification of vegetation effects on urban climate.

The two key terms of this research are the radiative budget and the mean radiant temperature (Tmrt). The radiative budget summarizes the interaction between radiation and the urban surfaces. The radiative budget of a city is directly influenced by the complexity of the urban geometry, surface materials, direct solar radiation, incidence angle, and atmospheric diffuse radiation. It is a key parameter in the urban energy balance and urban climate models. In contrast, the Tmrt summarizes the effective radiative flux reaching a human body and is an essential human bio-meteorological parameter of thermal comfort.

Several modelling tools exist with varying levels of detail. However, limitations exist regarding data retrieval and model assimilation, particularly when addressing complex 3-D geometries and fine-scale variation of vegetation properties and the optical properties of urban surfaces. Remote sensing technologies possess great potential in improving the assessment and monitoring of the thermal behavior of cities. On the one hand, they enable the direct mapping of urban structures and their optical characteristics. On the other hand, remote sensing enables the retrieval and mapping of vegetation cover and their properties. These products constitute useful information that more advanced modelling tools could assimilate.

This work seeks to close the gaps mentioned above by adapting an advanced 3-D radiative transfer model to compute the radiative budget of any urban scenario and produce maps of mean radiant temperature distribution. This adaption is capable of providing accurate simulations of urban temperatures over existing conditions or design scenarios at different scales.

The first objective of this work was to develop a methodology to generate 3-D urban scenes from satellite data on which simulation tasks can be performed over any desired location in a city. Then, radiative budget simulations were carried out over such datasets by repurposing the Discrete Anisotropic Radiative Transfer (DART) model. This allowed to evaluate the impact of urban typology, surface material, and the effects of changing leaf area density (LAD) on the radiative budget of different urban scenarios in Singapore. The results show that highly urbanized landscapes with no tree cover can absorb radiation up to four times more than a densely vegetated "natural" landscape. Furthermore, the simulation results show good agreement when compared against net radiometer data obtained from a local flux tower in Singapore. The second objective was to develop a new method for detailed modelling and mapping of Tmrt by adapting the DART model. The adaption of the DART model enabled the precise quantification of the effects of vegetation and surface materials on the Tmrt. The method was successfully evaluated against Tmrt observations obtained from two sets of sensors mounted on a custom-made mobile platform consisting of three net radiometers, a globe thermometer, and a Vaisala weather station.

Last but not least, the third part of this research work consisted of developing a fully convolutional neural network (FCN) approach to automatically delineate individual tree crowns (ITC) over a tropical urban park using satellite and UAV hyperspectral imagery. The ITC is an essential product at the beginning of the pipeline of fine-scale vegetation assessments. This work explored the role of spatial resolution and spectral information for individual tree crown delineation tasks.

This research work highlights the importance of radiative transfer modelling as a tool for better understanding the urban heat island effect, optimizing urban design, and enhancing thermal comfort in urban areas. This knowledge is indispensable for creating sustainable, liveable, and comfortable urban environments, especially in the face of rising temperatures and the challenges posed by climate change.

Riepilogo

Attualmente, più della metà della popolazione mondiale vive nelle città e molte regioni del mondo stanno attraversando una rapida urbanizzazione. La crescente urbanizzazione combinata con gli effetti del cambiamento climatico hanno portato all'intensificazione delle isole di calore urbane. Le isole di calore urbane riducono il comfort termico esterno e creano circuiti di feedback sul consumo energetico. Inoltre, le temperature estreme più frequenti hanno un impatto diretto sulla salute umana, in particolare nelle regioni calde del mondo.

I modelli microclimatici vengono spesso utilizzati per migliorare la comprensione dell'influenza delle complesse interazioni tra superfici urbane e del loro impatto sul comfort termico. Contribuendo così a guidare lo sviluppo di città termicamente confortevoli. L'aumento della copertura verde urbana viene spesso proposto come strategia di mitigazione per ridurre l'effetto isola di calore urbana e migliorare il comfort termico esterno. Tuttavia, i modelli microclimatici urbani non hanno affrontato completamente la quantificazione degli effetti della vegetazione sul clima urbano.

I due termini chiave di questa ricerca sono il bilancio radiativo e la temperatura media radiante (Tmrt). Il bilancio radiativo riassume l'interazione tra la radiazione e le superfici urbane. Il bilancio radiativo di una città è direttamente influenzato dalla complessità della geometria urbana, dai materiali della superficie, dalla radiazione solare diretta, dall'angolo di incidenza e dalla radiazione diffusa atmosferica. È un parametro chiave nel bilancio energetico urbano e nei modelli climatici urbani. Al contrario, il Tmrt riassume l'effettivo flusso radiativo che raggiunge un corpo umano ed è un parametro biometeorologico umano essenziale del comfort termico.

Esistono diversi strumenti di modellazione con diversi livelli di dettaglio. Tuttavia, esistono limitazioni per quanto riguarda il recupero dei dati e l'assimilazione dei modelli, in particolare quando si affrontano geometrie 3D complesse e variazioni su scala fine delle proprietà della vegetazione e delle proprietà ottiche delle superfici urbane. Le tecnologie di telerilevamento possiedono un grande potenziale per migliorare la valutazione e il monitoraggio del comportamento termico delle città. Da un lato consentono la mappatura diretta delle strutture urbane e delle loro caratteristiche ottiche. D'altro canto, il telerilevamento consente il recupero e la mappatura della copertura vegetale e delle sue proprietà. Questi prodotti costituiscono informazioni utili che strumenti di modellazione più avanzati potrebbero assimilare.

Questo lavoro cerca di colmare le lacune sopra menzionate adattando un modello avanzato di trasferimento radiativo 3-D per calcolare il bilancio radiativo di qualsiasi scenario urbano e produrre mappe della distribuzione media della temperatura radiante. Questo adattamento è in grado di fornire simulazioni accurate delle temperature urbane rispetto alle condizioni esistenti o scenari di progettazione a diverse scale.

Il primo obiettivo di questo lavoro era sviluppare una metodologia per generare scene urbane 3D da dati satellitari su cui è possibile eseguire attività di simulazione su qualsiasi posizione desiderata in una città. Quindi, sono state effettuate simulazioni del budget radiativo su tali set di dati riproponendo il modello DART (Discrete Anisotropic Radiative Transfer). Ciò ha permesso di valutare l'impatto della tipologia urbana, del materiale di superficie e gli effetti del cambiamento della densità dell'area fogliare (LAD) sul bilancio radiativo di diversi scenari urbani a Singapore. I risultati mostrano che i paesaggi altamente urbanizzati senza copertura arborea possono assorbire le radiazioni fino a quattro volte di più di un paesaggio "naturale" densamente vegetato. Inoltre, i risultati della simulazione mostrano un buon accordo se confrontati con i dati del radiometro netto ottenuti da una torre di flusso locale a

Singapore. Il secondo obiettivo era sviluppare un nuovo metodo per la modellazione e la mappatura dettagliata di Tmrt adattando il modello DART. L'adattamento del modello DART ha consentito la quantificazione dettagliata degli effetti della vegetazione e dei materiali di superficie sul Tmrt. Il metodo è stato valutato con successo rispetto alle osservazioni Tmrt ottenute da due serie di sensori montati su una piattaforma mobile su misura composta da tre radiometri netti, un globotermometro e una stazione meteorologica Vaisala.

Ultimo ma non meno importante, la terza parte di questo lavoro di ricerca consisteva nello sviluppo di un approccio di rete neurale completamente convoluzionale (FCN) per delineare automaticamente le chiome individuali degli alberi (ITC) su un parco urbano tropicale utilizzando immagini iperspettrali satellitari e UAV. L'ITC è un prodotto essenziale all'inizio del percorso di valutazioni della vegetazione su scala fine. Questo lavoro ha esplorato il ruolo della risoluzione spaziale e delle informazioni spettrali per le attività di delineazione delle chiome degli alberi individuali.

Questo lavoro di ricerca evidenzia l'importanza della modellazione del trasferimento radiativo come strumento per una migliore comprensione dell'effetto isola di calore urbano, ottimizzando la progettazione urbana e migliorando il comfort termico nelle aree urbane. Questa conoscenza è indispensabile per creare ambienti urbani sostenibili, vivibili e confortevoli, soprattutto di fronte all'aumento delle temperature e alle sfide poste dai cambiamenti climatici.

ACKNOWLEDGEMENTS

I want to take this opportunity to thank my family, partner, and friends for the amazing moments together during my PhD years. Their support, contact, visits to Singapore, and adventures together made this experience unique and wonderful. I am glad you all were part of my life in person and the distance during this journey.

Special thanks to Prof. Adrienne Grêt-Regamey for giving me the opportunity to pursue this degree. Her support, motivating attitude, and patience during the entire duration of my PhD were key for me to continue pursuing the goal, particularly during the hard times. Thank you for allowing me to explore different directions and giving me space to develop myself independently. Thanks for providing me with all the necessary tools, advice, discussions, and constructive criticism, these interactions made me grow not only academically but also professionally and as a person.

I am deeply thankful to Dr. Tiangang Yin for his continuous scientific guidance through my research and the opportunity to take part in his project in SMART, I am grateful for meeting his group, the discussions, and the interesting insights I gained from the project. Special thanks to Dr. Shanshan Wei, since the day we met, you have constantly motivated me to keep going. Thank you immensely for sharing your knowledge and the constructive guidance and support on the different projects during my PhD.

I am happy to have embarked on this journey together with the vibrant SEC community, particularly special thanks to all the members of my research group, whose positive and friendly attitude made the day-by-day a beautiful experience. Thank you, Philipp, Naika, Omer, Wu Hao, Tze Kwan, Xiao Ping, Rachel, and Clifford for the discussions, knowledge exchange, and collaborations we made. Thanks to Zuzana for the unconditional support and motivation you brought to the group, it has been a pleasure working with you all.

Last but not least, I would like to thank collaborators Prof. Jean-Philippe Gastellu, Dr. Nicolas Laurent, and the DART team of CESBIO for their consistent support of the DART model. Prof. Wong and Dr. Martin (NUS) for providing net radiometer sensors. Prof. Matthias Roth and Dr. Erik Velasco for providing initial net radiometer data. Dr. Juan Angel Acero from SMART for providing meteorological sensors. Professor Andrew Whittle (SMART), Dr. Genevive Ow, and Dr. Lockman (NParks) for granting access to carry out fieldwork in Bishan Park and allowing the usage of the UAV equipment and access to their lab. Thanks to Yuan Bo, Vivek, Sun, and Elliot for the time we shared in the lab and the field.

Funding: This research was conducted at the Future Cities Laboratory at the Singapore-ETH Centre, which was established collaboratively between ETH Zurich and Singapore's National Research Foundation (FI370074016) under its Campus for Research Excellence and Technological Enterprise programme.

1. Introduction

1.1. Motivation

In recent years, urban areas are increasingly experiencing elevated temperatures and heat waves due to urbanization and climate change [1]. The length, frequency, and intensity of heat waves are expected to rise in the future, exacerbating the already poor air quality of densely populated cities, increasing health risks of vulnerable population groups, affecting the thermal comfort of urban residents, and raising the demand of energy for cooling systems [1][2][3][4]. An often-discussed climatic phenomenon in urban areas is the Urban Heat Island effect (UHI), characterized by higher air and surface temperatures in urban settlements compared to their surrounding countryside [5]. The UHI effect can perturb the body's innate cooling mechanisms and amplify the vulnerability to heat-related ailments. This is particularly true for at-risk populations such as the elderly, children, and individuals with pre-existing health conditions. Individuals are more susceptible to experiencing discomfort and stress when subjected to increased temperatures, especially when coupled with elevated humidity levels.

Effective urban planning that considers land use, building design, energy consumption, and transportation systems can create more comfortable and climate-resilient urban environments. Informed adaptation strategies against urban heat are also needed to guarantee the well-being of urban residents. Some strategies include the incorporation of urban greenery, such as parks, trees, and green roofs, by providing shading, evaporative cooling, and reducing heat absorption. Other technologies, such as cool roofing and cool pavement, can help to reflect more sunlight and absorb less heat, thus lowering surface temperatures in urban areas. Furthermore, designing well-ventilated, pedestrian-friendly urban spaces can improve air circulation and reduce heat accumulation. With cities growing larger and denser, it is crucial to understand these strategies' role in enhancing the livability and resilience of urban spaces.

Examining the role of such interventions in increasing thermal comfort contributes to the development of thermally comfortable urban spaces. To do so, a detailed understanding of the influence of the complex radiation interactions between the built environment and vegetation at the building, neighborhood, and city scales is required [6]. Modelling tools are often used to simulate these complex interactions and to assess their impact on urban microclimate.

Radiative transfer models are mathematical and computational techniques to predict how radiation, such as visible light, infrared, or ultraviolet radiation, interacts and propagates with a medium. In climate science, radiative transfer models are used to simulate the flow and transport of solar and thermal radiation within the Earth's atmosphere and its interactions with the Earth's surface, clouds, aerosols, and greenhouse gases. These models are essential tools for understanding the Earth's energy balance, quantifying the impact of various climate drivers, and predicting future climate scenarios. These models contribute to our ability to assess climate change, inform climate policy decisions, and develop strategies for mitigating and adapting to global warming. Another use of radiative transfer modelling is for satellite-based remote sensing applications to interpret measurements of radiation emitted or scattered by the Earth and its atmosphere. These models help retrieve information about atmospheric temperature, humidity, and cloud properties; as well as mapping the Earth's surface.

The increasing availability and affordability of earth observation data, the advancement of process-based models, and ever-growing computation power open up new possibilities for more detailed modelling of environmental parameters in urban areas. In this context, remote sensing technologies possess great potential in improving the assessment and monitoring of the thermal behavior of cities through the direct mapping of urban surfaces and vegetation at an increasing level of detail; and through the repurpose and adaption of simulation tools such as radiative transfer modelling for a more in-depth analysis of radiative fluxes in urban areas.

The broad scope of this thesis is to explore two technical fields that can assist in the assessment of the current state and to evaluate strategies as part of the climate-responsive design process: 1) remote sensing technologies, such as satellite imagery and aerial photography, for instance, used for the retrieval of Earth's surface properties; and 2) radiative transfer modelling to simulate the interaction of radiation with urban surfaces and its impact on thermal comfort under different scenarios and urban design strategies.

Urban greenery, such as trees and other types of vegetation, not only provides local cooling via shading and evapotranspiration [7][8]; but also supplies additional ecosystem services such as rain runoff reduction [9], improving the air quality, providing habitats for flora and fauna and enhancing the aesthetics and value of urban areas [10]. This is why monitoring the status of urban trees is of great importance to understand the mutual influences between urban vegetation, anthropogenic activities, and regional climate change. Government agencies could benefit from using science-based tools to assist in the urban planning process and the management of urban vegetation. For instance, Singapore's National Parks Board (NParks) is responsible for managing more than seven million planted trees [11]. The current management practice involves annual inspections by park surveyors to maintain information on species diversity, tree health, and ecosystem service. Therefore, the deployment of automated monitoring approaches is highly valued, and the demand for such systems is expected to grow. In this framework, quantitative remote sensing technology plays an important role in parameterizing urban trees in terms of biophysical, biochemical, and physiological variables, from which indicators of tree health can derived. Furthermore, the possibility of linking fine-scale observations obtained from unmanned aerial vehicles to satellite observations opens up opportunities for scalability.

To summarize, this thesis aims to enhance the understanding of the benefits vegetation brings to urban areas in terms of thermal comfort through the use of data and tools that belong to the field of remote sensing. Particularly, this work evolved around two main topics: 1) the creation of datasets containing detailed information on urban form and vegetation and 2) the suitability of repurposing the advanced 3-D radiative transfer model (DART) to perform radiative budget and mean radiant temperature simulations over 3-D urban scenarios.

1.2. Description of the projects

This thesis was carried out within the project "Ecosystem Services in Urban Landscapes" of the "Future Cities Laboratory" at the Singapore-ETH Centre and the project "Remote Sensing for Urban Tree Management: Species Classification and Health Monitoring" of the Singapore-MIT Alliance for Research and Technology (SMART) and the National Parks Board (NParks), Singapore.

The project "Ecosystem Services in Urban Landscapes" aimed at understanding how we can improve the ecological performance of urban greenery through landscape design by exploring new types of data and modelling approaches. Physical, ecological, and socio-cultural parameters were used as inputs to model various types of ecosystem services. Landscape design was performed using 3-D point-cloud data to represent existing landscapes accurately. The iterative process of model simulation and design feedback provides opportunities to improve designs based on scientific results [12][13][14]. In this context, the contribution of this work towards the project was in 1) the creation of a 3-D database of buildings and vegetation for the entire city of Singapore so that simulations can be run in any desired location and 2) the implementation of two modelling approaches capable of assimilating detailed 3-D information on both vegetation and urban surfaces. This method provides maps of the radiative budget and mean radiant temperature, which are then combined with other model outputs such as wind simulations, humidity, and air temperature to assess the performance of the current situation and proposed scenarios as part of a design loop.

The project "Remote Sensing for Urban Tree Management: Species Classification and Health Monitoring" worked towards a computerized management of urban trees based on remote sensing information. While high spatial and spectral resolutions of UAV-based hyperspectral imaging provide unique opportunities for vegetation modelling and properties' retrieval at the local scale, satellite imagery could be the ultimate data source for regular surveys over larger areas in Singapore. This project used a hyperspectral UAV-based imaging system to build computational models of individual trees' biophysical, biochemical, and physiological properties. Radiative transfer modelling was used to establish a linkage between observations at leaf, canopy, and landscape scales. Ultimately, this enabled the retrieval of key variables for individual-tree health monitoring that can ultimately be observed from satellite imagery. The contribution of the work towards the project presented in this thesis was the development of a fully convolutional neural network (FCN) approach to delineate individual tree crowns over mixed tropical vegetation automatically. The individual tree crown (ITC) delineation is a product at the beginning of the pipeline of advanced vegetation monitoring approaches at the scale of individual trees.

1.3. State of the Art

Urban Heat Island and Thermal Comfort

UHI is the condition where urban areas experience consistently higher air and surface temperatures than the surrounding countryside. They are primarily a consequence of urbanization and the alteration of natural land cover into impervious surfaces such as concrete, asphalt, and buildings. These surfaces absorb and store heat during the day and release it slowly at night, leading to elevated night-time temperatures [5]. UHIs result from the complex interactions between the urban land surfaces and the atmosphere. These interactions are directly influenced by (1) the reduction of vegetation cover, (2) high storm-water runoff from impervious surfaces which reduces soil moisture and evapotranspiration, (3) urban materials with high heat capacity which retain heat and slowly release this at night, (4) low albedo urban materials that absorb large amounts of solar radiation; (5) complex urban geometries that absorb and trap heat, and (6) increased human activities in urban areas, such as transportation, industrial processes, and energy consumption, release heat into the environment. Furthermore, the density and design of buildings can trap heat, creating canyon-like structures that hinder air circulation and exacerbate the UHI effect [2][5,15].

Two important concepts concerning the study of the radiative behavior of a city are (1) *The radiative budget (RB),* which is a key parameter in the urban energy balance and urban climate models. It summarizes the interaction between radiation and the urban surfaces and is directly related to the UHI effect; and (2) *The mean radiant temperature (Tmrt*), an important human biometeorological parameter of thermal comfort, which summarizes all short wave and long wave radiation fluxes reaching a human body. Tmrt varies temporally and spatially in cities, as it is directly influenced by urban geometry, surface materials, vegetation, solar incident angle, and atmospheric diffuse radiation.

The increased urbanization and climate change experienced particularly in tropical cities affects directly and indirectly the thermal comfort and health of urban residents. Thermal comfort is a vital aspect of urban living, influencing the overall well-being of residents. It refers to the condition where people feel satisfied with their thermal environment. Achieving thermal comfort is essential for health, productivity, and quality of life. High temperatures in UHIs can lead to heat-related illnesses, such as heatstroke and dehydration, especially among vulnerable populations like the elderly and young children. Unbearable heat can make outdoor activities unpleasant and limit the use of public spaces, reducing social interaction and community well-being [16]. To cope with extreme heat, residents often rely on air conditioning, which increases energy consumption and greenhouse gas emissions,

contributing to further warming. To ensure the welfare of city dwellers, it is essential to implement informed strategies to combat urban heat. These strategies for instance encompass integrating green elements into the urban landscape, like parks, trees, and green roofs, to offer shade, and minimize heat absorption [17].

Urban Design and Modelling

Urban design has a significant influence on minimizing heat production and retention by urban surfaces and structures. For instance, the increase in vegetation cover and the use of solar reflective materials influence radiative fluxes and, therefore, can be a good strategy to improve outdoor thermal comfort by means of reducing Tmrt and thus, reducing the UHI effect [21–25]. Mitigation strategies for UHI are essential for improving thermal comfort, safeguarding public health, and promoting overall urban sustainability [18]. These strategies require a multifaceted approach encompassing a wide range of interventions; from green infrastructure and sustainable building design to community engagement and public transportation improvements. To expand on these, urban planning should prioritize the creation and preservation of green spaces, parks, and urban forests. These areas provide shade and promote cooling through evapotranspiration. The use of cool roofing materials and reflective pavements can reduce heat absorption and lower surface temperatures. Furthermore, architects and engineers can adopt energy-efficient building designs that incorporate natural ventilation, shading devices, and green roofs to reduce indoor temperatures and energy consumption [19]. Expanding and improving public transportation networks can reduce the number of private vehicles on the road, thereby decreasing heat emissions and air pollution [20]. Finally, educating and involving communities in UHI mitigation efforts can lead to the implementation of local cooling strategies [20].

Analyzing how mitigation increases thermal comfort helps to guide the development of thermally comfortable cities. In this context, simulation tools play a critical role in evaluating and optimizing various aspects of urban design to achieve sustainability goals. A variety of studies and models investigating heat mitigation strategies at the mesoscale exist. However, most leave out significant complexities that occur at the microscale, directly related to thermal comfort [21]. Existing radiation transfer models such as those used in ENVIMET [22], VTUF-3D (TEB) [6], and SOLWEIG [23], etc., have limitations in terms of characterization of vegetation and/or their modelling of radiative fluxes. Such models account for vegetation in a simplistic way and/or use a simplified parameterization of the vegetation properties. For instance, some estimate Tmrt in terms of the shade of an opaque object [24]. This does not capture vegetation's structural and biophysical complexity, which allows some radiation to pass through gaps in the canopy. Moreover, neglecting the 3-D structure of vegetation canopies can lead to errors in the radiation budget. Efficient models must account for the 3-D nature of the scenes [24]. To improve on this simple treatment of vegetation, several authors have suggested including detailed structural information and biophysical parameters of the tree canopy (e.g., Leaf Area Index [LAI] and Leave Angle Distribution [LAD]) [24]. Furthermore, existing modelling packages usually simplistically treat radiation as the description of surface optical properties relies only on a few simplified parameters such as albedo and emissivity. As a result, the detailed properties of radiation ranging over the short-wave and long-wave spectrum are not properly simulated.

One of the most comprehensive physically based 3-D radiative transfer models from ultraviolet to thermal infrared spectral domain is the Discrete Anisotropic Radiative Transfer model (DART) [25–27] [28]. The main advantages of using DART to model radiation transfer compared to other models are the fine treatment of radiation with a spectral domain that extends from ultraviolet to thermal infrared; simulation of broadband as weighted integration of narrow bands; versatility in terms of simulation inputs such as all types of surface optical properties, including isotropic property (Lambertian) or anisotropic property (specular, or predefined bidirectional reflectance distribution function), which extends the applications to all different materials; and the capability to simulate vegetation as a turbid

medium defined by biophysical properties such as leaf area density, leaf angle distribution, and clumping function [24]. Despite the potential capabilities for in-depth analysis of the radiative behavior of urban areas, the DART model has not yet been used to evaluate the radiative budget of different urban configurations or as a mapping and predictive tool of micrometeorological parameters such as the mean radiant temperature.

Remote Sensing Tools

Remote sensing represents a comprehensive source of spatio-temporal information on the physical parameters of the planet's surfaces. Such technologies have been applied in urban studies at different scales, allowing the establishment of links between ecological, physical, and social processes in a geographically explicit manner. Remote sensing technologies that are relevant for mapping and the environmental modelling of urban areas can therefore be best classified in terms of carrier platform:

a. Spaceborne: On one hand, open satellite data from NASA's Earth Observing System (e.g. MODIS, LANDSAT) and the ESA's Operational EO Missions (e.g. Sentinel) focus on global monitoring of the Earth's surfaces with multiple spectral bands with relatively low spatial resolution. On the other hand, commercial companies (e.g. Digital Globe) developed very high-resolution satellite platforms with broadband configuration. The spatial sampling can be up to 0.28 m for the latest WorldView-4 satellite. The spectral domain is relatively limited, but high spatial resolution allows users to retrieve information about single buildings and trees in an urban environment. In addition, the stereo satellite acquisition (also available in Worldview missions) enables retrieval of digital surface models with sub-meter accuracy. These data are commercially available.
b. Airborne: Compared with satellites, aircraft platforms have more flexibility to conduct time-series research with high resolution. Hyperspectral airborne devices can provide more than 200 spectral measurements with sub-meter spatial sampling. The Aerial Laser Scanner (ALS) can create a 3-D point cloud with up to 20 points per square meter. These data have been used in many scientific, design, and architecture applications [13]. However, flying an aircraft is expensive and raises security concerns in data sharing. Usually, government agencies may have these data, but they are challenging to acquire, even for research and education purposes.

c. UAV platforms: Unmanned aerial vehicle (UAV) platforms with lightweight hyperspectral and LiDAR sensors provide a more affordable alternative for detailed data collection due to low altitude measurements compared to conventional aircraft. Even though the flight time and covered area per flight are considerably smaller, UAVs can be used for local-scale monitoring of crops, forests, and other landscapes of interest. They can complement studies using conventional remote sensing platforms. UAV hyperspectral sensors have been used to retrieve plant biophysical and biochemical indicators [29,30] which are useful in the assessment of vegetation health and disease monitoring [31], vegetation water stress [32][33], plant vigor [34], biomass estimation [35,36]. Additional applications are wildfire detection [37], plant species classification [38–40], and forest preservation and management operations [41].
d. Terrestrial: Terrestrial measurements provide the most accurate data with flexible and mobile configurations. However, they can only provide in-situ measurement on a selected site instead of data acquisition over the whole city. Field measurements from instruments like LAI-2200 from LI-COR Biosciences and TLS are commonly used to validate remote sensing data [42]. TLS receives thousands to millions of points with sub-centimeter footprint size, allowing it to derive biophysical indicators and reconstruct single trees as an object or turbid medium format.

The remote sensing of vegetation is characterized by special requirements and challenges, such as the often complex acquisition of reference data and the subsequent understanding of the vegetation-

specific radiative transfer, the resulting sensor-specific electromagnetic signals, and their dynamics across the phenology. Biophysical indicators such as Leaf Area Index (LAI) and canopy spread are required to obtain realistic radiative transfer simulations at fine scales [43]. The 3-D distribution of plant material is a key parameter that can be analyzed to describe the vegetation structure, which influences several processes, such as radiation interception and ecosystem functioning [43]. Recent uses of TLS focus on the reconstruction of 3-D tree models [44], the retrieval of biophysical indicators such as LAI, foliage and density distribution [45][42][46], structural traits including height, biomass, life form, crown morphology, canopy cover, canopy roughness [47][29][48] and on determining the cooling effect of tree canopy [49].

The retrieval of vegetation traits from imagery is often done through hybrid modelling. A hybrid retrieval scheme relies on the use of physically based radiative transfer models for the forward simulation of a set of spectral responses as a function of the model input variables and on the use of machine learning regression algorithms to learn the relationships between the simulated spectra and the model input variables [50][51]. The most common approach is to train models using simulated datasets, to be then applied to the actual spectral data for estimating the traits of interest. Harnessing remote sensing data for vegetation assessments and monitoring requires efficient, accurate, and flexible analytical methods. For this reason, the radiation transfer models used in remote sensing were developed to compute radiation precisely in narrow or broad spectral domains, because such precision is highly important to inverting and evaluating existing data and to prepare future satellite missions [26].

Not many remote sensing products readily exist for fine-scale analysis, such as individual tree scale over tropical vegetation. One of the basic parameters in fine-scale vegetation studies is the ITC delineation. However, automatic methods for ITC delineation often fail in conditions of dense and mixed vegetation, which is the case in Singapore. There is a need for novel approaches to retrieve this information over a tropical urban park.

1.4. Summary of the research gaps and research questions

As presented in the previous section, new approaches are needed to gain a more in-depth understanding of the effects of vegetation in the urban microclimate. The current state of urban microclimate modelling has several limitations, for instance, in the representation/parametrization of vegetation in the existing modelling tools. This simplification makes current models not entirely suited to investigate and predict the complex interactions and feedback between vegetation and surrounding urban surfaces. Thus limiting their predictive ability to quantify the impact of vegetation in the urban microclimate. Which, in turn, is needed to assess vegetation as a potential mitigation strategy. Advanced radiative transfer models can handle detailed 3-D representations of vegetation together with their biophysical and biochemical properties. However, the potential of adapting the advanced 3-D radiative transfer model "DART" to carry out simulations of Tmrt has not been previously explored. Furthermore, remote sensing technologies possess great potential for the retrieval of detailed vegetation characteristics, as well as the creation of detailed 3-D urban datasets. This information could then be used as input on simulation tools and urban climate models. However, remote sensing products for fine-scale analysis, such as individual-tree-scale assessments, over tropical vegetation are limited. This is primarily due to the complexity of tropical ecosystems, the dense canopy cover, and the challenges associated with high spatial resolution imagery. Particularly, this thesis work seeks to tackle the following gaps:

- The impacts of vegetation and built environment on the radiative budget and Tmrt have not been thoroughly addressed by existing models. Simulation tools used for mapping Tmrt need more accurate consideration of the surface properties and 3-D structure of both vegetation and the built environment.

- There is a need for novel methodologies for retrieving 3-D data of urban structures and vegetation from remote sensing data.

- There is a need for an automatic method for individual tree crown delineation for images of dense and mixed vegetation.

To bridge such gaps, progress in three key research areas is needed: 1) the implementation of more accurate radiative transfer modelling approaches for urban microclimate studies, particularly for radiative budget and Tmrt simulations; 2) the generation of 3-D representations of urban areas that enable detailed modelling of physical and optical properties of urban materials and vegetation; and 3) new methods for the retrieval of biophysical properties of vegetation at the fine scale. In relation to the identified gaps and the respective key research areas, this thesis work has evolved with the intention of answering the following research questions:

- **What is the impact of varying vegetation properties, urban geometry, and surface optical properties on the Tmrt?**

Hypothesis: The type, density, and health of vegetation within an urban area can significantly impact Tmrt. More extensive and healthy vegetation, such as trees and green spaces, provide shading, thus, reducing Tmrt. Conversely, sparse or stressed vegetation may lead to higher Tmrt as they offer less "cooling" effect [52][53][54]. The layout of buildings, streets, and other structures affects the absorption and reflection of solar radiation [55]. Well-planned urban designs and the appropriate selection of construction materials can substantially reduce the Tmrt [56].

- **How can we effectively model the radiative budget in urban environments across various scales while accounting for the diverse optical and geometric characteristics of vegetation and buildings?**

Hypothesis: Effectively modelling the radiative budget in urban environments requires a combination of data-driven analysis and scenario testing. Advanced radiative transfer models can handle detailed 3-D representations of an urban environment [57]. By doing so, fine-scale variation of surface materials and vegetation properties of an urban scene can be quantified by computing their radiative budget. These 3-D radiative budget outputs can be further adapted to compute mean radiant temperature, enabling the evaluation of the impact of different vegetation types, tree species, and their distribution on both the radiative budget and mean radiant temperature at various scales.

- **To what extent deep learning methods can assist in the instance segmentation of individual trees in a dense and mixed urban park?**

Hypothesis: Deep learning can easily segment trees from the background and even differentiate tree species [58], but identifying and delineating individual trees is a challenging task. Evaluating a new algorithm over different spatial and spectral resolutions could improve the automatic delineation of individual tree crowns of a tropical urban park.

1.5. Cumulative Doctoral Thesis

The research questions are tackled in chapters two, three, and four, respectively, with each chapter containing a thorough description of the applied methodology, a detailed overview of the results, and a comprehensive discussion of the findings. The following section summarizes the content found in each of the subsequent chapters.

Chapter two presents a methodology to produce the data source to run radiative transfer simulations and other modelling tasks at any desired location in a city. First, the method to obtain a detailed 3-D model of Singapore, including buildings and vegetation from commercial and open satellite imagery, is described. Then, the 3-D Discrete Anisotropic Radiative Transfer (DART) model is repurposed to estimate the radiation absorbed by the urban surfaces accounting for the presence of vegetation cover and changing Leaf Area Density (LAD) conditions. Different urban typologies were extracted and evaluated in terms of radiative budget. Finally, an overview of the sensitivity of the radiative budget to changes in LAD and varying ground cover materials is explored. This chapter highlights the potential of using the DART model for detailed 3-D radiation transfer simulations at different scales, opening opportunities for more in-depth treatment of radiation in future urban simulation tasks.

Chapter three introduces a new method to produce detailed modelling and mapping of Tmrt distribution in urban landscapes using the DART model. This new approach can simulate Tmrt at different scales and under a range of parameters, including the urban pattern, surface material of ground, walls, roofs, and properties of the vegetation (coverage, shape, spectral signature, Leaf Area Index, and Leaf Area Density). The main advantages of this method are the fine treatment of radiation in both short-wave and long-wave domains, the detailed specification of optical properties of urban surface materials and vegetation, a precise representation of the vegetation component, and the capability to assimilate 3-D inputs derived from multisource remote sensing data. A first evaluation of the method was performed in Singapore by comparing simulated Tmrt vs field observations from a custom-made microclimatic measurement platform.

Remote sensing-based approaches for urban vegetation monitoring and management require information on biophysical and biochemical properties at the individual tree scale. This information is also required in fine-scale simulation tasks. The identification and delineation of individual tree crowns is a product of high relevance, which comes at the beginning of the data processing pipeline. Chapter four evaluates the performance of a proposed fully convolutional neural network (FCNN) approach to automatically delineate ITC's over a tropical urban park using satellite and UAV hyperspectral imagery. The role of spatial resolution and spectral information in individual tree crown delineation tasks was explored.

This thesis incorporates the following articles that have been published or submitted for publication in peer-reviewed journals:

- **3-D Reconstruction of an Urban Landscape to Assess the Influence of Vegetation in the Radiative Budget.**
  Dissegna, M.A.; Yin, T.; Wei, S.; Richards, D.; Grêt-Regamey, A. *Forests* **2019**.

- **Modelling Mean Radiant Temperature Distribution in Urban Landscapes Using DART.**
  Dissegna, M.A.; Yin, T.; Wu, H.; Lauret, N.; Wei, S.; Gastellu-Etchegorry, J.P.; Grêt-Regamey, A. *Remote. Sens*. **2021**

- **Automatic delineation of individual tree crowns in a tropical urban park: assessment of a new deep learning algorithm over different spectral and spatial resolutions.**
  Dissegna, M.A.; Wei, S.; Atlason, H.E.; Yin, T.; Grêt-Regamey, A. *IEEE Journal of Selected Topics in Applied Earth Observations and Remote Sensing. Submitted (**2024**).*

Additional articles elaborated during this research work that are not part of the cumulative thesis:

- **An assessment study of three indirect methods for estimating leaf area density and leaf area index of individual trees.**
  Wei, S.; Yin, T.; Dissegna, M.A.; Whittle, A.J.; Ow, G.L.F.; Yusof, M.L.M.; Lauret, N.; Gastellu-Etchegorry, J.P. *Agric. For. Meteorol.* **2020**

- **Point cloud modelling as a bridge between landscape design and planning.**
  Urech, P.R.W.; Dissegna, M.A.; Girot, C.; Grêt-Regamey, A. *Landsc. Urban Plan.* **2020.**

- **How urban densification influences ecosystem services - A comparison between a temperate and a tropical city.**
  Grêt-Regamey, A.; Galleguillos-Torres, M; Dissegna, M.A.; Weibel, B. Environ. Res. Lett. **2020**.

1.6. Study areas

The research was conducted in three case study areas across Singapore, a city of 5.8 million inhabitants experiencing UHI and seeking to enhance outdoor thermal comfort. Singapore has a tropical, humid climate with no distinctive seasons. Near-surface air temperature usually ranges from 23 °C to 32 °C. The vegetation is dense, diverse, fast-changing, and often heavily managed. The three study areas are (1) the Bedok Planning Area (indicated in blue on Image 1), (2) The "Cantonment Towers" located in the Tanjong Pagar district (yellow), and (3) the Bishan-Ang Mo Kio urban park (red).

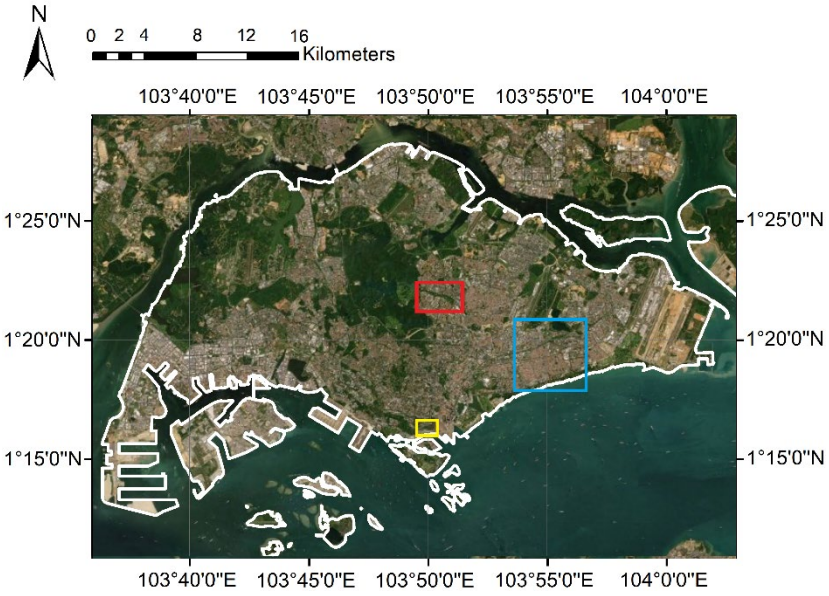

Image 1.

Bedok is a planning area located along the south-eastern coast of Singapore, covering a land area of 21.69 km2. It is home to approximately 280,000 residents [59]. The different urban typologies found in Bedok include residential low rise, industrial low rise, social housing medium rise, residential high rise, and secondary forest. Bedok planning area was selected due to the historical location of a micrometeorological flux tower in the Telok Kurau neighborhood [60]. Upwelling and downwelling shortwave radiation data obtained from this tower was used for model validation of radiative budget simulations in chapter two.

Tanjong Pagar District is located in southern Singapore within the Central Business District. Although Tanjong Pagar is part of the major financial center and showcases a high skyline, this area is also home to shophouses, condominiums, and government-built apartments, both old and new. The Tanjong

Pagar area has been an important focal point for Asia thanks to the Tanjong Pagar port, considered one of the world's busiest trans-shipment hubs. Future urban expansion plans over this area will occur from 2027, just after the port is transferred to the Tuas Megaport. Several design scenarios have been proposed and evaluated using a "design loop" approach in the Ecosystem services in urban landscapes project [12]. Within Tanjong Pagar are the "Cantonment Towers," a modern social housing complex with a playground built in 2000. The high-density housing blocks have 30 floors, resulting in a building height of 94 m surrounding the playground. This playground was chosen to collect bio-meteorological data using a customized mobile station consisting of three net radiometers oriented in six directions, a globe thermometer, a Vaisala sensor recording wind speed, wind direction, humidity, air temperature, and precipitation, and a Kestrel sensor. This information was used for model evaluation of mean radiant temperature simulations in chapter three.

Constructed in 1988, the **Bishan-Ang Mo Kio Park** is a 62-hectare tropical urban park in central Singapore on which the Kallang River flows (Image 2, top). The park showcases a water-sensitive urban design managing rainwater sustainably (Image 2, Bottom left). Aiming at catering to the increased rainwater runoff from the catchment due to urbanization, the river was transformed in 2006 from a linear utilitarian concrete drainage channel into a meandering, natural river flowing through the park in the form of a flat riverbed. Several soil bioengineering techniques and a wide variety of tropical plant species were applied along a length of 60 meters at one of the side drains in the park to stabilize the river banks and prevent erosion. These techniques included fascines, rip-rap with cuttings, geotextile-wrapped soil lifts, brush mattresses with fascines, reed rolls, planted gabions, and geotextile with plantings. In the upstream of the park, a cleansing biotope helps maintain the ponds' water quality. Additionally, carefully selected plants in a filter medium help to cleanse the water by retaining pollutants and absorbing nutrients. These, together with an ultraviolet (UV) treatment, eliminate any harmful biological contaminant without introducing chemicals into the water [61][62]. The most prominent tree species planted across Bishan Park are Samanea Saman, Tabebuia Rosea, Khaya Senegalensis, Peltophorum Pterocarpum, Pterocarpus indicus, and Syzysium grande. Overall, the vegetation of the park is heavily managed. The park's east side was selected to carry out a series of aerial surveys using a hyperspectral imaging sensor (Image 2, Bottom right).

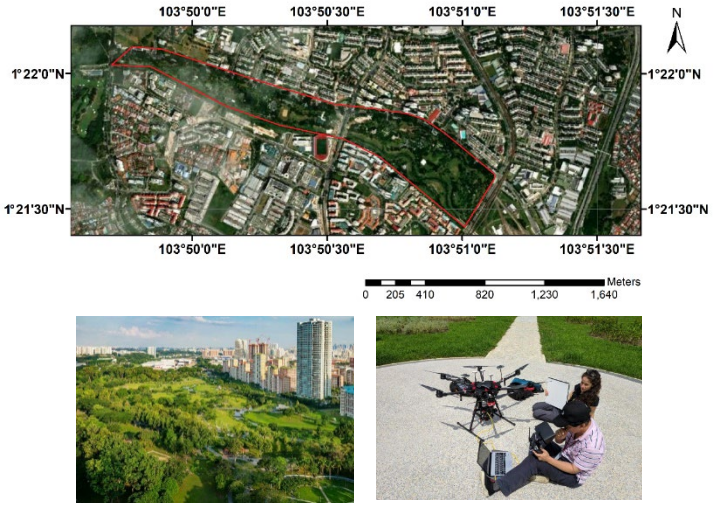

Image 2. A) Location and extent of Bishan Park. B) Aerial view of Bishan Park. Image by Ramboll Studio Dreiseiti Singapore. C) Preparations for aerial survey over Bishan Park.

2. Three Dimensional Reconstruction of an Urban Landscape to Assess the Influence of Vegetation in the Radiative Budget

Maria Angela Dissegna[1], Tiangang Yin [2], Shanshan Wei [3], Dan Richards[1] and Adrienne Grêt-Regamey[4]

[1] Future Cities Laboratory, Singapore ETH Center, 1 CREATE way, Singapore 138602, Singapore
[2] Earth System Science Interdisciplinary Center, University of Maryland, College Park, MD 20740, USA
[3] Singapore–MIT alliance for Research and Technology, Singapore 138602, Singapore
[4] Chair of Planning of Landscape and Urban Systems, ETH Zurich, 8093 Zurich, Switzerland

Keywords:

Urban vegetation
Leaf area density
Radiative transfer modelling
3-D urban model reconstruction

Published: Forests 2019, 10, 700; doi:10.3390/f10080700

Abstract

Increased urbanization and climate change have resulted in the intensification of the urban heat island (UHI) effect, particularly in tropical cities. One of the main causes of UHI is the man-made urban surfaces influencing the radiation budget by absorbing, reflecting, and emitting radiation at various wavelengths. The radiative budget of a city is directly influenced by the urban geometry, surface materials, direct solar radiation and incident angle, and atmospheric diffuse radiation. Vegetation cover, in contrast, can decrease UHI by intercepting radiation and through the process of photosynthesis. Better understanding the effect of urban vegetation on the radiative budget can thus contribute towards the mitigation of the UHI effect and ultimately the development of climate-resilient urban spaces. To analyze the contribution of vegetation to the radiative budget of a city, a detailed simulation of the complex interaction between the built environment and the vegetation is required. This study proposes an approach for analyzing the 3-D structure of both vegetation and built environment to quantify the contribution of vegetation to the radiative budget of an urban landscape. In a first step, a detailed 3-D model of Singapore including buildings and vegetation was reconstructed using a combination of free and commercial Earth Observation data. Then, the 3-D Discrete Anisotropic Radiative Transfer (DART) model was repurposed to estimate the radiation absorbed by the urban surfaces accounting for the presence of vegetation cover with changing Leaf Area Density (LAD) conditions. The presence of trees in the scene accounted for a significant reduction of the absorbed radiation by buildings and ground. For example, in the case of a residential low-building neighborhood, although having low tree cover, the reduction of the absorbed radiation by buildings and ground was up to 15.5% for a LAD =1. The field validation shows good agreement (R^2 =0.9633, RMSE=10.8830, and Bias=−1.3826) between the DART-simulated shortwave exitance and upwelling shortwave measurements obtained from a net radiometer mounted on a local flux tower in the urban area of Singapore, over the studied period. Our approach can be used for neighborhood-scale analysis, at any desired location of a city, to allow test scenarios with varying surface materials and vegetation properties.

2.1. Introduction

Tropical cities are experiencing more frequent temperature extremes due to climate change and the UHI effect [1]. The length, frequency, and intensity of heat waves are expected to rise in the future, exacerbating the already poor air quality of densely populated cities, increasing health risks of vulnerable population groups, affecting the thermal comfort of urban residents, and increasing the demand for energy for cooling systems[1][2][3][4]. Two of the key factors that contribute to the UHI effect are the radiative interaction between complex urban surfaces and the reduced vegetation cover [5]. To inform planning, a detailed understanding of the influence of the complex interactions between radiation and the urban surfaces is required at local, neighborhood, and city scales [6].

The radiative budget is a key parameter in urban energy balance and climate models. It summarizes the interaction between radiation and urban surfaces. Its study in urban environments has gained attention in recent years as an essential part of the global energy budget of big cities [63]. The radiative budget of a city varies temporally and spatially, where urban surfaces and vegetation interact, absorbing, reflecting, or emitting radiative energy at various wave-lengths. As a result, the radiative budget is directly influenced by the urban geometry, surface materials, solar incident angle, and atmospheric diffuse radiation. Urban greenery, such as trees and other types of vegetation provides local cooling via shading, evapotranspiration, and photosynthetic activity [7][8]. Therefore, examining the effect of urban vegetation on the radiative budget of a city is essential to guide the development of livable urban environments.

Different radiative transfer models and simulators with various levels of detail exist. Depending on the scope, some models can be applied from city scale to detailed micro-scale urban analysis. A review on modelling approaches of radiative exchange in urban areas is presented by the authors of [64]. Some of the limitations of existing radiation simulation software, such as those used in ENVIMET [22], VTUF-3D (TEB) [6], and SOLWEIG [23], are found in their characterization of vegetation, their modelling of radiative fluxes, and/or their capability for large-scale 3-D analysis. Lacking the physical bases, some of these models account for vegetation in a simplistic way and/or use a simplified parameterization of the vegetation properties in terms of the shade of an opaque object. Such an approach does not capture the biophysical complexity of vegetation, which allows some radiation to pass through the canopy through gaps of various sizes. To improve this simple treatment of vegetation, biophysical parameters of the tree canopy (e.g., Leaf Area Index (LAI) and Leave Area Density (LAD)) can be incorporated. Furthermore, existing modelling packages treat radiation in an approximated way with optical properties relying only on a few simplified parameters like albedo and emissivity. As a result, the detailed properties of radiation ranging over the short-wave and long-wave spectrum are not properly simulated. Finally, multiple scattering interactions between vegetation and buildings are not accounted for, which can result in non-negligible bias to both the short-wave and the long-wave (gray body) radiative budget.

Physically-based radiation transfer models used in the field of remote sensing were developed to compute radiation precisely in either narrow or broad spectral domains [65][66][67][68]. Such precision is highly important in order to invert and evaluate existing data and for the preparation of future satellite missions [26]. To accurately model radiative fluxes in 3-D urban scenes, we use such a physically-based radiation transfer model, the Discrete Anisotropic Radiative Transfer (DART) model, to assess the influence of vegetation in the radiative budget of an urban area. The DART model [26][25][27] is one of the most comprehensive physically based 3-D radiation transfer models from ultraviolet to thermal infrared spectral domain [69][70]. There are several functions in DART that make it a relevant tool to be used in our study:

(a) DART spectral domain extends from ultraviolet to thermal infrared, simulating shortwave broadband as weighted integration of narrow bands. Since the solar radiation and optical properties of objects vary dramatically over the spectral domain, the use of DART can provide more accurate results compared to simulation software in which radiation is only assessed in terms of short-wave and long-wave radiation (2 values) and the optical property is only defined by albedo and emissivity of broadband.

(b) DART considers all types of surface optical properties, including isotropic property (Lambertian) or anisotropic property (specular, or predefined bidirectional reflectance distribution function), which extends the applications to all different materials.

(c) DART models multiple scatterings between simulated scene elements in 3-D. This generates more accurate results for scene elements with high reflectance in the short-wave domain, and it permits modelling the gray body (emissivity less than 1) in the long-wave domain.

(d) DART uses a discrete-ordinate forward ray tracing approach, which facilitates an efficient generation of the 3-D radiative budget as opposed to models using backward ray tracing or radiosity approach.

(e) DART can simulate a cluster of leaves as a turbid medium defined by leaf area density, leaf angle distribution, and clumping function. By doing so, it saves the computer memory in storing every single leaf and provides results with high accuracy.

The objective of this study is thus to present a method to derive a 3-D model of a city using satellite data, which enables quantifying the influence of vegetation in the radiative budget of any existing urban area. We illustrate the approach in Singapore, a tropical city experiencing a high UHI effect [71][72]. We (1) developed a method for the creation of a 3-D scene of a city from satellite data; (2) conducted a sensitivity analysis of the radiative budget to changing LAD values; (3) illustrated the DART application in several 3-D scenes corresponding to important urban typologies found across the city to illustrate the effect of changing built environment configurations and ground surface materials; and finally, (4) validated the simulated radiative budget against net radiometer data from a local flux tower.

2.2. Materials and Methods

The study has two main components; first, the creation of a realistic 3-D model of the city, including buildings and vegetation; and second, the quantification of the influence of vegetation in the radiative budget of urban landscapes. The urban scenes consist of subsets of common urban typologies found in the city of Singapore. Those subsets were taken from the generated 3-D city model within the Bedok planning area. This planning area was chosen due to the proximity to the radiometer measurements. In the following, we present the workflow used to quantify the influence of vegetation on the radiative budget of various urban types in Singapore. The data used in this study are either open or commercially available, which allows replication in other cities. Additional details on the 3-D scene generation and the parameters used in the DART model can be found in Appendices A and B.

2.2.1 Generating 3-D Model of a City Using Open or Commercially Available Data

The workflow for creating the 3-D urban scenes consists of five steps presented in Figure 1 and elaborated further down. It should be noted that the resources for creating a 3D scenario in this work are either open or commercial data set. Thus, our approach can be expected to work for most of the cities

in the world without involving airborne laser scan, which is either unavailable or security-sensitive in the data distribution.

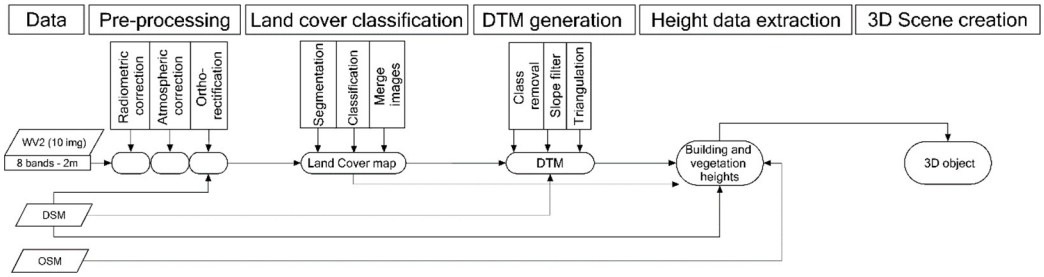

Figure 1. Conceptual framework for 3-D scene creation. WV2 = WorldView2; DSM = Digital Surface Model; OSM = Open Street Map building footprints; DTM = Digital Terrain Model.

2.2.1.1 Pre-processing

Ten high-resolution WorldView2 (WV2) satellite images (8-band, 2m pixel size) were used to map the land cover and vegetation types across Singapore. The preprocessing tasks werecarried out using ENVI software and included three steps namely WV2 Radiometric calibration [73], FLAASH atmospheric correction [74], and SPEAR Orthorectification [75]. The FLAASH module requires information on the atmospheric conditions at the time of acquisition of each image, the parameters used are listed in Appendix A and were obtained for Singapore from the NASA-Aeronet site.

2.2.1.2 Land Cover Classification

The preprocessed images were analyzed using multiresolution image segmentation and classification using the eCognition software. Due to the high occurrence of cloud cover and shadow effects, manual reclassification was required in the areas with low quality data. Two additional Quickbird images were analyzed and resampled to 2 m to fill up the remaining gaps towards the full data coverage over the city of Singapore. The classification resulted in twelve images classified into trees, grass, shrub, bare, built and water. The classified outputs were merged prioritizing the images with the latest acquisition date. An image of the land cover map for Singapore can be found in Appendix C

2.2.1.3 Digital Terrain Model and Height Data Extraction

A digital surface model (DSM) derived from the photogrammetric reconstruction of Digital Globe stereo satellite images (AW3D) was used to derive a digital terrain model (DTM), buildings, and vegetation heights. The nominal resolution of the DSM dataset is 1m for the urban areas and 5m for the densely vegetated areas. The relevant tiles for the study area were merged and resampled to 1m. The DTM was generated in three steps. First, a 10 m buffer was created around OpenStreetMap building footprint data, then, the areas corresponding to buildings, their buffer, and vegetated areas were removed. The resulting areas were used as "bare earth points". To avoid errors due to the effect of tall buildings or misclassifications in the land cover map, the second step was to use the DTM slope-based filter [76], with the search radius and slope parameters set between 30–50 and 10–15 respectively. Finally, the terrain model was reconstructed using the module multilevel B-spline Interpolation [77] and smoothed using a Gaussian filter.

2.2.1.4 Height Data Extraction

Building and vegetation heights were obtained by cross-referencing the DSM and the DTM with building location data and the vegetation layers of the land cover map. In the case of the buildings, the 90th percentile of the DSM values was used to indicate the roof, and the average of the DTM values for the same area were subtracted to obtain the effective building height. Vegetation height values were obtained by subtracting the DTM from DSM over the corresponding vegetated areas. Adjustments to the tree height layer were made to avoid erroneous values, such as vegetation getting height values from the buildings in close proximity or densely vegetated showing low values due to the inability to collect ground points in such areas during the DTM generation. With the aim of realistically representing the tree height for simulation, abnormal values were therefore modified by randomly assigning a value ranging between 5 and 16 m.

2.2.1.5 3D Scene Creation

A 3-D model of the city was reconstructed with the elements of the scene grouped into trees, buildings, and ground with varying land cover types. Figure 2 shows a sample of the 3-D scene over the study area. There are different ways to incorporate the information layers in a way that can be read by DART. One option is to create a scene in. obj format, in which the elements are grouped by type. In this case, the scene was created using ESRI Arcscene software. The first step is to convert the information layers into shape file format. Then, the "building" shape files are extruded according to their height attribute. The land cover classes, i.e., grass, bare soil, water, and paved are extruded 10 cm, in order to be merged with the rest of the scene components. The next step is to export the scene into ".wrl" format. Finally, the scene was exported into ".obj" format, keeping the elements of the scene grouped by type. This final task was done using 3DsMax software. The second option is to convert the scene information into 'DART plots text files'. This method is of relevance specially when creating 'turbid' vegetation plots for a given scene. The use of 'DART plots text files' enables a higher level of detail describing the elements of the scene and providing a more realistic representation of the tree canopy. Therefore, this method was used to input the trees into DART.

Figure 2. 3-D scene of Bedok planning area, Singapore. The red dot indicates the location of the flux tower used for field validation.

2.2.1.6 Urban Typologies Selection

Urban plots (620 m × 612 m) were selected and extracted from the 3-D model of Bedok planning area, Singapore. These plots correspond to homogeneous patches representing common urban typologies

found in Singapore. Figure 3 summarizes the properties of each scene.

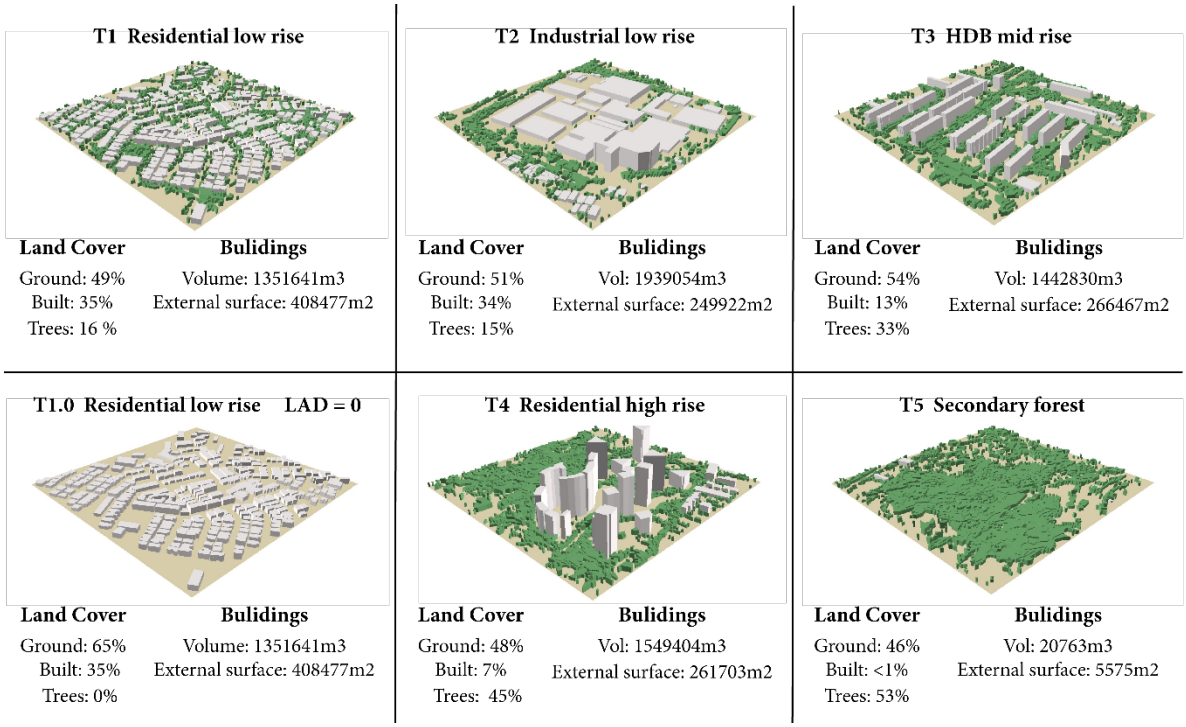

Figure 3. Cover properties of the 3-D objects used for radiative budget simulations representing common urban typologies found in Singapore. T1.0 represents T1 with Leaf Area Density (LAD) = 0. HDB (Housing Development Board) corresponds to public housing districts in Singapore.

2.2.2 Quantification of the Influence of Vegetation on the Radiative Budget of 3D Urban Scenes.

2.2.2.1 Field Measurements of Leaf Area Density

Terrestrial LiDAR scanning (TLS) measurements are increasingly being used to describe the 3-D spatial variability in canopy structure and to retrieve biophysical properties such as LAI and LAD [43][45]. This project uses TLS measurements to estimate the LAD, a property used to quantify canopy foliage as one-side area density within a given volume (m^2/m^3). TLS measurements of common urban trees were collected at various locations in Singapore. Similarly, additional samples were collected on continuous vegetated patches in urban parks. LAD was computed using VoxLAD, a parametric model that uses computational geometry to estimate LAD at the voxel scale on the basis of TLS point cloud data [78]. The obtained LAD values ranged from 0.2 to 1

2.2.2.2 Radiative Transfer Simulations Using DART

The DART model was used to compute the radiative budget of the 3-D scenes considering the influence of vegetation. The Absorbed Photosynthetically Active Radiation (APAR) represents the amount of incoming solar radiation in the Photosynthetically Active Radiation spectral region that is absorbed by a photosynthetic organism, typically describing the light absorption across an integrated plant canopy. This biophysical variable is directly related to the primary productivity of photosynthesis [79]. In the context of radiative budget and energy balance, APAR relates directly to the amount of energy which will be out of the system. Therefore, to obtain the magnitude of the influence of vegetation, this study conducted series of broadband simulations in the shortwave domain

(0.2–3 μm) and in the PAR domain (0.4 to 0.7 μm).

The selected urban plots were imported into DART in. obj format. Optical properties were assigned to the materials accordingly. Similarly, vegetation properties including LAD were assigned to the vegetation groups. The simulations were carried out for the day 23-March-2014, assuming clear sky. The atmosphere was included in the simulation using the database corresponding to a "Tropical-Urban" setting. The aerosol optical depth (AOD) for Singapore was retrieved from the NASA- Aeronet site for the simulation date. The radiative budget was computed at 2 m cell size, at diverse time steps between 7:30 and 19:30. A detailed list of the simulation parameters is shown in Appendix B.

2.2.2.3 Calibration with flux tower data

Net radiometer data (CNR1) was obtained from the flux tower measurements at Telok Kurau site in Singapore [60] on date 23-March-2014 for field validation. A series of hourly shortwave upwelling radiation simulations were run assuming a clear sky for the same date. The small (200 m × 200 m) 3-D model corresponding to the area of the flux tower footprint was generated. The location of the flux tower is marked with a red dot in Figure 2.

2.3 Results

2.3.1 Sensitivity of the Model to Leaf Area Density

Simulations in the shortwave and Photosynthetically Active Radiation (PAR) domain were run varying the LAD value between LAD = 0 (no trees) to LAD = 1 for the "residential low rise" typology (Figure 4). The results comprise the effect of varying LAD in the amount of shortwave radiation absorbed by ground and buildings and the absorbed photosynthetic active radiation (APAR). The graph corresponds to the average of the values of a determined cell type, in this case, absorbed radiation by cells corresponding to buildings and cells corresponding to ground. At 13:00, the amount of radiation absorbed by ground and buildings varies in the order of magnitude of 838.2 W/m2 for a scene without trees, and 708.4 W/m2 for a scene with trees with LAD = 1. The maximum rate of absorption occurs between LAD = 0 and LAD = 0.2. Then, equal increments of LAD, produce a decrease in rate of absorption by ground and buildings. The amount of radiation absorbed by plants for photosynthesis is in the order of 33.0 W/m2 for LAD = 0.2 and 84.7 W/m2 for LAD = 1. Additionally, a decrease in the rate APAR is observed toward higher LAD values. A visualization of the localized effect of increasing LAD values per time step is shown in Figure 5. The first row corresponds to simulations with no trees, therefore the shade is cast only by buildings. The third column corresponds to time step 13:00, where we can best see that the higher the LAD value the lower the absorbed radiation by ground and buildings.

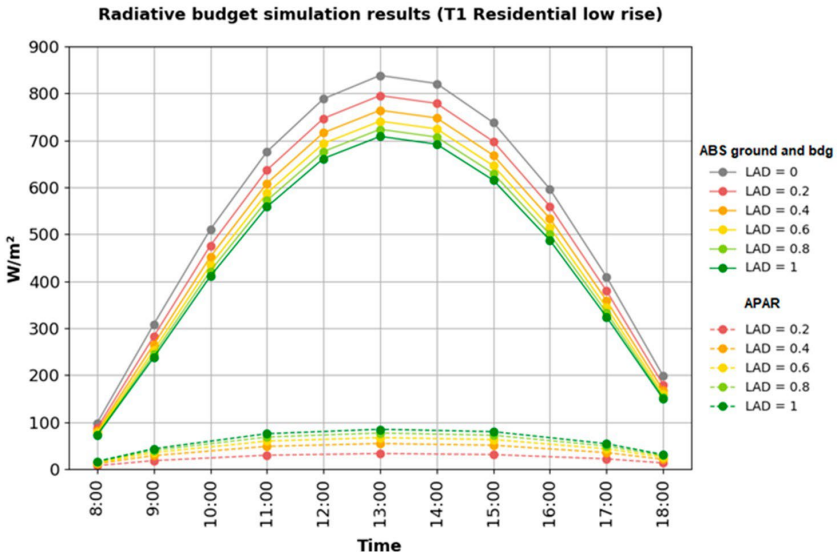

Figure 4. Time series of radiative budget simulation for a residential low-rise urban type (Typology 1), showing absorbed shortwave radiation by ground and buildings (ABS) and absorbed photosynthetically active radiation (APAR) with varying leaf area density (LAD) value.

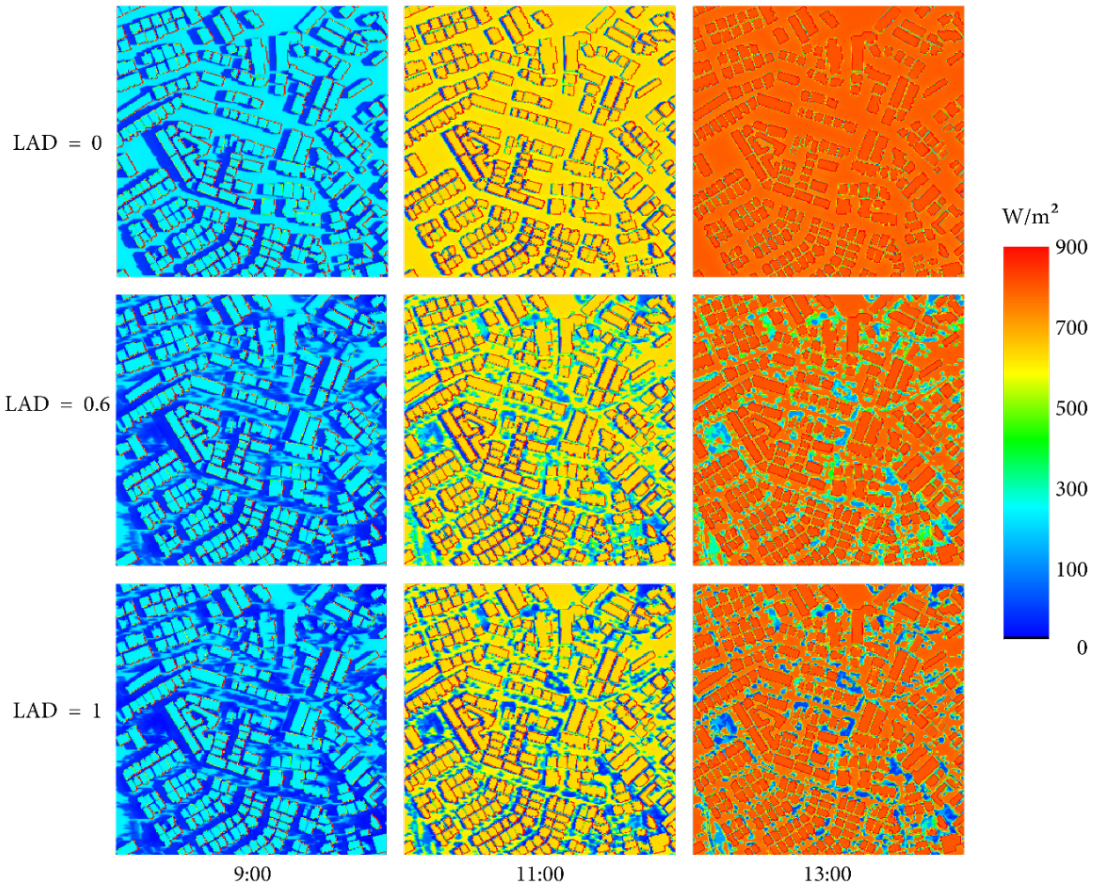

Figure 5. 2D visualization of time series of absorbed radiation by ground and buildings (for a residential low-density urban type, Typology 1). Time step on x-axis with changing leaf area density (LAD) on y-axis. LAD = 0 indicates a simulation of a scene with buildings and ground with no trees.

2.3.2 Comparing the Radiative Budget of Different Urban Typologies.

To compare the different urban typologies commonly found in Singapore, a set of simulations was carried out with LAD value fixed to (0.6). The results comprise Bottom of Atmosphere (BOA) irradiance, exitance, and absorbed radiation per object type. These are expressed in a series of (W/m^2) at each time step between 9:00 and 17:00. Figure 6 summarizes the computed radiative budget for each of the scenes at time 13:00.

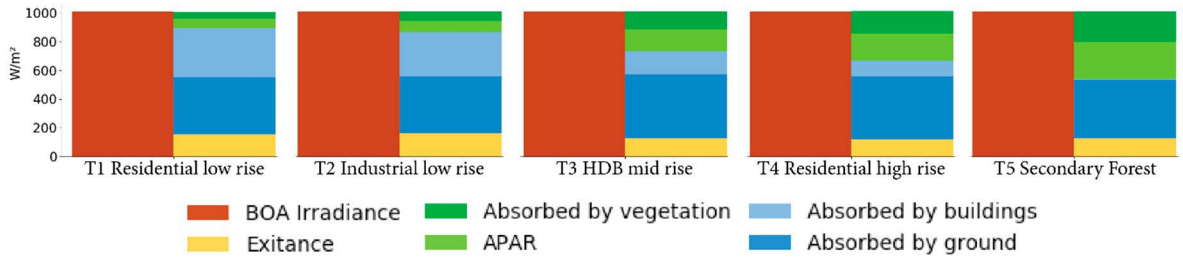

Figure 6. 3-D Radiative budget results per cell type of the analyzed urban typologies at time 13:00. LAD value fixed to 0.6.

When comparing the five typologies in terms of absorbed radiation by ground and buildings (Figure 7a), we observe that "T1 Residential low rise" has the maximum values, decreasing in the order "T2 Industrial low rise", "T3 HDB medium rise", "T4 Residential high rise", and "T5 Secondary forest", respectively. In this case, the magnitude of absorbed radiation is mainly determined by the external surface area of buildings. Comparing "T1 Residential low rise" against "T4 Residential high rise", we observe a difference of 194.0 W/m^2 at 13:00. In terms of absorbed photosynthetic active radiation APAR (Figure 7b) we can observe that the quantities vary in relation to the amount of vegetation found in each typology. In a "secondary forest" (T5) setting, the magnitude of APAR was estimated to be 257 W/m^2 at 13:00. For the case of "residential low rise" (T1) and "industrial low rise" (T2) APAR at 13:00 is as little as 68.4 W/m^2 and 79.9 W/m^2, respectively. A 2-D visualization of absorbed radiation by ground and buildings for each typology in five-time steps is shown in Figure 8.

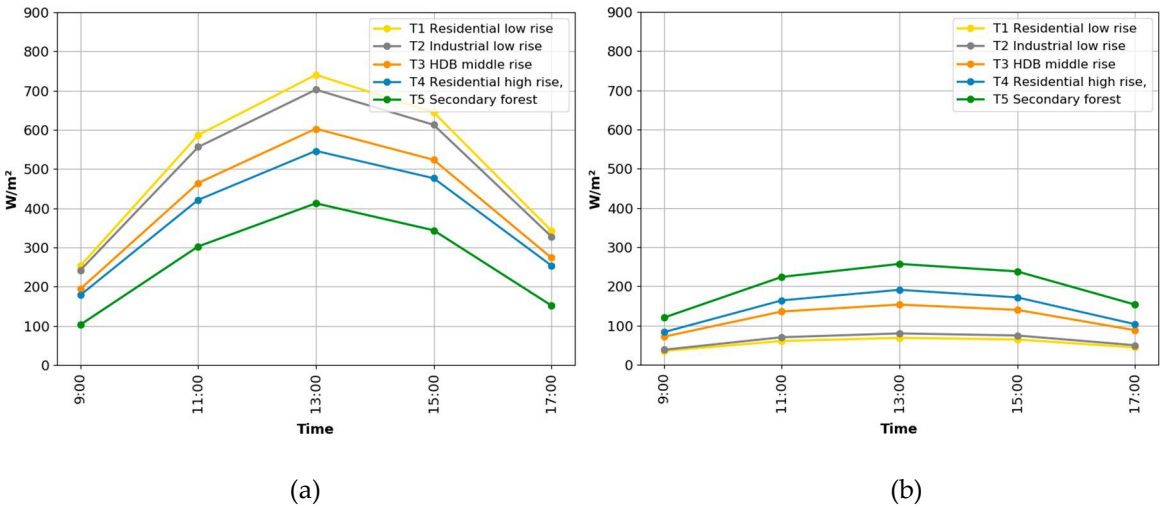

Figure 7. Comparison between different urban typologies. (**a**) Absorbed shortwave radiation by ground and buildings. (**b**) Absorbed photosynthetically active radiation.

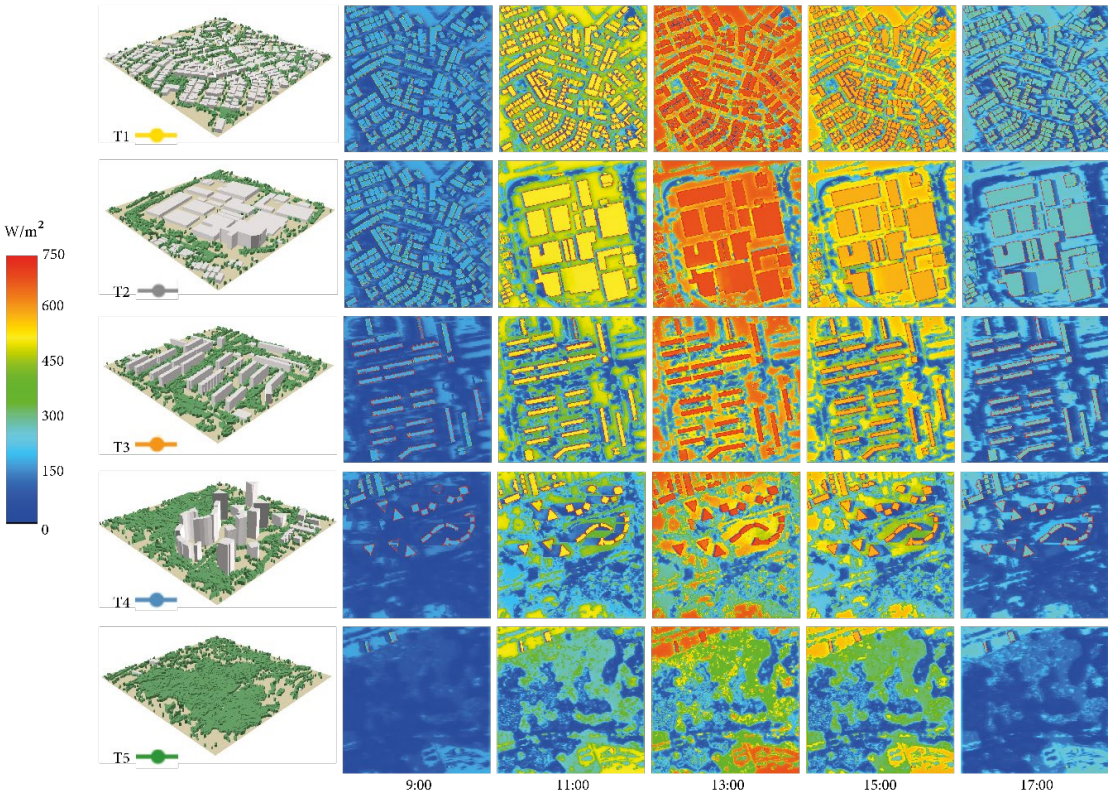

Figure 8. 2-D visualization of absorbed radiation by ground and buildings for each typology in five-time steps between 9:00 and 17:00. "LAD set to 0.6, ground material set to asphalt".

Shortwave Exitance Simulation and Field Validation

The simulation outputs were plotted against the shortwave net radiometer field measurements as shown in Figure 9b. The site level comparison between shortwave exitance simulations and net radiometer data on 23 March 2014 indicates good agreement (R^2 = 0.9633; RMSE = 10.8830; Bias = −1.3826) for the study period over Telok Kurau flux tower. This date corresponds to the day with the lowest cloud cover reported. Therefore, our simulation results, represent the maximum attainable values over a day with a clear sky. Notice there is a slight delay of the observed value compared with the simulated value (15–30 min). There are several possible reasons: (1) the net radiometer integrates the radiant flux within a hemispherical field of view (FOV) at the sensor location. On the other hand, DART models the exact upwelling radiation of the scene that exit through all the upward direction. They are not exactly the same quantity, but they are expected to be consistent. (2) Due to the FOV of the net radiometer, the iron frame of the flux tower itself has an influence on the measurements. For example, an obvious sink can be observed for downwelling shortwave radiation due to the shadow projection onto the radiometer; (3) there might be a slight offset between the net radiometer and the nadir direction.

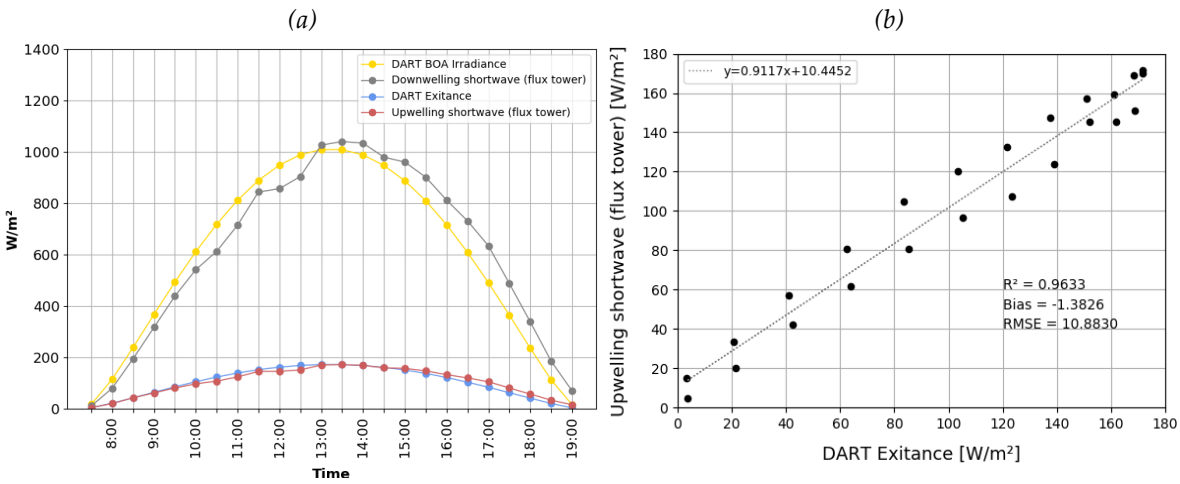

Figure 9. (**a**) Time series of Discrete Anisotropic Radiative Transfer (DART)-simulated bottom of atmosphere (BOA) irradiance and exitance and upwelling and downwelling shortwave radiation obtained from net radiometer measurements. (**b**) Scatterplot of DART-simulated exitance against upwelling shortwave.

2.4 Discussion

3-D computer-based city models have become the base for a variety of tasks related to urban microclimate studies. However, the availability of data for generating such models remains often challenging due to policy or simply lack of spatial information. This work used commercial satellite optical imagery to generate a 3-D model of urban form and vegetation across the entire city of Singapore, providing the data source to run radiative transfer simulations and modelling tasks at any desired location in the city. Such data has also been used in recent work on wind flow simulation and in a study of the urban climate of Singapore [80][81]. The accuracy of deriving tree height from satellite optical data remains low (3.5 m in this case). Ideally, Aerial Laser Scanning (ALS) would be the best data source for this purpose. However, access to such data remains restricted not only in Singapore, but also in many countries due to the high cost or security reasons. Additionally, this work has repurposed the DART model to perform an analysis of the effects of urban form and vegetation on the radiative budget. By using DART, a spatially explicit 3-D radiation budget can be simulated for any urban or natural landscape at different scales. Our results show good agreement between DART-simulated shortwave exitance and radiometer observations. However, the area corresponding to the footprint of the net radiometer is characterized by a grass field, few buildings, and reduced tree cover. Ideally, additional validation sites would be useful to assess the robustness of our method over different vegetation and urban settings. Another advantage of using DART is the possibility to simulate the atmosphere considering real observations of the Aerosol Optical Depth (AOD), for a determined date and location. The adjustment of this parameter played an important role in increasing the accuracy of our simulations when comparing them with real observations. We suggest special attention to adjusting this parameter using real observations of AOD for the specific simulation date and time.

One of the limitations of our approach is the simplification in terms of surface material designation. This simplification was made due to the interest in using directly information obtained from a dataset generated using satellite imagery (overall shape, location of the objects, and few land cover classes). This level of detail can be useful for large-scale analysis, but is not optimal for analysis at finer scales. Approaches to retrieve optical properties from satellite data exist, for example, in the paper by the authors of [63] surface optical properties were retrieved through an iterative approach based on the 3D urban landscape and the use of DART. This however was not included in our current study. To add

more variation, the user could modify the properties of buildings in a generalized way, taking into account the context (i.e., downtown areas assume facades to be glass-dominated, etc.). Our proposed methodology for the creation of a 3-D model of a city includes four ground cover classes (grass, bare soil, paved, and water). These distinct groups can be used to test different properties according to the user's interest. The within-scene variation of ground cover material was not considered in our current simulations; however, our methodology includes the generation of scenes with variation in ground cover.

The optical properties of surface materials have a dominant effect on the radiative budget; therefore, special attention to the selection of materials is crucial, as this may lead to erroneous simulations and wrong conclusions of the study. The magnitude of the effect of different surface materials on the radiative budget can be inferred by looking at their spectral signature. A graph showing the reflectance of some of the mineral materials within DART database can be found in the image (a) of Appendix D. Similarly, graph (b) shows the reflectance curves for few types of trees and grass. Spectral information of local materials/vegetation of interest can be added into the database and used to produce more realistic simulations. To provide an idea of the effect of ground material on the overall radiative budget of a scene, additional simulations testing grass, soil and asphalt as ground cover were run over the typologies T4 "High rise residential" and T5 "Secondary forest". The complete set of simulation results were compared to a base scenario (T5 Secondary forest; LAD = 1; ground cover = grass) and sorted in terms of the difference in radiation absorbed per scene. The comparative table can be found in Appendix E.

Biophysical and biochemical properties of vegetation such as LAI, LAD, canopy spread, reflectance, etc. are required to obtain realistic radiative transfer simulations, especially at finer scales. In our study, vegetation voxels were created in the regions of the land cover map that correspond to "trees class" and were placed at the upper two-thirds of the total tree height. Then, a unique LAD value was assigned to all the vegetation voxels in the scene. If local LAD data becomes available at larger extents, this information could be added to increase the accuracy of the simulations. Other factors such as leaf clumping coefficient and leaf angle distribution could be considered for simulation; however, they are difficult to measure in the field and to further specify their distribution over individual trees in an urban scene. Therefore, we made the assumption of keeping the same LAD value without clumping. Our methodology proposes using satellite data to produce a 3-D model to perform simulation tasks over an existing situation. If the user would be interested in testing scenarios with changing the percentage of foliage cover this would require modifying the original land cover map, and then re-doing the steps to produce new scenes. Another possibility would be to use connected component analysis over the vegetation voxels to restrict and reduce the outline of the crown in order to change the clumping without changing the coverage. Further analysis could be performed at finer scales such as neighborhood or tree level using a more detailed consideration of the shape and construction material of buildings as well as the real shape and detailed properties of vegetation. These object inputs, however, need to be done in a 3Dmax or CAD environment, probably more suitable for architects and designers interested in analysis at local scales.

Despite the advantages of DART to perform analysis at different scales, a high level of detail over large scenes will result in longer computation times. Therefore, it is crucial for the user to balance the trade-offs between scene size, level of detail, and computation time.

2.5 Conclusions and future work

Studies of the urban microclimate and UHI are gaining more attention in recent years and the related demand for mitigation strategies is on the rise. This research contributes to the development of methodologies to produce data that enable a better understanding of the influence of vegetation and other urban parameters on the radiative budget of urban landscapes. Our study highlights the

potential of using DART for detailed 3-D radiation transfer simulations at different scales, opening opportunities for more in-depth treatment of radiation in urban simulations. The field validation showed a good agreement between upwelling shortwave measurements and shortwave exitance simulated by DART. We shortly provided an overview of the sensitivity of the radiative budget to changes in LAD and varying ground cover materials. The results show that the presence of trees in the scenes accounts for a significant reduction of the absorbed radiation by the buildings and the ground. Additionally, our results indicate that highly urbanized landscapes with no tree cover can absorb up to four times more than a densely vegetated "natural" landscape.

Many possible analyses can be performed, for instance, future work could be conducted on testing different aerosol optical depths, different ground, roof, and wall materials, different tree species, and additional vegetation properties; these analyses however, would be ideally carried out using more ad hoc scenes to minimize the computation times, while obtaining sufficient results for a detailed statistical analysis. Our future work will explore the adaption of DART for the estimation of the mean radiant temperature of urban scenes at different scales. This approach might contribute to more accurate modelling of urban outdoor thermal comfort and could ultimately be used as a tool for planners and designers to evaluate mitigation strategies to reduce the impacts UHI effect.

2.6 Acknowledgments and funding

The authors would like to thank Jean-Philippe Gastellu and the DART team of CESBIO (CNES, CNRS, IRD, University of Toulouse) for the consistent support of the DART model and Erik Velasco (Independent Researcher) and Matthias Roth (Geography Department, National University of Singapore) for providing the shortwave net radiometer data used for validation. The authors appreciate the valuable remarks and suggestions from anonymous reviewers.

This research was conducted at the Future Cities Laboratory, Singapore-ETH Centre, which was established collaboratively between ETH Zurich and Singapore's National Research Foundation (FI 370074016) under its Campus for Research Excellence and Technological Enterprise Programme. Shanshan Wei is funded by the Singapore National Parks Board (Nparks) project "Remote Sensing for Urban Tree Management: Species Classification and Health Monitoring'.

3. Modelling Mean Radiant Temperature Distribution in Urban Landscapes Using DART

Maria Angela Dissegna [1,2], Tiangang Yin [3], Hao Wu [1], Nicolas Lauret [4], Shanshan Wei [5], Jean Philippe Gastellu-Etchegorry [4] and Adrienne Grêt-Regamey [1,2]

[1]Future Cities Laboratory, Singapore ETH Center, 1 CREATE way, Singapore 138602, Singapore
[2]Chair of Planning of Landscape and Urban Systems, ETH Zurich, 8093 Zurich, Switzerland
[3]Earth System Science Interdisciplinary Center, University of Maryland, College Park, MD 20740, USA
[4] Centre d'Etudes Spatiales de la BIOsphère (CESBIO)—UPS, CNES, CNRS, IRD, Université de Toulouse, CEDEX 9, 31401, Toulouse, France
[5] Singapore–MIT alliance for Research and Technology, Singapore 138602, Singapore

Keywords:

Mean Radiant Temperature
DART
3-D Urban Landscapes
Urban Vegetation
Urban Microclimate
Outdoor Thermal Comfort.

Published: Remote Sensing 2021, 13 (8), https://doi.org/10.3390/rs13081443

Abstract

The microclimatic conditions of the urban environment influence significantly the thermal comfort of human beings. One of the main human biometeorology parameters of thermal comfort is the Mean Radiant Temperature (Tmrt), which quantifies effective radiative flux reaching a human body. Simulation tools have proven useful to analyze the radiative behavior of an urban space and its impact on the inhabitants. We present a new method to produce detailed modelling of Tmrt spatial distribution using the 3-D Discrete Anisotropic Radiation Transfer model (DART). Our approach is capable to simulate Tmrt at different scales and under a range of parameters including the urban pattern, surface material of ground, walls, roofs, and properties of the vegetation (coverage, shape, spectral signature, Leaf Area Index and Leaf Area Density). The main advantages of our method are found in (1) the fine treatment of radiation in both short-wave and long-wave domains, (2) detailed specification of optical properties of urban surface materials and vegetation, (3) precise representation of the vegetation component, and (4) capability to assimilate 3-D inputs derived from multisource remote sensing data. We illustrate and provide a first evaluation of the method in Singapore, a tropical city experiencing a strong Urban Heat Island effect (UHI) and seeking to enhance outdoor thermal comfort. The comparison between DART modelled and field estimated Tmrt shows good agreement in our study site under clear-sky conditions over a time period from 10:00 to 19:00 (R^2 = 0.9697, RMSE = 3.3249). The use of a 3-D radiative transfer model shows promising capability to study urban microclimate and outdoor thermal comfort with increasing landscape details, and to build linkage to remote sensing data. Our methodology has the potential to contribute towards optimizing climate-sensitive urban design when combined with the appropriate tools.

3.1. Introduction

The increased number of heat waves due to global climate change experienced in growing urban areas across the world affects the thermal comfort and health of urban residents, particularly in the tropics. The environmental factors controlling outdoor thermal comfort are the Mean Radiant Temperature (Tmrt), wind speed, air temperature, and humidity [82]. Outdoor thermal comfort and heat-related mortality are more influenced by the Tmrt and less by the other three factors [83]. Tmrt is considered an essential bio-meteorological variable having a strong influence on thermal comfort indices such as the Physiological Equivalent Temperature (PET) [84], Predicted Mean Vote (PMV) [82], Universal Thermal Climate Index (UTCI) [85], the Perceived Temperature (PT) [86], and Global Outdoor Comfort Index (GOCI)[87]. A comprehensive review of thermal comfort studies in urban spaces can be found in Lai et al. 2020 [88].

In solar exposure conditions, the energy loss or gain by radiation is the most important heat flux in the energy balance; followed by convective fluxes of sensible and latent heat and at last, the conductive heat flux [89]. The concept of Tmrt is based on the fact that the net exchange of radiant energy between two objects is approximately proportional to their temperature difference multiplied by their ability to emit and absorb heat [82]. This is valid as long as the absolute temperatures of objects in question are large compared to the temperature differences, allowing linearization of the Stefan–Boltzmann Law in the relevant temperature range[90,91]. Different city structures in the same thermal region differ mainly in their radiation temperatures [92]. This is due to the geometrical complexity of buildings, their surface radiative properties, and their wavelength dependency. These properties play an important role in the radiation exchange and therefore, on its modelling. Numerical tools such as Rayman [90], ENVI-met[22], SOLWEIG [23], TUF-3D [93], CityComfort+ [94], and VTUF 3D [6] are increasingly being used by planners and architects to assess the bio-meteorological performance of urban scenarios. Such tools vary in terms of dimensionality, i.e., 1-D/3-D, accuracy in predicting the radiation fluxes, consideration of surface material properties, distribution of surface temperatures, physical representation of the vegetation, scale of analysis, speed of computation, and capability to assimilate remote sensing data as input for simulations.

Remote sensing technologies have great potential to study the thermal behaviour of cities in space and time [95], particularly when combining information on urban surfaces and their spectral characteristics using physically-based radiative transfer models (RTMs). Recent studies have successfully combined a variety of remotely acquired data with RTMs to derive urban surface properties (albedo and temperature), energy fluxes, and Tmrt [24,63,96–99]. These studies highlight an increasing demand for advanced tools capable of 3-D analysis of detailed urban data including vegetation. RTMs used in the field of remote sensing were developed to compute accurate canopy spectral radiance, to invert and evaluate existing data, and for the configuration of future satellite missions [26]. Only a few RTMs simultaneously simulate the canopy spectral radiance and the canopy 3-D radiative budget (RB). To our knowledge, advanced physically-based RTM models have not been fully employed for modelling Tmrt. Therefore, this study seeks to (1) exploit the advanced capabilities of a physically-based 3-D RTM for the estimation of Tmrt of complex urban scenes, and (2) introduce its use for a broader application by planners and urban climate scientists.

In this study, we propose a new method for detailed 3-D modelling of Tmrt in complex urban scenes by improving the radiative budget module of the Discrete Anisotropic Radiation Transfer model DART [100]. The characteristics that make DART a powerful tool to model radiation are summarized hereafter. (1) DART considers the full spectral domain from ultraviolet to thermal infrared in solar/atmosphere radiation and optical properties. Therefore, it provides more accurate results than models that consider that radiation only belongs to two spectral domains (i.e., short and long wave

domains) and/or that the canopy optical property is only defined by its albedo and emissivity. (2) DART considers all types of surface optical properties, including spectral reflectance, transmittance, and absorbance; the spectral emissivity of opaque material is equal to one minus the spectral reflectance of this material. Surface reflectance can be isotropic (Lambertian) or anisotropic using Fresnel equations or a predefined bidirectional reflectance distribution function, which allows DART to consider any material. (3) DART can simulate vegetation either as a set of facet-like leaves with specific locations, orientations, and optical properties, or as a 3-D distribution of turbid medium (i.e., an infinite number of infinitely small plane elements) defined by specific clumping, leaf angle distribution, Leaf Area Index (LAI)/Leaf Area Density (LAD), and optical properties. Therefore, DART simulates light propagation below trees conversely to models that represent trees as opaque volumes. The turbid representation of vegetation is adopted in this work. (4) DART simulates 3-D multiple scattering within vegetation and between vegetation and other materials (e.g., walls). This is very important in the presence of high reflectance scene elements (e.g., green vegetation in the near-infrared domain), and also to simulate the grey body (emissivity less than one) in the long wave domain. (5) In addition to the radiative budget of canopies, DART simulates their remote sensing signal [24][26][25]. DART is considered one of the most advanced 3-D RTMS and it has been positively evaluated in the framework of the Radiative transfer inter-comparison project (RAMI) [69][28].

Our methodology for modelling Tmrt can be applied at different scales and under a range of parameters including the urban pattern, surface material of ground, walls, roofs, and vegetation properties (coverage, shape, spectral properties, Leaf Area Index, and Leaf Area Density). Three-dimensional scenes can be generated from multi-source remote sensing data as shown in our previous study on 3-D Reconstruction of urban landscapes from satellite data, where a detailed workflow for the derivation of 3-D urban scenes was presented, together with an evaluation of 3-D radiative budget over different urban typologies found in Singapore [24]; additionally, scenes can be generated from Aerial LiDAR Scanning (ALS) point cloud data [13] or using 3-D modelling software. Depending on the desired scale of analysis, vegetation turbid plots (i.e., the volume of turbid material) can be generated from satellite data [24], from ALS point clouds [13], or using realistic 3-D models. Moreover, vegetation properties (e.g., LAI/LAD) can be retrieved from terrestrial laser scanning data (TLS) at the plant scale [46][101], from ALS [102][103] at neighbourhood scale, or from other remote sensing systems. Finally, the spatial distribution of vegetation can be modelled from hybrid point cloud data [13]. Information on suggested data sources for scene creation can be found in Table A1 and Table A3 in the appendix section.

We illustrate our approach in Singapore, a city experiencing strong UHI and seeking to enhance outdoor thermal comfort. We present a field comparison and perform a sensitivity analysis to examine how building materials and vegetation properties influence Tmrt. Then, we discuss the limitations of our approach, possible areas of improvement, and future research directions.

3.2. Materials and methods

3.2.1. Scene Generation and Parameter Setting

A 3-D model of the Tanjong Pagar District, Singapore, was reconstructed. The building height, vegetation shape, and distribution was obtained from the Aerial LiDAR Scanning dataset of Singapore [104]. This dataset was acquired by the Optech Pegasus HA500 sensor with a planar density of about 30 points/m^2 which proved to be well adapted to map vegetation. The buildings were reconstructed using 3DsMax software, obtaining a Level of Detail (LOD) of 1.2. The north part of the scene corresponds to the existing urban setting, whereas the southern part (former Tanjong Pagar Port) corresponds to a design proposal with a high-density urban form [13]. The scene elements were

grouped by surface material, allowing them to be linked to their respective surface temperatures and optical spectral properties in the DART database. All trees were assumed to have the same LAI value of 1.5 (single-side leaf area divided by the tree projection area). This value falls within the range of measured LAI of urban trees found in Singapore [42]. Surface temperature is an essential term for simulations in the longwave domain. It can be derived from field observations of a calibrated thermal camera [105] or from an energy balance model, i.e., DART EB. It is provided as an input to DART either as thermal functions (i.e., the mean and standard deviation of hourly modelled temperatures) or as a 3-D temperature distribution. DART uses these thermal functions to distribute the temperature values over the scene using a virtual sun illumination of the scene: the most irradiated surfaces are given the highest temperature values. In our study, the mean and standard deviation of hourly surface temperatures were estimated using the Urban Eco-hydrological model UT&C [106]. UT&C is a fully coupled energy and water balance model that accounts for the biophysical and eco-physiological characteristics of urban trees. UT&C is a 1D model, providing as output the mean and standard deviations of surface temperatures of impervious roof, impervious ground, ground covered with grass, tree, sunlit wall, and shaded wall for each of the parametrized areas of interest. Our study area was classified in urban "typologies" to extract the neighbourhood parameters such as building height, height to width ratio and the fraction of vegetation. The model requires meteorological data of incoming shortwave and longwave radiation, rainfall, pressure, wind speed, air temperature, and humidity at forcing height above the urban canyon. The model was run over the time period from 1 May 2013 to 30 April 2014. The mean and standard deviation of the temperatures were obtained considering all the hours with a cloudiness of less than 50% with the aim to approximate the average conditions on rather sunny days in Singapore. Information on the values such as volumetric heat capacity and thermal conductivity are reported in the supplementary information on the UT&C model development document [106].

3.2.2. Mean Radiant Temperature Computation

To compute the Tmrt of Tanjong Pagar District, we carried out two sets of DART radiative budget simulations, one in the shortwave domain (0.3–2.5 μm) and one in the longwave domain (3–50 μm). Simulations were run at a resolution of 2 m horizontally and 1 m vertically. The use of "repetitive scene mode" in the longwave domain reduces the computation time without producing substantial differences in the resulting radiative budget. However, in the shortwave domain, the use of repetitive scene mode would cause the emergence of shadows that do not correspond to reality. Therefore, we used "isolated scene mode" when running simulations in the shortwave domain. During the simulation process, DART converts the scene into voxels at a defined dimension. These voxels contain information on the material reflectance, surface temperature, and additional properties such as LAI/LAD for the case of turbid vegetation plots. DART stores the resulting radiation that has entered each voxel. The previous versions of DART did not compute the radiative budget on empty cells; therefore, it was not suitable for estimating and mapping Tmrt. The recently improved releases of DART's radiative budget 3-D allow one to store separately the direct, diffuse, and emitted irradiance reaching each and every voxel of the scene from six directions (N-S, E-W, and Upwelling–Downwelling). This allows a virtual transformation of the voxels into equivalent cylinders [107] on which the absorption coefficient of the human surface to solar radiation ($1 - \alpha$) and emissivity of the clothed body (ε) can be considered and be varied at the Tmrt computation stage. In the short waves (i.e., solar radiation), the absorption coefficient of the skin ($1 - \alpha$) ranges between 0.55 and 0.85 depending on the skin color [108]. In the long waves (i.e., terrestrial radiation), the emissivity of the human skin is assumed to be 0.99 and 0.95 for normal clothing surfaces [109]. The complete list of the simulation parameters can be found in Table A4 and Table A5. The surface temperatures used for each time step are reported in Table A6 and Table A7.

The computation of Tmrt is done according to the method proposed by Peter Höppe [110], with further considerations [107]. These include (1) the representation of the human body as a cylinder as opposed to a box, (2) separated treatment of direct and diffuse short-wave radiation as well as for long-wave radiation, (3) consideration of solar elevation and azimuth for every time step. We used a cylinder with the measurements reported in Table 1 to derive the surface fractions $w_{i\ Cylroof} = 0.0616$ and $w_{iCylwall} = 0.28$, respectively. The cylindrical representation of the human body is centered at a height of 1.5 m from the ground.

Table 1. Characteristics of the cylindrical representation of the human body.

Cylinder Dimensions	
Diameter:	0.28 m
Height:	1 m
Total area:	1 m^2
roof area:	0.06 m^2
wall area:	0.88 m^2
Area of frontal view:	0.28 m × 1 m = 0.28 m^2
Surface fraction $\mathbf{w}_{i\ Cylroof}$:	0.0616 m^2/1 m^2 = 0.0616
Surface fraction $\mathbf{w}_{i\ Cylwall}$:	0.28 m^2/1 m^2 = 0.28

The mean radiant flux (Sstr) reaching a rotationally symmetrical (cylindrical) representation of the human body is computed at a specified layer height using Equation (1).

$$\mathrm{Sstr,cyl} = (1-\alpha)\cdot\left[\mathbf{w}_{\mathrm{Cylwall}}\cdot\sum_{1-4}\mathrm{K_{dir,hor}} + \mathbf{w}_{\mathrm{Cylroof}}\cdot(\mathrm{K_{\uparrow dir}} + \mathrm{K_{\downarrow dir}} + \mathrm{K_{\uparrow diff}} + \mathrm{K_{\downarrow diff}}) + \sum_{1-4}\mathrm{K_{diff,hor}}\cdot\mathbf{w}_{\mathrm{Cy}} + \varepsilon\cdot\sum_{1-6}\mathbf{w}_{\mathrm{i}}\cdot\mathrm{L_i}\right] \quad (1)$$

where

α is Albedo of clothed human body (0.37)
$K_{dir,\ hor}$ is Horizontal direct shortwave radiation (KE, KS, KW, KN)
$K_{\uparrow dir}$, $K_{\downarrow dir}$ is Vertical direct shortwave radiation
$K_{\uparrow diff}$, $K_{\downarrow diff}$ is Vertical diffuse shortwave radiation
$K_{diff,hor}$ is Horizontal diffuse shortwave radiation (KE, KS, KW, KN)
ε is Emissivity of clothed human body (0.97)
$\mathbf{w}_i$ is Surface fractions of the standing "cylinder man" ($\mathbf{w}_{Cylwall} = 0.28$ and $\mathbf{w}_{Cylroof} = 0.0616$)
L_i is Longwave radiation

The mean radiation temperature Tmrt [°C] results from the Stefan–Boltzmann law using Equation (2).

$$\mathrm{Tmrt} = \sqrt[4]{\frac{S_{str,cyl}}{\varepsilon\cdot\sigma}} - 273.15 \quad (2)$$

where

$\mathbf{S}_{Str,\ cyl}$ is the mean radiant flux
ε is Emissivity of clothed human body
σ is Stefan–Boltzmann constant $5.670374419 \times 10^{-8}$ $W{\cdot}m^{-2}{\cdot}K^{-4}$

3.2.3. Study Area and Data Collection

Our study area is located in Tanjong Pagar district, Singapore (Figure 1a). Singapore has a tropical humid climate with no distinctive seasons. Near-surface air temperature usually ranges from 23 °C to 32 °C. The "Cantonment Towers" site, a modern social housing compound with a playground surrounded by high-density housing blocks was selected to carry out the field evaluation (Figure 1b). Three net radiometers Kipp and Zonen CNR4 [111] were mounted on a mobile platform at 1.5 m from the ground. The minimum height suggested by the manufacturer to avoid interference from the mounting structure to the readings is 1.5 m. Additionally, a Vaisala WXT536 weather station [112] and a Campbell Scientific 152 mm black globe thermometer [113] were mounted on the platform to record wind speed, precipitation, air temperature, and globe temperature, respectively (Figure 1c). Special care was taken to keep the tower leveled and oriented with the geodetic north [107]. Figure 1b shows the location of the measurement station in the study site.

Figure 1. (**a**) Location of the study area. (**b**) Location of the measurement station within the study site (marked in red). (**c**) Bio-climate measuring station for determining the Tmrt.

A time series composite was generated by collecting observations of the maximum incoming radiation from 20 February 2020 to 2 March 2020 between 9:30 and 19:00 with a time step of one minute. This was done to approximate the maximum attainable Tmrt values for the site over a day with clear sky Tmrt was estimated using the integral radiation measurement technique [91][110]. Calculations of Sstr,cyl were based on angular factors for a rotationally symmetric standing person using Equation (3).

$$\mathrm{Sstr,cyl} = (1-\alpha)\cdot\left[\mathbf{w}_{\mathrm{Cylwall}}\cdot\sum \mathrm{K}_{\mathrm{dir,tot}} + \mathbf{w}_{\mathrm{Cylroof}}\cdot(\mathrm{K}_{\uparrow}+\mathrm{K}_{\downarrow}) + 0.88\cdot\mathrm{K}_{\mathrm{diff}}\right] + \varepsilon\cdot\sum \mathbf{w}_{\mathrm{i}}\cdot\mathbf{L}_{\mathrm{i}} \quad (3)$$

where

$K_{dir,\ tot}$ is Direct and reflected horizontal shortwave radiation (KE, KS, KW, KN)
$K_{\uparrow}$, $K_{\downarrow}$ is Vertical shortwave radiation
K_{diff} is Diffuse radiation = min (KE, KS, KW, KN)
ε is Emissivity of clothed human body
$\mathbf{w}_i$ is Surface fractions of the standing cylinder man ($\mathbf{w}_{iCylwall}$ = 0.28 and $\mathbf{w}_{i\ Cylroof}$ = 0.0616)
$\mathbf{L}_i$ is Longwave radiation

Then, the Tmrt is determined using Equation (2).

3.3. Results

3.3.1. Modelled Tmrt over Tanjong Pagar, Singapore

Figure 2 shows the results of the Tmrt simulation over the Tanjong Pagar district, Singapore, at 15:00 on 29 February 2020. In sunlit areas, the Tmrt at pedestrian level reaches 68 °C. The highest Tmrt values are observed near the sunlit walls of buildings. Tmrt decreases as the distance to the sun-exposed surfaces increases. Under trees, Tmrt varies between 40 °C and 28 °C. The combined effect of building shade and tree shade results in Tmrt values that are below 28 °C. This suggests a slight underestimation of Tmrt in areas without direct solar radiation.

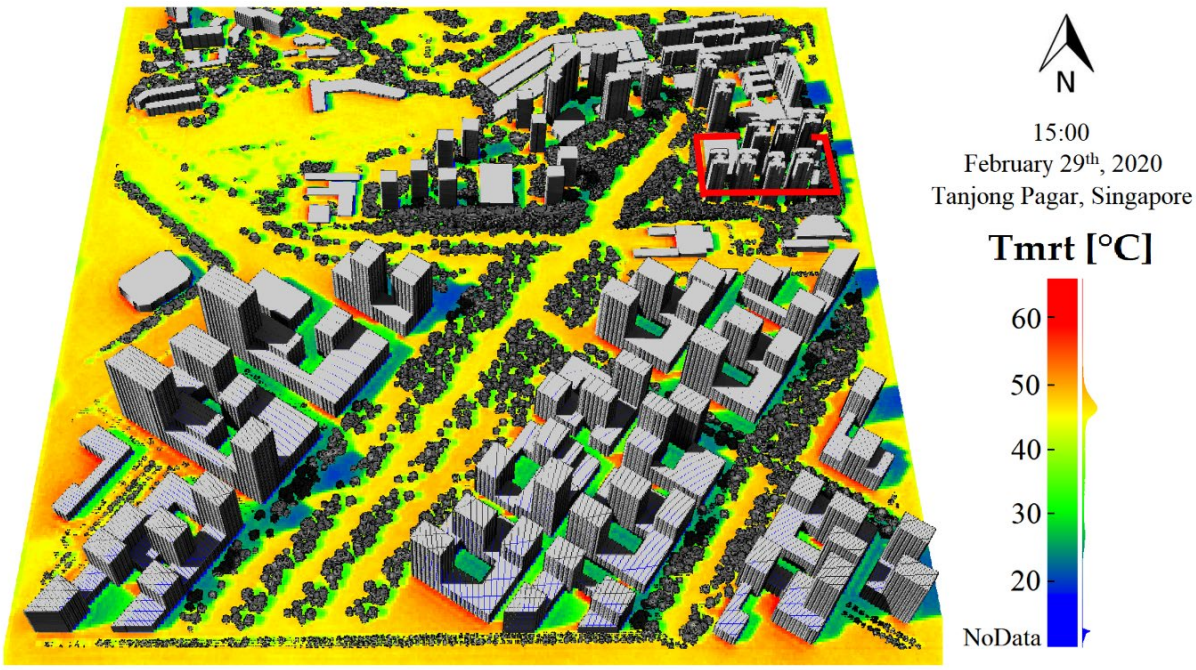

Figure 2. Visualization of pedestrian level Tmrt of the Tanjong Pagar South district, Singapore, at 15:00 on 29 February 2020. The results are overlaid into a Cloud Compare display of the original 3-D scene used for simulations (http://cloudcompare.org/ accessed on 13 July 2020). The north part of the scene corresponds to the existing urban setting while the south is a proposed urban design for the former Tanjong Pagar Port [13]. The area marked in red corresponds to the Cantonment Towers site used for field evaluation.

3.3.2. Field Evaluation

A smaller subset corresponding to the Cantonment towers was generated for the purpose of field evaluation. Simulations were carried out assuming the absence of clouds over the scene and using hourly values of Aerosol Optical Depth (AOD) reported by NASA-AERONET Singapore. They were run at 1m resolution. Then, the values of DART cells with the center 1.5 m above the ground were extracted to compute Tmrt maps at different times of the day (Figure 3). The highest Tmrt values are mostly observed close to the walls that receive direct solar radiation, prominently at 10:00 on the east-facing walls and at 16:00 on the west-facing walls. Generally, higher Tmrt occurs at 16:00.

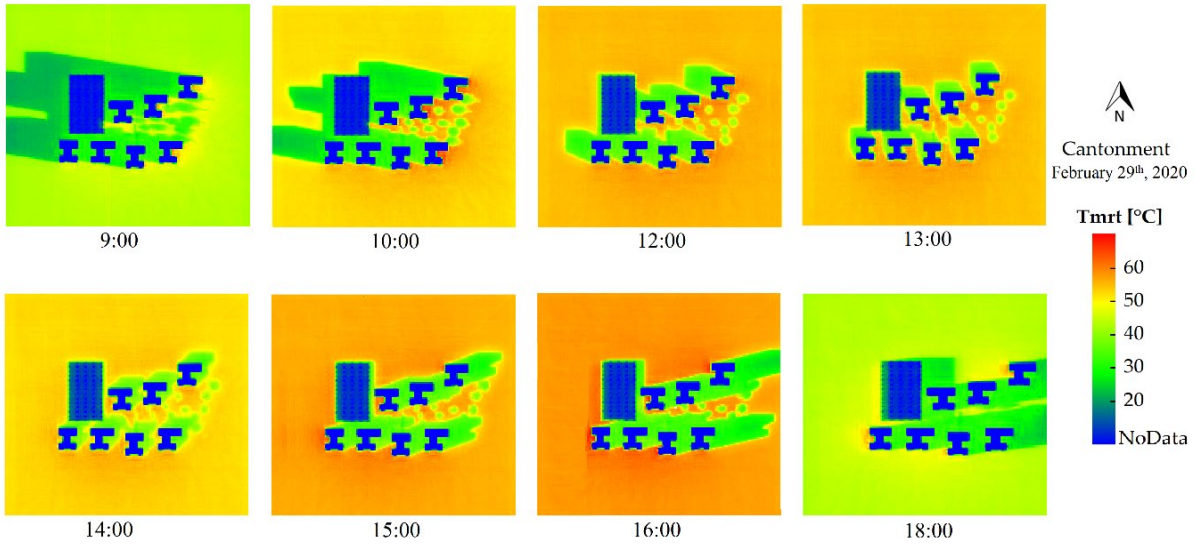

Figure 3. Selected Tmrt maps for the Cantonment towers site at different simulated times of the day.

The comparison of modelled and field-estimated Tmrt is shown in Figure 4. The green line shows the field estimated Tmrt during the sunniest day of the study period, 29 February 2020. The downward peaks indicate a reduction of Tmrt due to the passage of clouds over the site. The blue line presents the maximum Tmrt value of each time step obtained from the net radiometers during the entire study period (20 February 2020 to 2 March 2020). The black asterisks indicate the DART-modelled Tmrt for 29 February 2020 assuming clear sky conditions. The results show good agreement between 10:00 and 19:00 h (R^2 = 0.9697, RMSE = 3.3249) when comparing DART-modelled Tmrt with the maximum Tmrt values reported over the entire study period (blue line). In the morning at 9:00, the modelled Tmrt was estimated to be 19.54 °C. This is explained by the fact that the DART simulation for Cantonment towers was run on a small subset of the scene, therefore neglecting the shadows that are cast by buildings outside the scene, particularly at low solar angles. Around 13:00, we observe a slight overestimation of 2.16 °C in the modelled Tmrt. From 17:15 onwards, our measuring site is affected by the shadow cast by buildings within the scene. Tmrt decreases considerably until sunset just after 19:00. Then, Tmrt is only determined by the longwave radiation fluxes and remains relatively constant throughout the night. From 18:00 to 19:00, in the absence of direct solar radiation, we observe an underestimation of 5.55 °C and 6.395 °C respectively on our modelled Tmrt.

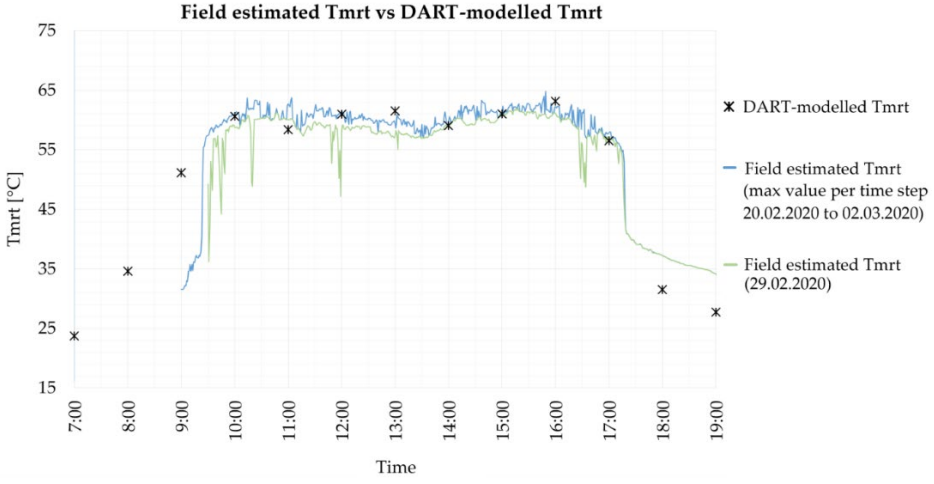

Figure 4. Comparison between DART Tmrt and field-estimated Tmrt. The green line indicates records from 29 February 2020. The blue line corresponds to a composite of maximum values attained at each

time step over the study period. The black asterisks correspond to each time step of DART- modelled Tmrt.

3.3.3. Radiation Fluxes Recorded at the Study Site

The diurnal longwave and shortwave radiation fluxes received from each of the six directions (i.e., North ↔ South, East ↔ West, Up ↔ Down) on 29 February 2020 are illustrated in Figure 5 and Figure 6. In terms of longwave radiation, we observe a steady behavior from the six directions throughout the day ranging between 450 and 600 W/m^2. The maximum values are observed around 14:00. Before midday, the upwelling and West directions have the strongest signal. After midday, the downwelling direction becomes more prominent.

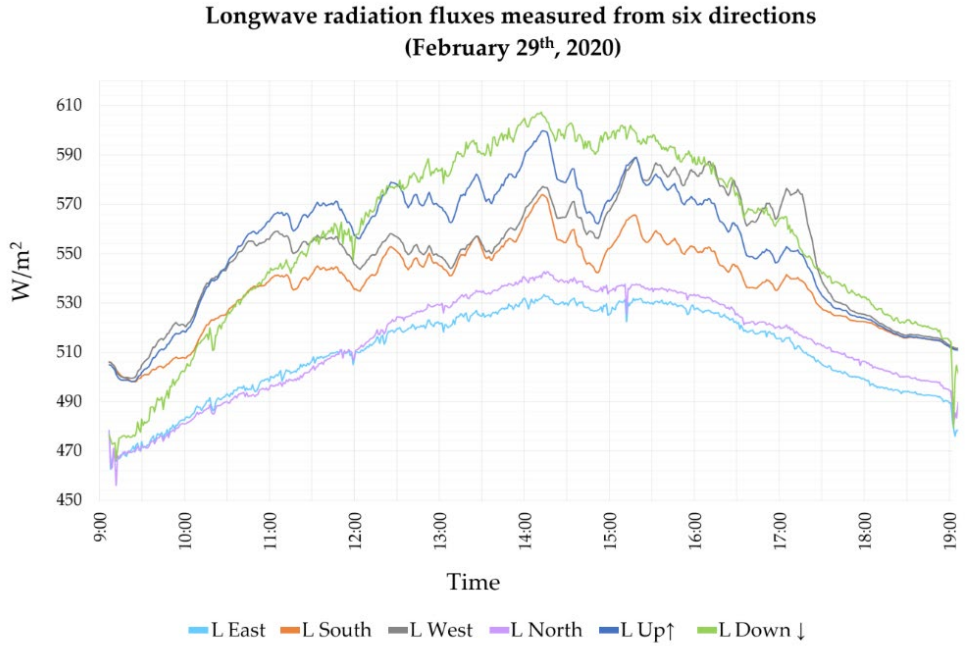

Figure 5. Diurnal longwave (L) radiation fluxes measured from six directions (9:00 to 19:00) on 29 February 2020.

The downwelling shortwave radiation is the predominant flux with a maximum around 13:00 with 980W/m^2 and changes considerably during the day. This flux is primarily determined by the sun's position and the sky view factor of the site. The upwelling shortwave is due to the reflection of solar radiation by the ground. It peaks around 13:00 with 120 W/m^2 with a slight variation during the day. The radiation from the South direction is greater than that from the North, hovering around 250 W/m^2 at 1:00 p.m. and varying gently throughout the day. This is because Singapore is geographically located 1° North from the Ecuator. The downward peaks correspond to the effect of passing clouds over the study site.

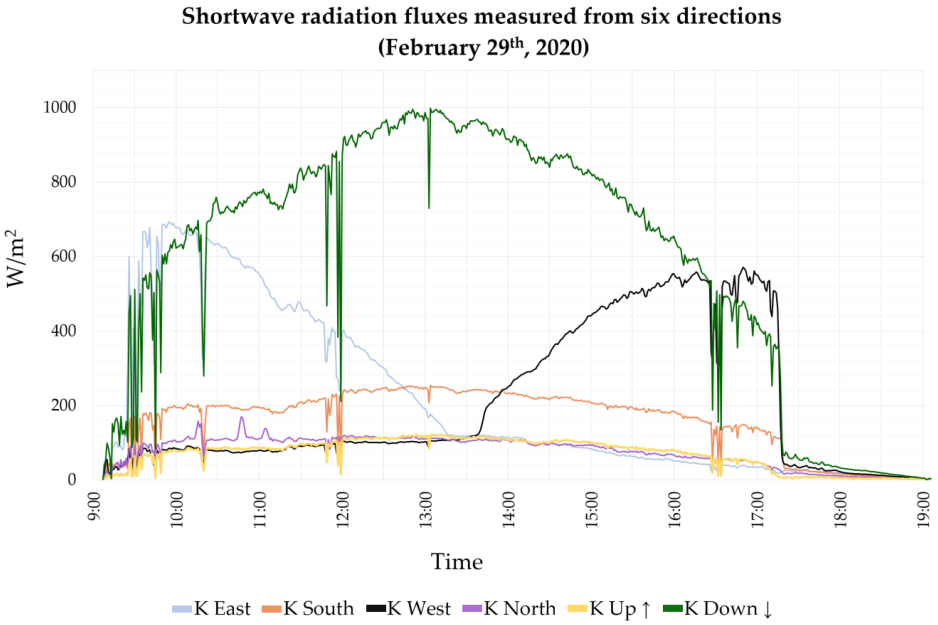

Figure 6. Diurnal shortwave (K) radiation fluxes measured from six directions (9:00 to 19:00) on 29 February 2020.

3.3.4. Sensitivity Analysis

A sensitivity analysis was performed to demonstrate (1) how much the variation of a biophysical vegetation property (LAI) impacts Tmrt, (2) how much ground surface temperature impacts Tmrt, (3) how spectral properties of wall material impacts spatially the Tmrt at pedestrian level.

Effect of Varying LAI on Tmrt Under the Tree Canopy

Urban trees are an important component that contributes to the urban microclimate because of their potential to attenuate solar radiation, evapotranspiration, and control wind speed. In tropical humid regions, the cooling effect by trees is caused mainly by the reduction of Tmrt due to shading. The benefits provided by trees are constrained by several factors such as spatial arrangement, type, age, height, phenology, crown shape, characteristics of trunk and twigs, leaf size, LAI, and leaf reflectance. Strategic placement and optimal selection of vegetation are essential to obtain the desired Tmrt attenuation. Biophysical properties of vegetation such as LAI/LAD are required to obtain realistic Tmrt simulations and to assess the differences between species and planting regimes. The effect of varying LAI on the Tmrt under the tree canopy of three common tree species of Singapore namely Albizia Saman, Khaya Senegalensis, and Tabebuia Rosea was explored and reported in Appendix E. A scene was created using 3-D models of the tree species, assuming the ground material to be grass. Simulations were run at 13:00 and 16:00 using the respective surface temperatures reported in Table A6. The results show that for the three species, the impact on Tmrt due to increasing LAI is large if LAI is low. The impact decreases when LAI increases, and becomes minimal when LAI is larger than 5.5. Khaya Senegalensis has the highest potential for reducing Tmrt. For instance, with small LAI values (LAI = 0.1), we observed a difference in Tmrt up to 16.19 °C when comparing Khaya Senegalensis against Tabebuia Rosea. This is primarily due to the number of twigs and branches and their homogeneous distribution throughout the canopy; this implies a reduction of Tmrt even when LAI = 0.

Effect of Surface Temperature on Tmrt for Different Ground Materials

To provide an idea of the effect of the surface temperature of different ground materials on Tmrt, we simulated a small scene where the surface temperatures of grass, concrete, and three types of asphalt

varied between 20 °C and 60 °C. In the case of grass, the range was assumed to be 20 °C to 40 °C This is because a surface temperature of grass higher than 40 °C is unrealistic. The overall response in terms of Tmrt of the studied materials is almost linear to the change in surface temperature. It was observed that light materials tend to give higher Tmrt, due to their higher reflectance. The results of the sensitivity analysis and additional details are reported in Appendix F.

Effect of Spectral Properties of Wall Material on Tmrt

The radiative response of the urban surface materials plays an important role in the radiative budget and thus, on Tmrt and in the overall urban microclimatic conditions. To assess the influence of different wall materials on Tmrt, we recreated a small scene with three buildings of dimensions (L:10 m, W:24 m, H:18 m). The first building has 100% white walls, the second has 66.6% white walls, and 33.3% glass and the third has 100% glass walls. The simulation was run at 16:00 with a cell size (x, y, z) of 1 m. The results indicate values of 79.39 °C, 68.59 °C, and 64.47 °C Tmrt in the first cell adjacent to the respective building. A detailed representation of the results together with the surface temperatures assumed for this exercise is reported in Appendix G.

3.4. Discussion

This work introduced a new method, which uses for the first time the DART model to estimate and map Tmrt at different scales. Our motivation to use the DART model to estimate Tmrt stems from its capability to assimilate a large variety of 3-D data derived from state-of-the-art remote sensing techniques; providing the possibility to better analyze how Tmrt is influenced by vegetation and its biophysical properties, by the optical properties of surface materials, by surface temperature, and also by local atmospheric conditions. The field evaluation indicated good agreement between DART-simulated Tmrt and field-estimated Tmrt at the Cantonment towers measurement site. However, a substantial underestimation is observed in areas with absence of solar radiation and in the late afternoon. This might be explained by several considerations on which our method is based. Firstly, we assumed clear sky conditions throughout the day. This is valid as long as one seeks to map temperature extremes. However, in a tropical city such as Singapore, the presence of clouds and episodes of rain have a major impact in the actual mean radiant temperature. To give an idea of this, we plotted the field observed Tmrt under different meteorological conditions over the study period in Figure 7. The inclusion of clouds on DART simulations has been recently explored [114]. However, this has not been implemented in our study. Atmospheric conditions such as water content and aerosols are highly variable over a day. They influence the amount of radiation reaching the ground and consequently, Tmrt. However, in the case of Singapore, there is not much variation in terms of water content. The annual average of relative humidity is 84.0%. Therefore, we only included real-time (local) AOD observations obtained from the NASA AERONET website for each time step simulated.

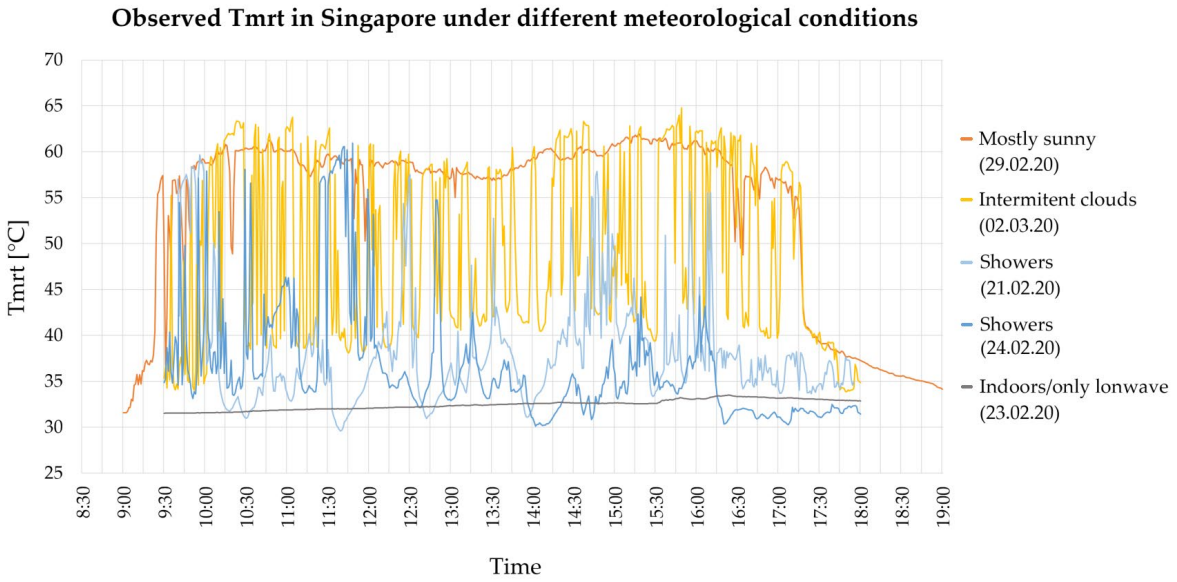

Figure 7. Observed Tmrt under different meteorological conditions in Singapore over a two weeks' period.

Secondly, the designation of optical properties was merely based on site inspection and matching with the closest material existing within the DART database, this, however, is a source of uncertainty since the spectral library of DART might not well represent the actual characteristics of the surfaces of our study area. An overview of the spectral signatures of construction materials and vegetation used in our simulations can be found in Appendix D. The correct consideration of optical properties of surface materials plays an important role in the radiative budget and thus, on Tmrt. To obtain a more accurate representation of optical properties, spectral signatures could be collected using a spectroradiometer and measuring the emissivity of the surfaces in the actual site. Unfortunately, we did not have access to such equipment. A detailed methodology for the derivation of spectral signatures of urban materials through emittance and reflectance spectroscopy can be found in Kotthaus et al. 2014 [115].

Thirdly, the variation of surface temperatures impacts pedestrian Tmrt, particularly in sunny conditions. This is expected since in sun hours the intensity of Tmrt is primarily driven by shortwave radiation. The influence of longwave emission tends to decrease with the distance between the emitting surface and the absorbing human body. The sensitivity analysis to changing the surface material of the ground showed that the ground material greatly influences Tmrt. For instance, the maximum difference of Tmrt observed between the five materials was 7.5 °C when surface temperature = 20 °C. This difference decreases to 5 °C if the surface temperature equals 60 °C. A possible reason for the underestimation in the areas with no direct shortwave radiation is that the surface temperatures obtained from UT&C energy balance model were obtained considering all the hours with a cloudiness of less than 50% over the time period from 1 May 2013 to 30 April 2014. This resulted in relatively lower surface temperatures compared to the actual surface temperatures occurring on a day with no cloud cover.

Fourthly, the accuracy of LAI retrievals from indirect methods relies on the integrity of the data used and on the retrieval technique. The retrieval of biophysical properties of vegetation has received particular attention in recent years, nevertheless, important gaps still exist for example in the estimation of LAI of heterogeneous tropical vegetation and for individual urban trees [42]. Further field investigations on the relationship between LAI and under-canopy Tmrt would help to validate and improve the predictions of our proposed method. In our study of Tanjong Pagar, Singapore, a uniform

LAI value was assumed for all the trees on the site. If local LAI/LAD data becomes available, for instance, retrieved from ALS [102], this information could be assimilated. Additionally, more evaluation sites are required to further assess the robustness of our method under different vegetation and urban settings, and in different climatic zones.

Finally, our method currently provides Tmrt at pedestrian level (1.5 m above the ground). Mapping 3-D Tmrt for instance on facades, balconies, and elevated terraces could be possible since Tmrt is computed per vertical column of voxels of the scene. This would require selecting the voxels in proximity to walls and roofs and ignoring the empty spaces where a person could not stand. Despite the advantages of using DART to perform analysis at different scales, a high level of detail over large scenes will result in long computation times. Therefore, the user must balance the trade-offs between scene size, level of detail, and computation time. A table with examples of computation times is provided in Table A2. With the continuous increase in computing power, this technical limitation will continue to decrease in the coming years.

3.5. Conclusion

The increasing availability of data on urban areas opens up new possibilities for detailed analysis in terms of urban microclimate and thermal comfort. Affordable laser scanners are being developed, opening opportunities for a wide range of research on the processing and data retrieval for urban 3-D mapping. This unprecedented increase of data and computation capacity highlights the need for more detailed simulation tools and methods for planners and designers to evaluate the performance of existing areas and to assess future designs under different climatic scenarios. This study explored the potential of using the 3-D physically based RTM DART to model Tmrt. We presented a new method for the estimation and mapping of Tmrt at different scales with a detailed consideration of surface materials and vegetation. The field evaluation showed good agreement between modelled and field estimated Tmrt. The impact of LAI on pedestrian Tmrt was explored as part of the sensitivity analysis. The results indicate a reduction of up to 38.2 °C Tmrt under the canopy when LAI = 5.5 compared to an "exposed" setting. This highlights the importance of using accurate vegetation properties for simulations. The sensitivity analysis showed consistency across different resolutions and changing simulation parameters. We demonstrated a potential first application of our proposed method. Our approach can be used to visualize locations in need of interventions, to help optimize climate-sensitive urban design, and to support urban microclimate and outdoor thermal comfort studies when combined with adequate simulation tools for wind analysis and energy balance models.

A correct designation of surface temperatures is crucial to avoid erroneous simulations and wrong conclusions of the study. In future work, we will explore coupling our method with a 3-D energy balance model such as DART EB [116] for a more precise designation of surface temperatures and a detailed calibration of input parameters. Additional validation exercises in different urban settings and other climatic regions would contribute to improving the robustness and applicability of this newly proposed method.

Quantifying the influence of urban design, construction materials, and vegetation on Tmrt can be helpful in evaluating urban planning scenarios aiming at reducing heat stress in existing urban areas, promoting enhanced thermal comfort in future developments, and contributing to reducing energy consumption for cooling systems. Future research could, for instance, explore the effect of building morphology and urban patterns; which species to plant and their optimal spatial arrangement such as in street-tree scenarios; as well as the effect of construction materials on Tmrt by using the existing DART spectral database or by adding the actual spectral information of the materials found on the site of interest.

3.6. Acknowledgements and funding

The authors would like to thank the DART team of CESBIO (CNES, CNRS, IRD, and University of Toulouse) for the consistent support of the DART model. Special thanks to Professor Wong Nyuk Hien (Building Department, National University of Singapore) for providing the Net radiometer devices used for field evaluation. We acknowledge the Singapore Land Authority for providing the LiDAR data and Naika Meili for providing the surface temperatures derived from the UT&C model the authors appreciate the valuable remarks and suggestions from anonymous reviewers.

This research was conducted at the Future Cities Laboratory, Singapore-ETH Centre, which was established collaboratively between ETH Zurich and Singapore's National Research Foundation (FI 370074016) under its Campus for Research Excellence and Technological Enterprise Programme. Shanshan Wei is funded by the Singapore National Parks Board (Nparks) project "Remote Sensing for Urban Tree Management: Species Classification and Health Monitoring".

4. Automatic delineation of individual tree crowns in a tropical urban park: assessment of a new deep learning algorithm over different spectral and spatial resolutions

Maria Angela Dissegna*t [1,2], Shanshan Wei[3], Hans Emil Atlason[4], Tiangang Yin[5] and Adrienne Grêt-Regamey [1,2]

[1] Future Cities Laboratory, Singapore ETH Center
[2] Chair of Planning of Landscape and Urban Systems, ETH Zurich
[3] Singapore–MIT alliance for Research and Technology, Singapore
[4] Department of Electrical and Computer Engineering, University of Iceland, Reykjavik, Iceland
[5] Earth System Science Interdisciplinary Center, University of Maryland, College Park, MD 20740, USA;

Keywords:

Individual tree crown delineation
Very High resolution
UAV hyperspectral
Deep Learning
Convolutional Neural Network
Tropical Vegetation
Urban Park

Submitted, *IEEE Journal of Selected Topics in Applied Earth Observations and Remote Sensing (2024).*

Abstract

Detecting and mapping the location and extent of individual tree crowns is a valuable parameter for forest monitoring and park management tasks such as tree counting, growth, health inspection, species classification, yield predictions, and biodiversity and ecosystem function assessments. A number of methods for instance segmentation of trees exist. However, their accuracy may be hard to replicate when image acquisition and pre-processing differ. Furthermore, the diversity of physical characteristics, seasonal variation, and environmental conditions in the forest makes it impossible to have one method that fits all.

This study presents a new fully convolutional neural network (FCNN) to delineate individual tree crowns (ITC) automatically. The performance of the approach was evaluated over different spatial and spectral resolutions of satellite and hyperspectral unmanned aerial vehicle (UAV) imagery of a highly diverse tropical urban park. The highest delineation accuracy was obtained using the UAV image B37-69-196 at 0.1 m resolution, with a binary segmentation accuracy of 85.54 % and a relative delineation accuracy of 59.87%.

Based on the experimental results, the proposed method is applicable to delineate trees in highly heterogeneous settings using both satellite or UAV hyperspectral data. Our method is better suited for satellite data when considering the data volumes and the pre-processing steps required to deal with very high-resolution hyperspectral imagery.

4.1. Introduction

Monitoring the status of individual trees is essential for various ecological, environmental, economic, and social reasons. It enables us to make informed decisions, protect our natural resources, and address the challenges of a changing climate and urbanization. Monitoring the status of individual trees has gained relevance in park management practices such as tree counting, growth monitoring, yield predictions, tree health, early-stage plant stress, and biodiversity assessments. Effective monitoring of vegetation status requires characterizing leaf biochemical traits and canopy structural traits across space and over time. Quantitative remote sensing has proven effective in parametrizing biophysical, biochemical, and physiological variables such as leaf area index, chlorophyll content, and fraction of absorbed photosynthetic active radiation [117][118][42][119]. These variables provide input data for automated monitoring approaches, particularly when evaluated over time and at the individual tree level. Therefore, the individual tree crown (ITC) delineation is a useful product for such fine-scale analysis. It provides information about the exact location and extent of trees. In other words, the ITC delineation is the base for further analysis based on region properties which combine radiometric and spatial information.

High-resolution remote sensing data has been successfully applied in mapping the canopy of urban trees [120][121][122][123], and recent studies have successfully identified individual trees over highly diverse tropical forests [124] and over broad-leaf forests [125]. However, these studies often need more description of the characteristics of the individual trees at larger scales, which is often required to support park management decisions [126]. One of the major issues for individual tree detection and further individual tree crown delineation tasks is the parameterization of a chosen algorithm to a specific context. The variety of conditions in terms of vegetation composition, planting scheme, climatic zone, and management practices makes it hard to use existing approaches directly as a one-fits-all solution. Due to this high contextual variability, it is common to obtain inconsistent results when applying existing algorithms to a new study area. Trees vary significantly in age, shape, spatial arrangement, and curation within urban environments. The complex and heterogeneous land cover also challenges the individual tree crown delineation. These conditions have made designing, parametrizing, and applying algorithms challenging, particularly in urban areas [127].

A variety of passive remote sensing methods for ITC delineation has been developed addressing landscapes with different degrees of complexity ranging from homogeneous plantations such as Oil Palm and coniferous forests to more complex vegetation structures found in deciduous forests, tropical forests, mixed forests, and more recently, urban forests [128]. Common image processing methods include spectral analysis, texture analysis, edge detection and edge enhancement, object segmentation, morphological analysis, blob analysis, local maximum filtering, image binarization, scale analysis, template matching, semi-variogram computation, scale-invariant feature transform, alley following, between- tree shadow identification, region grouping, watershed segmentation, multi-scale segmentation, and 3D modelling. The performance of these methods largely depends on the degree of variation of crown size and crown overlap, particularly in high stem density (crowded) situations.

Unmanned aerial vehicles (UAVs) can provide appropriate temporal and spatial resolution images to produce suitable datasets for mapping individual trees in more diverse forested areas and in urban settings [129]. In this context, several methods have been proposed based on histograms and thresholding, object-based image analysis, and multiresolution segmentation [130][131][132]. Methods based on a combination of UAV photogrammetric point clouds and hyperspectral imaging [38], as well as hyperspectral imaging and LiDAR [133,134] have achieved particularly high accuracy in individual tree detection, classification, and, in some cases, individual tree crown delineation. Furthermore, the combination of airborne hyperspectral and LiDAR data has proven effective in estimating individual-

tree morphological and physiological traits in a spatially explicit and consistent way at large scales [118]. These growing opportunities for detailed vegetation mapping come with several challenges regarding the affordability of multi-sensor platforms, increased data volumes and computational loads, and more diverse data structures with increasing dimensions (spatial, temporal, spectral), often featuring complex relationships [135]. Data dimensionality reduction techniques such as Principal Component Analysis (PCA), independent component analysis, and optimum index factor are increasingly used to deal with high volumes of data produced by using multi-source remote sensing and for fine-scale analysis [136]. A review of hyperspectral band selection methods can be found in [137].

Approaches incorporating deep learning methods such as Convolutional neural networks (CNN) achieved state-of-the-art results with high robustness even over a vast study area [138]. For instance, Brandt et al. (2020) mapped the crown size of 1.8 billion individual trees whose crown size was more than 3 m2 over a land area that spans 1.3 million km2 in the West African Sahara, Sahel and sub-humid zone, using sub-metre-resolution satellite imagery and a deep learning algorithm [139]. CNNs are increasingly used in different applications in the field of remote sensing due to their capability to learn spatial translation-invariant features [135][138] [139][140][141][142][143][144][145]. A summary of the advantages and potential of deep learning in earth observation science can be found in [146]. CNN applications include automatic classification, object detection, semantic segmentation, and, more recently, instance segmentation. Compared to image classification and object detection tasks, which do not delineate the shape or contour of a target, semantic segmentation assigns a class label to each pixel in an image, thus potentially capturing the form and size of an object more accurately [147]. Semantic segmentation approaches include *U-Net* [148], *SegNet* [149], and *FC-DenseNet* [150] and have been used for a variety of mapping tasks ranging from plant species, plant communities, deadwood to tree species in an urban context [124][140][151][152][153]. Semantic segmentation CNNs built on the U-Net architecture are effective since they conserve the spatial reference by memorizing the pixels that caused activations in earlier stages of the network and forwarding it to an output segmentation map. In the context of individual tree crown delineation, instance segmentation aims to detect individual things, such as individual plants or plant elements, and segment their spatial extent. Instance segmentation combines object detection and semantic segmentation [135]. Instance segmentation requires a more sophisticated collection of reference data (labels), which involves identifying individuals and delineating their explicit spatial extent [135]. Studies on individual tree characterization have frequently used manual tree crown delineation as an input feature to train the detection algorithms [154][155] or used existing tree inventory data as training to parameterize the segmentation algorithm [156]. Despite the potential utility of instance segmentation, few studies have used instance segmentation for individual tree crown segmentation [157][158]. One of the most popular algorithms for end-to-end instance segmentation is *Mask-R-CNN* [159]. The Mask R-CNN is a framework commonly used to detect objects in an image while generating a high-quality segmentation mask for each instance. It comprises a two-step approach, including an initial region proposal subject to a segmentation branch, followed by the localization and classification of the feature maps.

Similar to semantic segmentation, fully connected layers are used to create masks at the original resolution of the input imagery. The applicability of Mask R-CNN in the field of forestry is still at an early stage. Mask R-CNN has been effective in detecting and mapping the spatial extent of non-overlapping individual trees [160], as well as in accurately delineating tall trees in a tropical forest using red-green-blue (RGB) imagery and LiDAR-derived 3-D data [161]. However, Mask R-CNN failed to delineate a significant proportion of trees, partially attributed to the high degree of overlap between trees. Despite their potential, there are challenges associated with using CNNs for individual tree

delineation, such as the need for high-quality training data, addressing class imbalance (since trees are often a minority class in images), and handling complex backgrounds.

Additionally, model performance may vary depending on the specific dataset and environmental conditions. To effectively use CNNs for individual tree delineation, it is essential to employ appropriate data preprocessing techniques, select or design a suitable CNN architecture, fine-tune the model on target datasets, and regularly update it to account for changing environmental conditions. Additionally, incorporating other geospatial data sources, such as LiDAR or hyperspectral imagery, can complement CNN-based delineation efforts, enhancing accuracy and reliability.

Our study presents an FCNN approach for object instance segmentation to perform individual tree crown delineation over different spatial and spectral resolutions of WorldView2 satellite and UAV hyperspectral imagery of a tropical urban park. Since none of the existing methods could deal with our UAV hyperspectral data, we aim to provide an approach to use this information. Our proposed method, InTree-CNN, segments individual trees from the background and predicts a distance from the delineation of edges of individual trees. This distance information is subsequently used as input to a watershed algorithm [162] to label each tree with a unique ID.

4.2. Materials and Methods

4.2.1 Study Area

Our study area is located at the Bishan-Ang Mo Kio Park, a tropical urban park in central Singapore, as indicated on the left side of Figure 1 . Singapore has a tropical climate with dense, diverse, fast-changing, and often heavily managed vegetation. The most prominent tree species planted in the park are Samanea Saman, Tabebuia Rosea, Khaya Senegalensis, Peltophorum Pterocarpum, Pterocarpus indicus, and Syzysium grande. Aerial surveys were carried out on the park's east side using a hyperspectral camera mounted on a UAV platform shown on the right side of Figure 1.

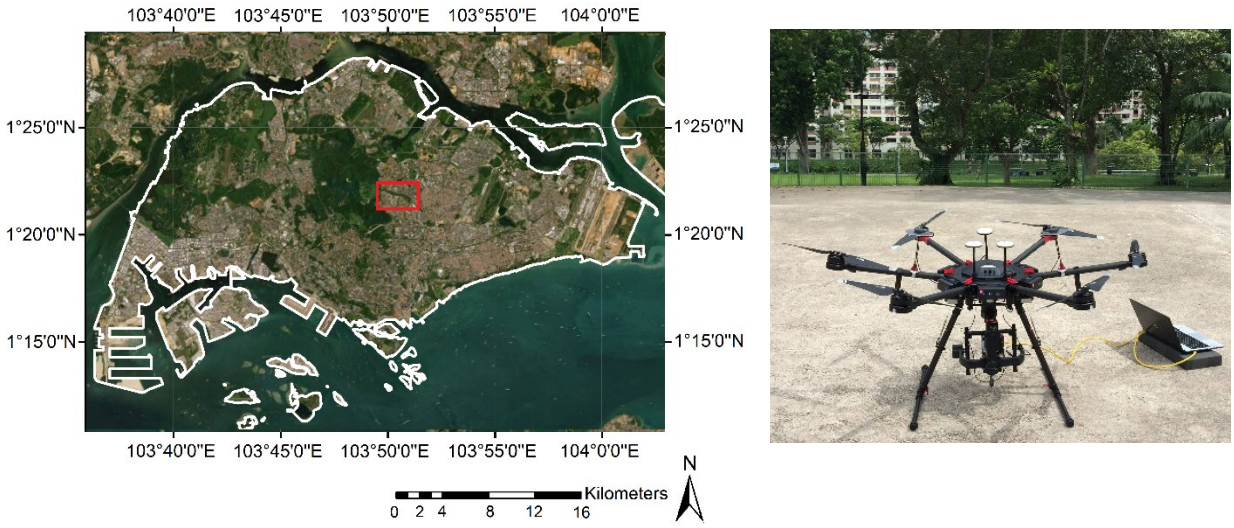

Figure 1. (left): Location of the study area. (Right): UAV platform setup.

4.2.2 Data collection

The datasets consist of (1) atmospherically corrected WorldView2 satellite image at 1.2 m and 0.5 m resolution acquired on 23-12-2017, (2) one hyperspectral data cube at 0.1 m resolution acquired on 10-10-2020, and (3) sets of manually delineated tree crowns created with the guidance form field inspections and established park databases (provided by NParks) matching each of the satellite and UAV datasets. In the case of WV2 imagery, the rater delineated tree crowns using the 0.5 m resolution

image. The manually delineated tree crown polygons were converted into raster and resampled to match the spatial resolution and pixel alignment of their corresponding hyperspectral and WV2 images.

4.2.2.1 WV2 Satellite imagery

The satellite imagery was pre-processed using ENVI software using the following functions: "WV2 Radiometric calibration" [73], "Fast Line-of-Sight Atmospheric Analysis of Spectral Hypercubes (FLAASH)" atmospheric correction [74], and "SPEAR" Orthorectification.

4.2.2.2 UAV hyperspectral imagery

The hyperspectral data cube was collected using a Headwall NanoHyperspec push broom scanner (lens' focal length: 12 mm; spectral bands: 270; wavelength range: 400- 1000 nm; pixel pitch: 7.4 μm; pixels per scanline: 640). The sensor was mounted on a DJI Matrice 600pro UAV using a DJI Ronin-MX gimbal to provide mechanical stabilization to the sensor. A Headwall GPS/IMU was attached to the scanner for orientation tracking with an accuracy rating of 2/2/2.5 m (x/y/z), 0.1/0.1/0.3° (roll/pitch/yaw) at a sampling rate of 4 Hz. These data were used subsequently for the geometric rectification of the images.

The flights were carried out at an altitude of 150 m, flying at a speed of 5 m/s with a ground sampling distance (GSD) of 9.2 cm, resulting T in a scanning swath of 59.2 m with 30% overlap for adjacent flight paths. A radiometric reference tarp with three reflectance panels (sized 3 x 3 m and calibrated as 11/32/56% reflectivity) was used to calibrate the scanned images. With this system configuration, the UAV-based imaging system had a total mass of 12.2 kg and could sustain nearly 12 minutes to map each mapping site per battery charge. The image acquisition parameters setup, storage, and data transfer were carried out using the software package Hyperspec 111 v3.0.

The pre-processing steps included converting from digital numbers to radiance and subsequently to reflectance, orthorectification, and mosaicking. For ease of processing, the captured data cubes were stored contiguously as segments of a fixed length of 2,000 scanlines per segment. The raw data segments were first converted to radiance values, which were then converted to reflectance values by using the radiance values of the calibration tarp in the image. Headwall's software package provided fine adjustments for imaging parameters to produce the best possible camera model for map projection. The digital elevation model (DEM) offset was adjusted so that the image resolution is always close to 9.2 cm. The view-angle-related adjustments (pitch/roll/yaw) can only be verified after long computations; this trial-and-error is unavoidable and time-consuming. Therefore, to improve the efficiency and accuracy of georeferencing, the view-angle-related adjustments were skipped entirely; instead, ground control points (GCP) from Google Maps were used to construct affine transformations to project the orthorectified data segments to the final reflectance map. As the UAV flies in opposite directions between the adjacent tracks, contiguous segments in different directions were orthorectified and mosaicked into separate tracks without view-angle-related adjustments. Each track was inspected to find evenly spread ground points that had unmistakable counterparts in Google Maps, or vice versa, and these points (more than three) were used as GCPs to establish correspondence between the raster space and the map space. Singular value decomposition (SVD) was used to fit the six parameters for the affine transformation, which was used to project the separate tracks to the final hyperspectral image. Functional segments were processed individually and finally mosaicked as a map shown in Figure 2.

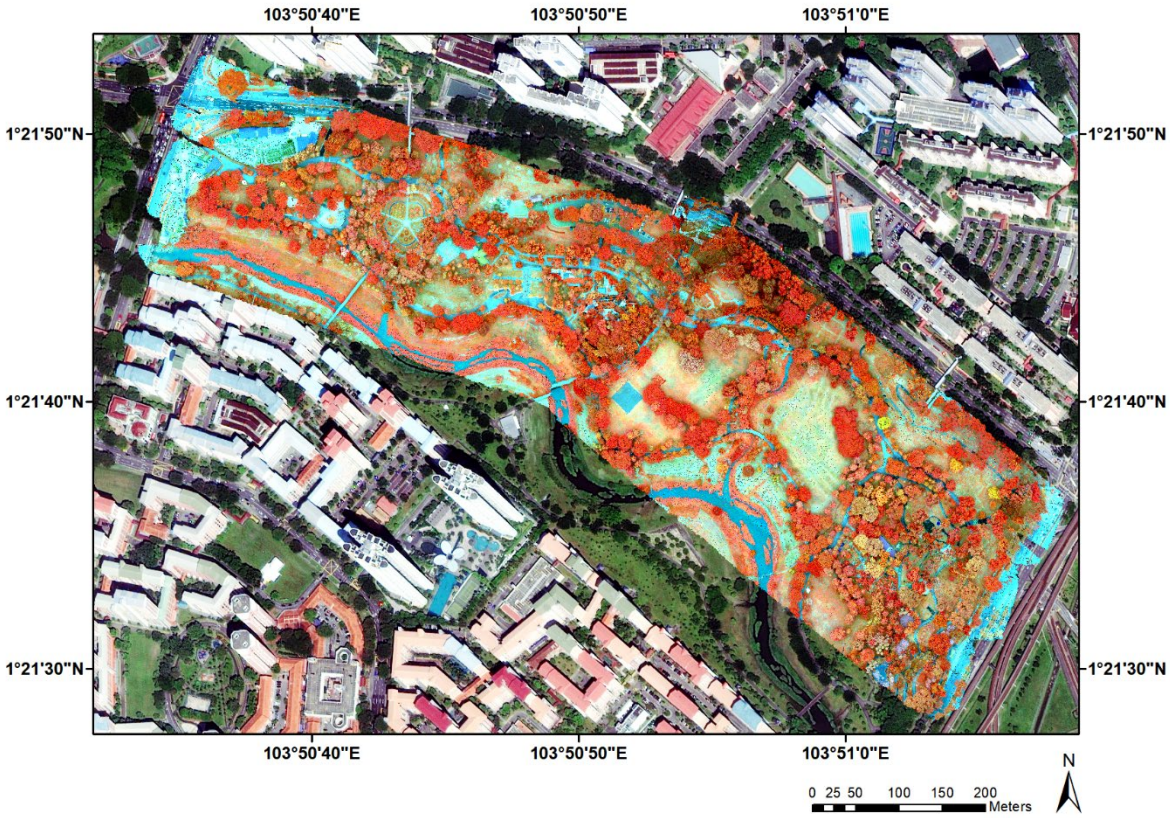

Figure 2. Display of false color composite (544.3 nm - 726.6 nm - 840.0 nm) of UAV hyperspectral imagery collected over Bishan- Ang Mo Kio Park.

A principal component analysis (PCA) was applied over the hyperspectral data cube to reduce the high data volume and overcome computational limitations. Three visually coherent images explaining the highest variance were selected among the resulting PCA images. To further accentuate the variation among trees in the principal components of the image, a second approach was to run a PCA using statistics obtained from the regions in the image containing trees and then apply it over the entire image. Additional 0.1 m resolution images were generated based on the UAV dataset. The first, corresponding to R-G-B-NIR bands (479.9 nm - 551.0nm - 660 nm, 833.4 nm; B# 118-69-37-196); and the second, two selections of three bands which produced the highest visual variation among trees:

544.3 nm - 726.6 nm – 840 nm (B#66-148-199)
475.4 nm - 573.2 nm - 833.5 nm (B#35-79-196)

Due to computer memory limitations, only three bands of the UAV dataset could be used at a time. Therefore, the R-G-B-NIR dataset was run twice (R-G-B and NIR-G-B). The characteristics of the datasets used in this study are reported in Table 1.

Table 1. Characteristics of the image datasets

Source	Date of acquisition	Spatial resolution	Spectral Resolution
WV2 Multispectral	23-December-2017	2 m	8 WV2 Bands
WV2 Pansharpen	23-December-2017 and	0.5 m	4 Bands (R,G,B & NIR)
Manual delineation of tree crowns (WV2)	23-December-2017	0.5 m	-
UAV hyperspectral	10-October-2020	0.1 m	479.9 nm - 551.0nm - 660 nm -833.4 nm 4 Bands (R-G-B-NIR)

UAV hyperspectral	10-October-2020	0.1 m	544.3 nm - 726.6 nm - 840.0nm (Visual selection)
UAV hyperspectral	10-October-2020	0.1 m	475.4 nm - 573.2 nm - 833.5nm (Visual selection)
UAV hyperspectral PCA (full image stats)	10-October-2020	0.1 m	3 Bands representing 97% of all bands (PCA)
UAV hyperspectral PCA (only trees stats)	10-October-2020	0.1 m	3 Bands representing 97% of all bands (PCA)
Manual delineation of tree crowns (hyperS)	10-October-2020	0.1 m	-

4.2.3 InTree-CNN

The proposed CNN architecture (Figure 3), hereafter referred to as the InTree-CNN is based on the U-net architecture [148] and includes two output paths corresponding to the tree segmentation and the distance-to-edge, respectively. The manually delineated datasets are used to create two new images: one corresponding to the segmentation of trees (Figure 4, a) and another corresponding to the delineation of the edges of the trees. A morphological distance transform is used to create an image that shows the Euclidian distance-to-edge of every pixel to the power of 0.1 (Figure 4, b). Subsequently, the images are subdivided into patches of 512 x 512 pixels with a stride of 256 x 256 pixels.

The method was applied to images of different spatial and spectral resolutions indicated in Table 1. The InTree-CNN was trained using two loss functions: a weighted cross-categorical loss function for segmenting trees from the background and a mean square error (MSE) loss function for predicting the distance-to-edge. The MSE loss function had a weight α relative to the other loss function (weight of 1). The hyperparameters used for training the InTree-CNN were set as follows: number of epochs 150, the batch size was 12, and α=1 for the first 50 epochs and α=20 for the subsequent 100 epochs. After training InTree-CNN, the final steps involved assembling the predicted patches and carrying out a watershed algorithm [162] on the distance-to-edge image to segment individual trees. Only areas where trees existed, according to the predicted tree segmentation, were considered individual trees. A morphological opening was performed to remove small or thin objects. Similarly, a morphological closing was performed to fill holes in segmentations that could result from the removal of small objects. Due to the resolution difference, the opening and closing were performed for one iteration on satellite data and five iterations on the hyperspectral data.

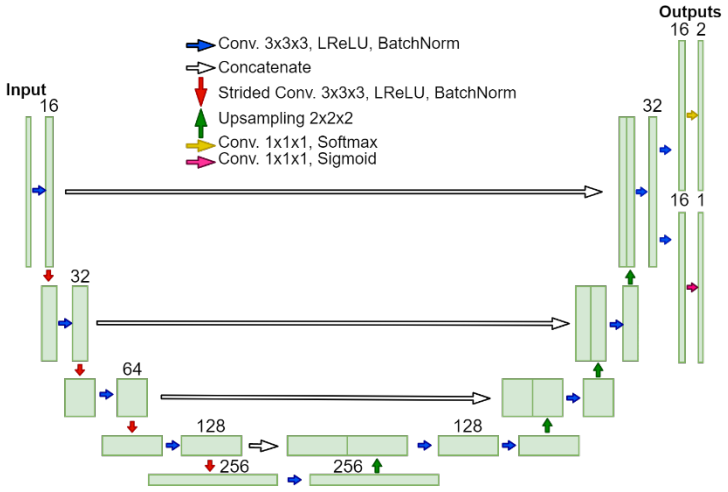

Figure 3. The proposed CNN architecture (InTree-CNN)

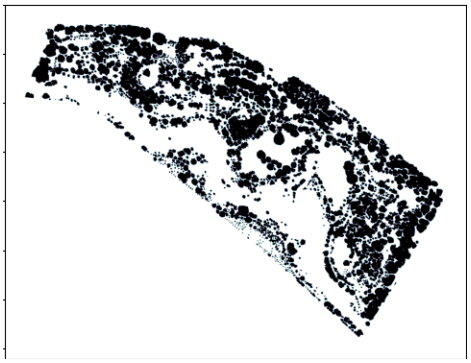
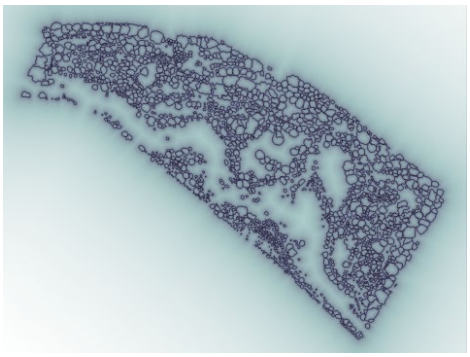

Figure 4. (a)Tree segmentation ground truth; (b) Distance to edge

4.2.4 Neural network training and validation

The accuracy assessment was performed for each image subset corresponding to 33.3% of the data not used during training. The accuracy of ITC delineation was first evaluated using the following metrics for both the *binary segmentation*, that is, the ability to discriminate trees vs background (Table 2.), and the *instance segmentation*, which is the actual detection of individual trees (Table 3 and 4).

- **Dice coefficient:** A measure of the overlap between a ground truth tree crown and the predicted tree crown. When many predicted crowns correspond to a single ground truth, the predicted instance is chosen as the one that most overlaps with the ground truth crown.
- **Recall**: The fraction of segmented pixels in the predicted instance that matches the ground truth instance.
- **Precision:** The fraction of segmented pixels in the predicted instance that exists in the ground truth instance.

Secondly, the degree of over-segmentation (a subdivision of a crown into multiple predicted segments) and the under-segmentation (predicted segments that correspond to more than one manually delineated crown) were assessed in terms of overlap between each tree crown of the predicted segmentation dataset against the ground truth dataset and vice versa. The results are represented as follows:

- O**ver-segmentation** (blue bars 2- 10)**:** number of predicted crowns overlapping each individual "ground truth" tree crown.
- **Under-segmentation** (orange bars 2- 10)**:** number of crowns in the "ground truth" overlapping with each crown in the prediction dataset.
- **Commission error** (blue bar in zero)**:** Number of false positives.
- **Omission error** (orange bar in zero): Number of false negatives.
- **One-to-one match:** Predicted segmentation vs ground truth (blue bar in one) and ground truth vs predicted segmentation (orange bar in one).

Figure 5 shows an example of the evaluation metrics for assessing the accuracy of the individual tree crown delineation. The evaluation results for each tested image are reported in Appendix A. The visual representation of results and a comparison between outputs can be found in Appendix B and C.

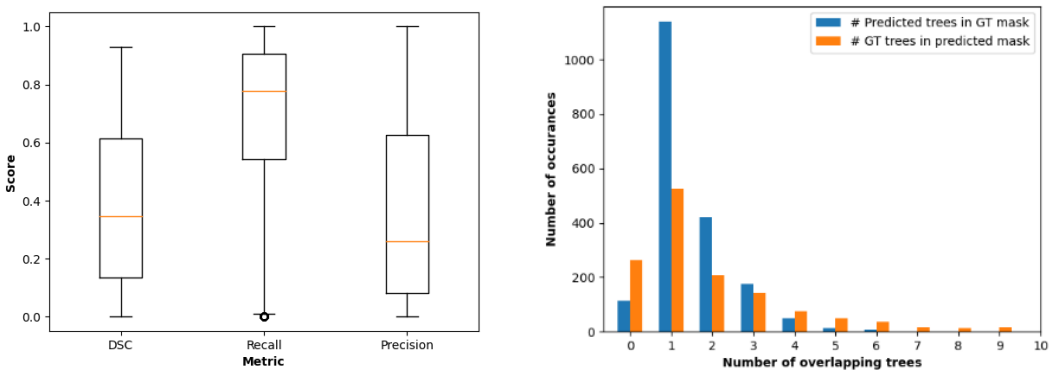

(a) (b)

Figure 5. (a) Dice, Recall and Precision; (b) Under-segmentation and over-segmentation.

4.3. Results

A visualization of the individual crown delineation over the WV2 satellite image at 0.5 m resolution is shown in Figure 6. A total of 2865 trees were manually delineated. 2713 trees were predicted at 0.5 m resolution, while 2123 trees were predicted at 2m resolution.

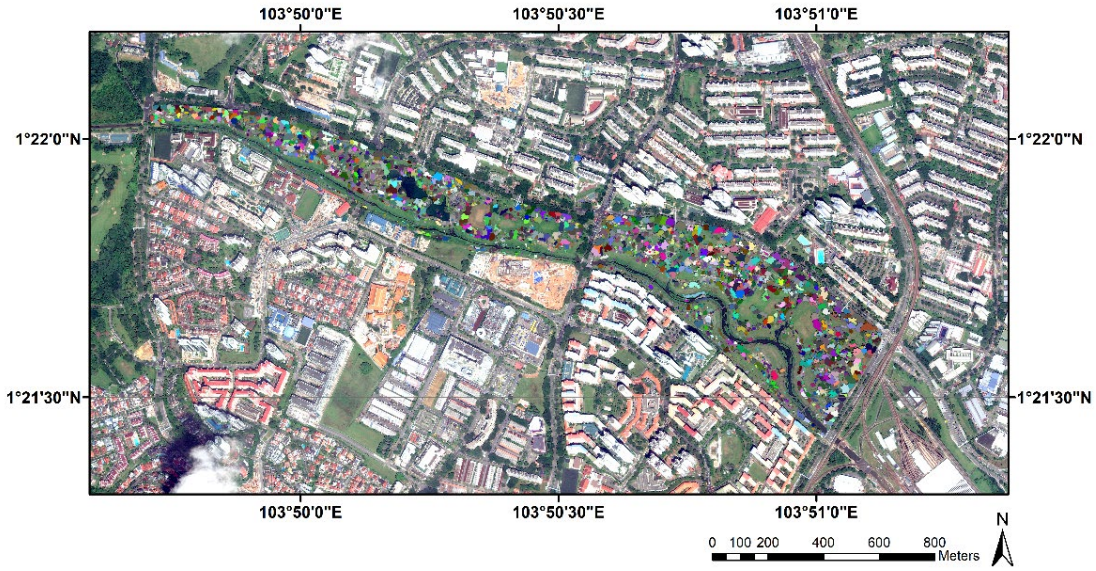

Figure 6. Visualization of results for WV2 satellite image at 0.5 m resolution.

The binary segmentation results in table 2 show that our method differentiates tress from background with high accuracy. The highest dice obtained was 0.8582 on the 0.1 m resolution image B37-69-196, followed by a dice of 0.8554 at 0.5 m and 0.8419 at 2 m. The instance segmentation results are reported in Table 3 for the satellite imagery at 0.5 m and 2 m resolution and in Table 4 for the different band combination of the UAV hyperspectral imagery.

Table 2. Binary segmentation results (tree vs background)

Image	Dice	Precision	Recall
Satellite WV2 2 m	0.8419	0.8400	0.8713
Satellite WV2 0.5 m	0.8554	0.8351	0.8488
UAV 0.1 m B35-79-196	0.8487	0.8510	0.8464

UAV 0.1 m B66-148-199	0.8546	0.8645	0.8449
UAV 0.1 m B37-69-118	0.8180	0.8438	0.7937
UAV 0.1 m B37-69-196	0.8582	0.8690	0.8477
UAV 0.1 m PCA trees stats	0.8214	0.8247	0.8181
UAV 0.1 m PCA full image stats	0.8378	0.8443	0.8313

Table 3. Instance segmentation results from satellite imagery. Average and standard deviation of Dice, Recall, and Precision for the 0.5 m and 2 m satellite images.

	WV2 0.5 m	WV2 2 m
Average Dice	0.4586 ± 0.2889	0.4401 ± 0.2827
Average Recall	0.7315 ± 0.2550	0.6593 ± 0.2923
Average Precision	0.4492 ± 0.3467	0.4445 ± 0.3482

Table 4. Instance segmentation results from UAV hyperspectral imagery. Average and standard deviation of Dice, Recall, and Precision for each hyperspectral dimensionality reduction / channel selection method.

	B35-79-196	B66-148-199	B37-69-118 (RGB)	B37-69-196 (BGNIR)	PCA trees stats	PCA full image stats
Average Dice	0.5528 ± 0.2710	0.5845 ± 0.2557	0.5345 ± 0.2537	0.5987 ± 0.2582	0.5508 ± 0.2664	0.5641 ± 0.2602
Average Recall	0.6688 ± 0.2948	0.6581 ± 0.2811	0.6046 ± 0.2904	0.6708 ± 0.2775	0.6207 ± 0.2984	0.6413 ± 0.2932
Average Precision	0.6584 ± 0.3418	0.6958 ± 0.3196	0.6670 ± 0.3244	0.7013 ± 0.3203	0.6858 ± 0.3377	0.6755 ± 0.3278

When comparing the predicted instances against manually delineated crowns, the majority of mismatches were found to be shrub areas delineated as if they were trees; followed by grass areas exhibiting an abrupt change in reflectance (Figure 7). Different degrees of disagreement in the definition of individual tree crown boundaries are observed primarily in larger crowns, which usually overlap with other trees that have similar reflectance.

Figure 7. Predicted tree crowns not matching with ground truth (red).

When evaluating the accuracy of boundary delineations, it is important to mention that the likelihood for a predicted instance to exactly match a manually delineated crown is very low. Overall, predicted crowns have a tighter fit. The difference in crown area between predicted and ground truth can be attributed to the roughness of the manual delineation compared to a computerized determination of boundaries. The amount of false positives tends to be lower when image resolution increases (Figure 8). The smallest crown area to be detected is 1.25 m^2. While the manual delineation dataset omitted some of these small trees, the CNN was able to detect them. An overestimation of crown size is observed in the satellite image at 2 m resolution (Figure 9). The two main reasons are 1) part of the tree

shadow being included as part of the crown and 2) contiguous trees of similar reflectance being generalized as one tree. A lower overestimation of crown size is observed when using the 0.5 m resolution image. At 0.5 m resolution it can be observed that tree shadows are no longer considered to be part of the crown, even if shadows were often included in the manually delineated data used in the training process. Evaluating the results of the UAV imagery, a higher accuracy was obtained using UAV image B37-69-196.

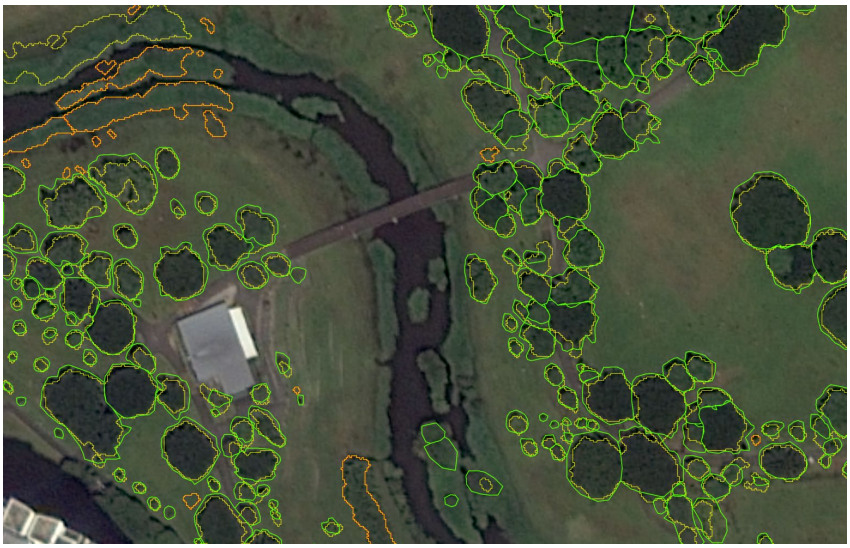

Figure 8. Satellite image at 0.5 m resolution. Manually delineated tree crowns are indicated in green, predicted crowns in yellow, and false positives in orange. Omitted: green instances with no corresponding prediction.

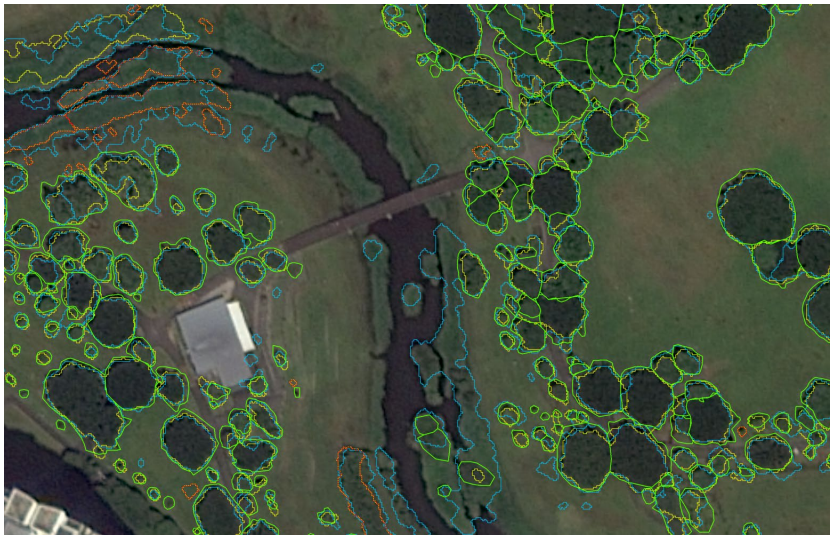

Figure 9. Manually delineated tree crown indicated in green, predicted (at 0.5 m res.) in yellow, false positive (at 0.5 m res.) in orange, omitted: green alone. Predicted crown (at 2 m res.) indicated in blue.

4.4. Discussion

This research investigated the effectiveness of a proposed FCNN approach in automatically outlining individual tree crowns within a tropical urban park. Our approach's effectiveness was assessed across various spectral and spatial resolutions of satellite and UAV imagery. The most accurate delineation

was achieved using the UAV imagery bands 37-69-196 at a resolution of 0.1 m, yielding a binary segmentation accuracy of 85.54% and a relative delineation accuracy of 59.87%.

Several sources of inaccuracy exist at the different stages of the process and are explained hereafter. The first source is issues related to data acquisition, particularly in UAV data collection, and the second is discrepancies in the manual delineation. Third, we had limited training data compared to the high degree of variation of vegetation found in our study area. Irregularities in the data stitching of UAV imagery were common in our dataset, mainly due to sudden wind during the survey and inaccuracies in the GPS/IMU system. When comparing UAV data to satellite data, the first is more affected by changes in illumination during the survey due to scattered cloud cover and alternating viewing angles due to the aerial survey path. Due to flight time restrictions, the area mapped using the UAV platform is considerably smaller than the total area of Bishan Park, which is covered entirely in the case of satellite data. However, more individual trees were manually identified in the UAV images than in the Satellite due to the increased spectral and spatial resolution. The increased level of detail provided by the 0.1 m resolution images came with the downside of overcomplicated crown boundaries to be manually defined.

The manual delineation of individual crowns used for the training and validation dataset is not always consistent due to systematic errors and intra-rater and inter-rater variability. On the one hand, overlapping trees with similar reflectance characteristics make it hard for the rater to define the crown boundaries accurately. This issue is prominent when drawing at a lower resolution. On the other hand, when drawing over the 0.1 m resolution image, there are discrepancies in the crown shape caused by differences in zoom or not cutting into the crown between branches. The manual delineation of small trees, such as palm trees, has not been done consistently. In some cases, some were grouped, others were defined as individuals, and others were omitted. Training with images that are not entirely labeled means that the CNN will learn that certain areas with trees are, in fact, not trees, affecting the overall detection accuracy.

Both manual and automatic tree crown delineation are challenging in dense, diverse, and multi-layered tropical canopies. Furthermore, a high level of heterogeneity can be found in tropical urban parks, where trees are heavily influenced by planting patterns, man-made arrangements, and curation. For instance, they may be associated with flower beds or in contrast to grass, herbaceous shrubs, concrete, or asphalt ground, among other materials. The higher level of variability increases the number of training samples required. In our case, we had limited training data compared to the high degree of variation. A common problem in CNN-based architectures is the issue of scale, meaning that if the CNN is trained on images where trees are of a specific size, it struggles to predict on images where trees are relatively smaller or larger as a proportion of the whole image [179]. Therefore, there is much room for improvement by increasing the amount of training data.

The use of high-accuracy ground truth data is crucial in the development and validation of instance segmentation methods. However, manually delineating trees at very high resolution is a tedious and time-consuming task. A potential way to improve the accuracy of the ground truth data to overcome some of the limitations mentioned above would be to create a synthetic dataset [160]. For instance, a 3-D radiative transfer model could be used to simulate satellite and UAV data of varying spectral and spatial resolutions, on which each individual tree's exact location and extent is known. This would enable the creation of larger training datasets, with a range of combinations between understory vegetation, ground material, tree species, size, and planting densities. Furthermore, creating such an artificial dataset could assist in the systematic identification of key parameters that enhance the adaptability of the CNN to different types of images, as well as to different forest conditions in complex and heterogeneous landscapes. A CNN trained on synthetic data could subsequently be fine-tuned on real data (manually delineated) in a setting specific to the area of interest. Although not included in the

scope of this study, we recognize that 3-D information such as a digital surface model constructed either from RGB images using structure from motion technique or more detailed vertical structure obtained from LiDAR scanning would contribute towards higher accuracy of individual tree crown delineations [161]. This information should be taken into consideration when creating synthetic training datasets. Our method is better suited for satellite data when considering the data volumes and the pre-processing steps required to deal with very high-resolution hyperspectral imagery. Further evaluation of dimensionality reduction/ band selection methods is encouraged to deal with the high volumes of these particular data.

4.5. Conclusion

This study explored the applicability of a proposed FCNN to delineate individual tree crowns in a tropical urban park automatically. The performance of our method was evaluated over different spectral and spatial resolutions of satellite and UAV imagery.

Based on the experimental results, the proposed method applies to delineating trees in highly heterogeneous settings using satellite or UAV hyperspectral data. Our method is better suited for satellite data when considering the data volume and the pre-processing steps required to deal with very high-resolution hyperspectral imagery. Further evaluation of the code using different training and imagery sources and the creation of synthetic datasets would be needed to increase its robustness. The methodological framework and CNN code resources are available upon request for other researchers to test, repeat, and adapt our method over different forest ecosystems.

5. Synthesis

5.1 Summary of the key findings

Despite the technological advancements in research, the complexity and heterogeneity of the urban built environment have imposed limitations on applying traditional micrometeorological theory in urban areas [163]. Novel spatial datasets can now provide information at the fine resolution required for urban microclimate studies. However, gaps exist in the data assimilation and simulation capabilities of current modelling tools. For instance, existing modelling approaches often fail to provide a detailed analysis of the 3-D interactions between complex urban surfaces. Remarkably, the vegetation component and the optical properties of urban surfaces have been treated in a rather simplistic manner.

To bridge those gaps, this work's first objective was to create 3-D datasets containing spatial information required to feed state-of-the-art modelling tools. These datasets were retrieved from a variety of remote sensing platforms, such as satellite and UAV imagery, as well as aerial and terrestrial LiDAR scanning point clouds. This included the development of a methodology to create detailed urban scenes of any location of a city based on commercially available data presented in chapter two; and a fully convolutional neural network approach for the automatic delineation of individual tree crowns presented in chapter four. These datasets were used as input to the simulations presented in chapters two and three.

Second, rather than promoting DART, this thesis intended to highlight the benefits of exploring the applicability of an advanced radiation transfer model as opposed to simplistic models. An advanced 3-D radiative transfer model such as DART possesses excellent modelling capabilities besides the initial intended use, which is the forward simulation of sensor observations. In this research, the DART model was successfully adapted to perform an analysis of the effects of urban form and subtle variation of vegetation on the radiative budget and to map the spatial distribution of Tmrt in any given urban configuration at different scales. The key findings of the research work presented in this thesis are summarized hereafter in reference to the research questions presented in chapter one.

- **How can we effectively model the radiative budget in urban environments across various scales while accounting for the diverse optical and geometric characteristics of vegetation and buildings?**

Effective modelling of the radiative budget in urban environments requires an integrated, multidisciplinary approach that considers physical, optical, and geometric characteristics of vegetation and buildings. By combining data analysis, simulation, and practical implementation, strategies can be developed to mitigate the urban heat island effect and create more comfortable, sustainable urban environments.

The DART model has several advantages over existing models as it handles radiation across a wide spectrum, simulates broadband radiation through narrow bands, is versatile with various surface optical properties (isotropic or anisotropic), and can simulate vegetation using biophysical characteristics. The research work presented in chapter two explored the applicability of the DART model as a tool for detailed assessment of the radiative budget of 3-D urban landscapes at a high level of detail in terms of spatial features and advanced parameter setting possibilities. The entire methodology, from retrieving 3-D urban scenes from high-resolution satellite imagery to the simulation stage using DART was demonstrated in a case study of common urban typologies of Singapore. The evaluation compared the impact of urban typology, ground material, and the effects of changing leaf area density (LAD) on the radiative budget of different urban scenarios. This comparison showed that highly urbanized landscapes with no tree cover can absorb up to four times more than a densely vegetated "natural" landscape. The simulation results show good agreement when compared against

net radiometer data obtained from a local flux tower in Singapore. This confirms the suitability of using our proposed methodology to compute an accurate radiative budget for any urban/vegetation configuration. Therefore, not only does it serve as a diagnostic tool, but the methodology can also be used to assess the effect of mitigation strategies of different proposed designs. Furthermore, after the successful development and test of the presented methodology, the three-dimensional radiative budget outputs were further used to compute Tmrt as described in chapter three. This was possible through the adaption of the three-dimensional outputs to provide the six-directional components required for the Tmrt equation. By doing so, it was possible to evaluate the influence of different vegetation types, tree species, and their distribution pattern both on the radiative budget and the Tmrt at different scales.

- **What is the impact of varying vegetation properties, urban geometry, and optical characteristics of both elements on the Tmrt?**

Urban environments are highly complex and consist of multiple interacting factors. The interplay between building configurations, surface materials, and vegetation is intricate and nonlinear [164]. Modelling allows us to simulate these interactions and better understand their combined effects on Tmrt.

The approach presented in chapter three on adapting DART to map Tmrt facilitates the concurrent assessment of vegetation-related parameters to discern differences between plant species, biophysical properties, and planting regimes. For instance, if we consider a pedestrian standing directly exposed to the sun in Singapore at 4:00 PM, they would experience a Tmrt of 64.1°C. However, if the same individual stands beneath a Khaya Senegalensis tree with a leaf area index (LAI) of 5.5, the Tmrt would reduce to 25.89°C, and with an LAI of 0.1, it would be 31.15°C. This highlights that strategically positioning and selecting vegetation is crucial to minimize the radiation entering urban spaces and achieve the desired reduction in Tmrt. The radiative properties of urban surface materials significantly influence the radiative budget and, thus, the Tmrt and the overall microclimatic conditions. For example, a Tmrt variation of up to 15°C can be observed when comparing the impact of surface materials like white concrete walls versus glass. Additionally, light materials tend to increase Tmrt due to their higher reflectance. Furthermore, the response in terms of Tmrt to various urban surface materials in the longwave domain was nearly linear to changes in their surface temperature. This highlights that choosing construction materials with properties that minimize heat absorption and radiation can lead to a reduction in Tmrt, improving thermal comfort. However, the extent of the reduction will also depend on other factors, such as the local climate and the overall building design.

Modelling tools provide a predictive capability that allows urban planners, architects, and researchers to forecast the impact of design and material choices on Tmrt. This is particularly important for assessing the effectiveness of potential solutions for mitigating urban heat islands and enhancing outdoor thermal comfort.

- **To what extent deep learning methods can assist in the instance segmentation of individual trees in a dense and mixed urban park?**

Chapters two and three highlight the importance of incorporating detailed information of vegetation at the fine scale. However, not many remote sensing products readily exist for fine-scale analysis, such as individual-tree-scale over tropical vegetation. Deep learning methods have the potential to significantly enhance the instance segmentation of individual trees in a dense and mixed context such as an urban park [146]. Their ability to automatically learn and adapt to complex visual patterns in the data makes them valuable for accurately delineating and distinguishing trees within such challenging environments. However, the extent of their effectiveness depends on factors such as the quality and quantity of training data, model architecture, and the specific characteristics of the urban park in

question. Deep learning methods have shown promising results, but their performance varies based on the complexity and diversity of the park's vegetation and overall conditions.

The delineation of ITC serves various practical purposes in environmental and ecological studies, forestry, urban planning, and urban microclimatic modelling. By delineating individual tree crowns, researchers can gain a more detailed understanding of trees' distribution, condition, characteristics, and ecological roles in various environments, which in turn supports informed decision-making and sustainable resource management. Compared with traditional image analysis techniques, using CNN models for ITC has two major advantages. Firstly, CNN models have transfer-learning ability, such that knowledge learned from one site can be transferred to another site, resulting in model generalizability. In contrast, most image analysis models rely on pre-defined parameters, which need to be manually adjusted when applied to a different environment or dataset. Secondly, CNN models detect trees at an object level by learning patterns from hierarchical combinations of image features. While other techniques describe tree objects solely based on reflectance or morphological features, CNN models provide a more comprehensive representation of tree appearance with abstract visual characteristics.

To address the case study of a tropical urban park in Singapore, a new fully convolutional neural network to delineate individual tree crowns automatically was developed and presented in chapter four. Furthermore, different spatial and spectral resolutions of satellite and hyperspectral UAV imagery of a highly diverse tropical urban park were evaluated and presented in chapter four. As demonstrated by the experimental results, the proposed method effectively delineates individual trees in highly diverse environments, utilizing satellite or UAV hyperspectral data. The highest delineation accuracy was attained using the UAV image B37-69-196, which had a resolution of 0.1 meters. This resulted in a binary segmentation accuracy of 85.54% and a relative ITC delineation accuracy of 59.87% in delineating individual tree crowns. Currently, the method is better suited for satellite data due to considerations such as data volume and the pre-processing steps necessary to manage very high-resolution hyperspectral imagery.

5.2 Limitations

Measuring the impact of vegetation on outdoor thermal comfort in a tropical city is a complex task. Outdoor thermal comfort is influenced by a complex interplay of factors, including air temperature, humidity, wind speed, and solar radiation. For instance, introducing urban greenery can raise humidity levels and block wind circulation, which might lead to a decrease in outdoor thermal comfort in an already hot and humid environment. Moreover, vegetation plays a role throughout the day and across seasons, necessitating a comprehensive analysis of its influence on outdoor thermal comfort across these time frames to gain a complete understanding of the potential advantages it offers [165].
This thesis solely studied the interactions of electromagnetic radiation between urban and vegetated surfaces. To comprehensively account for the interplay between various types of vegetation, their characteristics, and their respective impacts on outdoor thermal comfort, an energy balance model would be required in order to quantify the exchange of energy between different components in the outdoor environment, including vegetation. This is essential for understanding how vegetation affects air temperature, humidity, and heat transfer [106].

One of the limitations of the presented approaches for radiative budget and Tmrt simulation is the simplification in terms of surface material designation. This simplification was made due to the interest in using direct information from a satellite imagery dataset (overall shape, location of the objects, and few land cover classes). This level of detail can be useful for large-scale analysis, which was the case presented in chapter two, but is not optimal for analysis at finer scales. However, detailed information on the desired surface construction materials and/or vegetation can be incorporated when testing

design scenarios, as demonstrated in Chapter Three. Similarly, fine-scale 3-D architectural features can be well represented and their effect simulated [56][57].

A second limitation is the lack of data on local vegetation properties over larger extents. However, with advances in retrieving vegetation properties from remote sensing data, this information could be added to increase the accuracy of the simulations [42]. Other factors, such as leaf clumping coefficient and leaf angle distribution, could also be considered for simulation [166]; however, they are more difficult to measure in the field and to further specify their distribution over individual trees in an urban scene. Discrepancies exist in the retrieval of vegetation properties when different methodologies are applied. As an attempt to bridge this gap, a study assessing three indirect methods for estimating leaf area density and LAI of individual trees was conducted within the research group to understand the extent of variability over relevant tree species in Singapore [42]. However, the applicability of these methodologies over different geographic regions or vegetation regimes remains to be determined.

Third, despite the increasing number of studies applying CNN models to ITC tasks with different data and in various forest environments, comparing CNN models for different ITC delineation approaches across studies remains a challenging task. Firstly, when using multispectral or hyperspectral images, adjustments are required to handle higher dimension inputs than standard RGB images. These adjustments can be categorized into data dimension reduction and model structure modifications. The former approach simplifies high-dimensional data to accommodate the 3-channel input expected by pre-trained CNN models, while the latter approach modifies the architecture of a CNN model to allow direct input of higher-dimensional data. Secondly, variations in stand density, crown characteristics, and backgrounds are some of the factors that affect the performance of CNN models under different forest types. Some proposed solutions such as adding more training samples, using higher-resolution images, or data fusion may not be necessary for one forest type but could be crucial for another.

Simulation tools have proven effective in evaluating the current situation and hypothetical scenarios. However, field evaluation is required to warrant the proposed methods' robustness. The access and affordability to the required instrumentation might limit such evaluations. To overcome these limitations, a collaborative study was carried out to evaluate the performance of the standard 150 mm black globe thermometer to provide Tmrt values in Singapore's hot and humid tropical urban area. Specific mean convection coefficients were derived by comparison with radiant flux measurements (shortwave and longwave) obtained from net radiometers. The analysis was performed over different weather conditions and considered different averaging periods. This work provides the possibility to improve the estimation of Tmrt in outdoor settings in a hot, humid, low wind speed and cloudy tropical region like Singapore by using a 150 mm black globe thermometer. The approach is simple and requires significantly less costs than radiation measurements [167].

The presented approaches are best suited for neighborhood-scale analysis at any desired location of a city or in order to test existing or designed scenarios with varying surface materials and vegetation properties. However, despite the advantages of DART to perform analysis at different scales, a high level of detail over large scenes results in longer computation times. Therefore, it is crucial to balance the trade-offs between scene size, level of detail, and computation time.

5.3 Relevance to science and society

Rapid urbanization, together with the projected rise in global temperatures due to climate change, is likely to increase temperatures in urban areas further. This poses adverse effects on the outdoor thermal comfort and health of urban dwellers. With thoughtful urban planning and sustainable design strategies, mitigating these effects and creating more liveable, comfortable, and sustainable urban environments is possible. The incorporation of vegetation into built environments, as well as the development of nature-based solutions as mitigation strategies, has gained interest worldwide.

However, evaluating vegetation's effects alone is insufficient without understanding the mutual influences between urban vegetation, anthropogenic activities, and urban climate. A quantitative understanding of the dynamic factors driving urban climate is needed. Such processes include wind, heat, water flow, and other natural processes, which can be modelled using appropriate simulation tools. Simulating the complex interactions between the built environment and the vegetation helps quantify the effect of different mitigation strategies against the UHI effect and, ultimately, contributes to enhancing outdoor thermal comfort. In this context of climate-sensitive urban design, modelling tools such as the ones developed in this thesis contribute to the assessment of the current state and the design process by anticipating the effect of alternative landscape designs. Thus, modelling tools are helpful to optimize the future spatial configuration of a city based on a set of specific set goals [12][13][14].

Implementing mitigation strategies against UHI requires planning, execution, monitoring, and recurrent maintenance, each of these factors having associated costs. Science-based tools are emerging as a cost-efficient way to both assist in the planning process and in the monitoring and management stages of the proposed mitigation strategies. For instance, an automatic system to monitor urban vegetation's health could provide a more comprehensive understanding of the conditions of the trees in a city; this, in turn, contributes to maintaining a good quality of green urban spaces at a lower cost. In other words, deploying automated monitoring approaches is highly valuable for government agencies to reduce labor-intensive tasks. The creation of such a monitoring approach requires initial data products such as the individual tree crown delineation so that changes in biophysical and biochemical properties could be studied over time at the individual tree scale. This research work contributed to the delivery of an initial dataset to aid the evaluation of the current state of urban vegetation, aiming to contribute to a more systematic monitoring over space and time.

Overall, the contribution of this research work was (1) the development of a methodology to evaluate better the influence of vegetation and other urban parameters on the radiative budget and Tmrt of urban landscapes; and (2) on the generation of the relevant spatial datasets to carry out advanced simulation/modelling/monitoring tasks. The outputs of this research are of interest to the fields of microclimate modelling, urban design, urban planning, ecosystem services, and remote sensing. Although the research is carried out in Singapore as a case study, the methodologies could be implemented to study any other tropical city or vegetation types using commercially available data.

5.4 Future research directions

Balancing the demands of urbanization with the need for thermal comfort is essential for the health and prosperity of urban residents and the long-term resilience of our cities. A variety of multidisciplinary approaches combining the fields of urban microclimate, architecture, urban design, computer science, and remote sensing are emerging at a fast pace with the aim at understanding the complex urban climate systems and human-environment interactions at finer temporal and spatial scales. At the same time, model outputs and their availability to the research community have increased thanks to the ever-growing computing and storage capacity. For instance, new trends in urban microclimate research focus on comprehensive assessments of human thermal exposure, intra-urban hazard distribution, and the development of lower-cost tools and comprehensive spread data collection methods [168].

The increase in availability of free and commercial remote sensing data, together with multi-sensor data fusion [169], enables the retrieval of novel datasets with detailed information on the three-dimensional heterogeneity of urban configurations, as well as on surface optical properties and vegetation properties. This fuels the development of new techniques for urban microclimate modelling at building to regional scales, producing urban climate parameters at high spatial and temporal resolutions. In this regard, the proposed methodology of using DART for 3-D radiative budget and Tmrt mapping opens up unprecedented possibilities to assimilate a wide range of parameters, either numerical or in the

format of spatial datasets, to provide a finer representation of the scenes of study. However, currently, most simulation software can rarely handle remotely sensing data or point cloud models directly [168]; therefore, further research on data interoperability is needed. Although many advancements have been made in the 3-D reconstruction of the built environment, the methods for reconstructing urban trees from remote sensing are still in their early stages. The need for detailed information, including geometric features and physiological characteristics of urban vegetation, has been highlighted repeatedly in recent research [170]. Additional validation exercises in different urban settings and other climatic regions would improve the robustness and broad applicability of the proposed methods to other climatic regions and urban contexts.

Since the publication of the articles presented in this thesis, some advancements have occurred which are directly related. Regarding the DART model, advancement has been made to include cloud cover parameters in the simulations. Clouds cover two-thirds of the Earth's surface and can be thick enough to influence the radiative budget. Their influence is particularly relevant when modelling tropical climates such as in Singapore. In this implementation, clouds are characterized by user-specified optical properties and vertical distribution and modelled as a layered one-dimensional medium that coexists with gases and aerosols [114]. This highlights the potential of DART to simulate irradiance on cloudy days accurately. This could potentially be used for a wide range of experiment applications on urban and vegetation studies since direct and diffuse Bottom of Atmosphere irradiance (BOA) in narrow bands are commonly required for such simulations. Another recent study presented a new reference model for outdoor radiative exchange based on the backward Monte Carlo method with many spectral and directional radiative transfer capabilities in complex urban canopies. The main advantages of this new model are found in its capability to represent the full complexity of urban geometry without leading to high computational cost while representing the relevant physical processes, e.g., scattering and absorption of radiation due to potentially cloudy or polluted air in between the buildings, spectral urban material reflectivity, and specular reflecting materials [171]. An interesting comparison could be made between the new approach based on the backward Monte Carlo method and DART, which is based on the Discrete Ordinates Method, since, as it is now, the main limitation of using DART is the prohibitive computation times when scenes become large. Other recent research advancements that are of relevance to the proposed methodology include: 1) approaches to retrieve surface optical properties from UAV or satellite data [172]; 2) retrieval of biophysical and biochemical parameters of vegetation [173] and 3) combination of SfM photogrammetry and instance segmentation for applications related to urban scene reconstruction and automatic recognition of buildings and distinct sub-elements [174][175]; 4) deep learning approaches for 3D mapping of urban landscapes [176] and 5) Coupling the presented adaption of DART with a 3-D energy balance (EB) model such as DART EB for a more precise designation of surface temperatures and a detailed calibration of advanced input parameters [177].

This research promotes advancements in the use of remote sensing technologies and machine learning in urban climate studies. The CNN approach developed has proven efficient in automatically mapping individual tree crowns over a tropical urban park using satellite and UAV hyperspectral imagery by examining the role of spatial resolution and spectral information for individual tree crown delineation tasks. The ITC is a vital product at the onset of fine-scale vegetation assessments. This innovation signalled the potential of AI and machine learning in addressing complex environmental challenges while further contributing to the understanding of vegetation's role in urban climate regulation. The methodologies developed in this research could be refined and combined with other remote sensing technologies for more accurate and comprehensive mapping and monitoring of urban vegetation and urban microclimate. Urban planners and policymakers can utilize such information to make informed decisions about city design and infrastructure development to mitigate the effects of urban heat islands and improve thermal comfort. As urban parks and green spaces become increasingly vital in urban climate regulation, methods such as these will play a pivotal role in their management and optimization.

The study presented on chapter four only focused on individual tree detection as opposed to classification or multiple individual species identification. Studies using multiclass detection are still rare. In plantation, natural, and urban forests, multiclass detection has been only conducted to differentiate classes within a single species, for example, palm trees with different health conditions [158]. Deriving a single class of trees from other forest types is challenging due to interference from surrounding trees and backgrounds. As a result, most natural forest or urban forest studies either choose a tree class that has a unique appearance (e.g. palm trees or diseased trees) or are undertaken in a small study area with a homogenous environment, relative to the broader area. For general class detections, a need for numerous high-quality training samples was reported in numerous studies, particularly for urban and natural forest applications [178–182]. Further research could focus on investigating multispecies ITC, single species ITC (other than diseased trees) within complex forest environments, and the impact of the number of training samples and their quality on general class detection tasks. As well as exploring data fusion approaches to take advantage of the characteristics of different types of remote sensing data; evaluate impacts of pre-training and parameter tunings and further improve data efficiency with customized sample approaches and synthetic samples. Techniques to generate synthetic tree samples are rule-based and designed by researchers' subjective understanding of tree features. Compared with hand-annotated data, these manipulation methods have the potential to artificially create more variance in the sample data and therefore improve the generalizability of the CNN model.

Integrating architecture and urban design with modelling approaches opens possibilities for the collaboration of multidisciplinary teams to explore the importance of design choices and foster performative scenarios. The evaluation of the performance of design scenarios relies on a continuous exchange of information between simulation tools and digital models. In this way, case studies can be tested and expressed in conjunction with digital models, workflows, simulations, and dynamic tools [183]. An example of this is the concept of an 'Ecosystem Services-Design Loop' developed within the "Ecosystem Services in Urban Landscapes project." This concept envisions a tool enabling designers and planners to predict the ecosystem services provided by a potential urban development. Simulation tools (UT&C, DART, and OpenFoam) are used to answer the question about the multiplicity of ecosystem services benefits of a new design in a particular landscape context [12][14][24][106]. The core idea of this project is that designing with a point cloud could assist the iterative exchange by repeatedly adapting the models based on the evaluation results using dynamic modelling tools [13]. The design is then improved in an iterative process that is guided by the results of the simulations as well as by knowledge about the local ecology [184], human-environment interactions such as park usage and visit frequency of urban parks [185], engagement with nature-related activities [186] and perception of urban vegetation types [187]. Furthermore, the widespread monitoring of the health of individual trees would be a significant step forward and could precede more accurate estimates of outdoor thermal comfort. Using these tools and information, planners and architects can quantify the impact of their designs on environmental performance, including such aspects as rainwater retention, air temperatures, and wind speeds thanks to the use of novel mechanistic modelling approaches [106][165]. The evaluation of the environmental impacts of different designs offers a powerful way to convince developers of the value of urban greening. This could directly contribute to the implementation of more holistic mitigation strategies to tackle the increasing environmental pressures that cities are experiencing at the present time [188].

From the social point of view, further understanding of the equity implications of urban heat mitigation strategies is needed, to ensure that vulnerable and disadvantaged communities benefit from these efforts, and are not disproportionately affected by extreme heat; as well as the assessment of the economic benefits and costs associated with urban heat mitigation strategies, considering factors such

as energy savings, reduced healthcare costs, and increased property values [189]. Interdisciplinary collaboration, data-driven analysis, and the integration of advanced technologies is essential for advancing research towards effective urban heat mitigation strategies for a more sustainable and resilient urban future[168].

6. Appendix

Appendix Chapter 2. Three Dimensional Reconstruction of an Urban Landscape to Assess the Influence of Vegetation in the Radiative Budget.

A. Parameters for Atmospheric Correction Using FLAASH Module

Image	Acquisition time	Date	Water web	Water column (Water web/4.11535369775)	Aerosol Angstrom	AOD	Initial Visibility [3.912/(AOD/2)]	MeanSunElev	Zenit angle (MeanSunElev + 90)	MeanSatAngle	Azimuth angle (-180 + MeanSatAngle)
P001	03:43:16.622660Z	14-Jun-2012	3.58	0.869913077	1.24	0.27	28.97777778	60.5	150.5	103.4	-76.6
P002	03:23:32.688322Z	25-Nov-2015	5.45	1.324309015	0.5	0.45	17.38666667	59.2	149.2	103.4	-76.6
P003	03:49:17.979495Z	18-Jul-2011	4.35	1.057017287	1.31	0.15	52.16	61.9	151.9	155	-25
P004	03:34:17.029274Z	23-Mar-2015	4.57	1.110475632	1.53	0.7	11.17714286	65.5	155.5	106.3	-73.7
P005	03:42:41.899876Z	8-Apr-2011	3.8	0.923371423	1.5	0.38	20.58947368	68.2	158.2	71.8	-108.2
P006	03:43:25.477834Z	8-Apr-2011	3.8	0.923371423	1.5	0.38	20.58947368	68.6	158.6	140.5	-39.5
P007	03:38:34.373855Z	19-Nov-2010	4.65	1.129915031	1.7	0.6	13.04	62.9	152.9	84.6	-95.4
P008	03:33:58.835479Z	17-Jan-2015	4	0.971969919	0.9	0.14	55.88571429	57	147	58.1	-121.9
P009	03:33:57.705150Z	23-Mar-2015	4.52	1.098326008	1.53	0.75	10.432	65.6	155.6	72.5	-107.5
P010	03:36:40.397901Z	19-Apr-2015	5.35	1.300009767	1	1.1	7.112727273	66.2	156.2	120.9	-59.1

Figure A1. Parameters for atmospheric correction using FLAASH module.

B. DART simulation parameters

Flux-tracking				
			Radiation-Radiative method	*Flux Tracking*
			Atmosphere radiative transfer TOA<->BOA	*Analytic model*
	Flux -tracking parameteres			*Default*
	Products			*Radiation budget products only*
	Spectral interval	spectral band		*mode , CW1.6, SB 2.8*
		Radiative Budget	…	
			Radiative budget unit	*W/m2*
			Radiative budget componets	*select the first six options*
			Scene element components	*select the four options*
Direction input parameters				
			Sun angles or date	*Exact date*
			Year	*2014*
			Month	*3*
			Day	*23*
			Hours	**To be set in sequence launcher tool*
			Local time	*yes*
			Time Zone (UTC)	*8*
Optical and temperatures properties				
	Lambertian	Ground	Property name	Ground
			2D lambertian database	*Lambertian_mineral.db*
			2D lambertian model	asphalt_road_gray
	Lambertian	Built	Property name	*Built*
			2D lambertian database	*Lambertian_mineral.db*
			2D lambertian model	*concrete_grey_new*
	Vegetation	Tree	Vegetation property name	*Tree*
			3D vegetation database	*Lambertian_Vegetation.bd*
			3D vegetation model	*leaf_deciduous*
	Temperature	Thermal function	Mean temperature	*300*
			Delta temperature	*0*
Earth Scene				
			Excaclty periodic scene	*Isolated scene*
			Whole or sub earth scene	*Whole*
			Whole earth scene Cell dimensions	*x and y 1m*
				z 1m
			earth scene dimensions	*x 620m*
				y 612m
			Ground optical property name	*Built*
			type of optical property	*lambertian*
			Geo location - Altitude of the DEM zero level	*0 m*
			Latitude	*1°*
			Longitude	*103°*
Earth scene: 3D imported object				
	Ponctual object			
		Object	DEM mode	*Defined by group*
			Possible symmetric repetitivity	*NO*
			Source file	*path of the .obj file*
		Geometric properties	Position	*x 310m*
				y 306m
				elev 0m
		Groups - Terrain	DEM mode	*Used as DEM*
			Use for computing LAI	*No conversion*
			Optial property name	*Built*
		Groups - Buildings	DEM mode	*Ignore DEM*
			Use for computing LAI	*No conversion*
			Optial property name	*Built*
		Groups - Vegetation		*Added using vegplots.txt*
				(Earth scene plots tab)
Atmospehere				
			Gas optical properties	*Tropical*
			Gas temperature profile	*Tropical*
			Gas O3 and other gases vertical profile	*Tropical*
	Aerosol	Aerosol properties		
			Aerosol optical properties	*Tropical_urbav5*
			Aerosol vertical profile	*Urbanv5*
			Aerosol Henyey Greenstein parameters	*Urbanv5*
			AOD multiplicative factor	*Retrieved from Aeronet for simulation date*

Figure A2. Parameters used for DART simulations.

C. Land cover map of Singapore

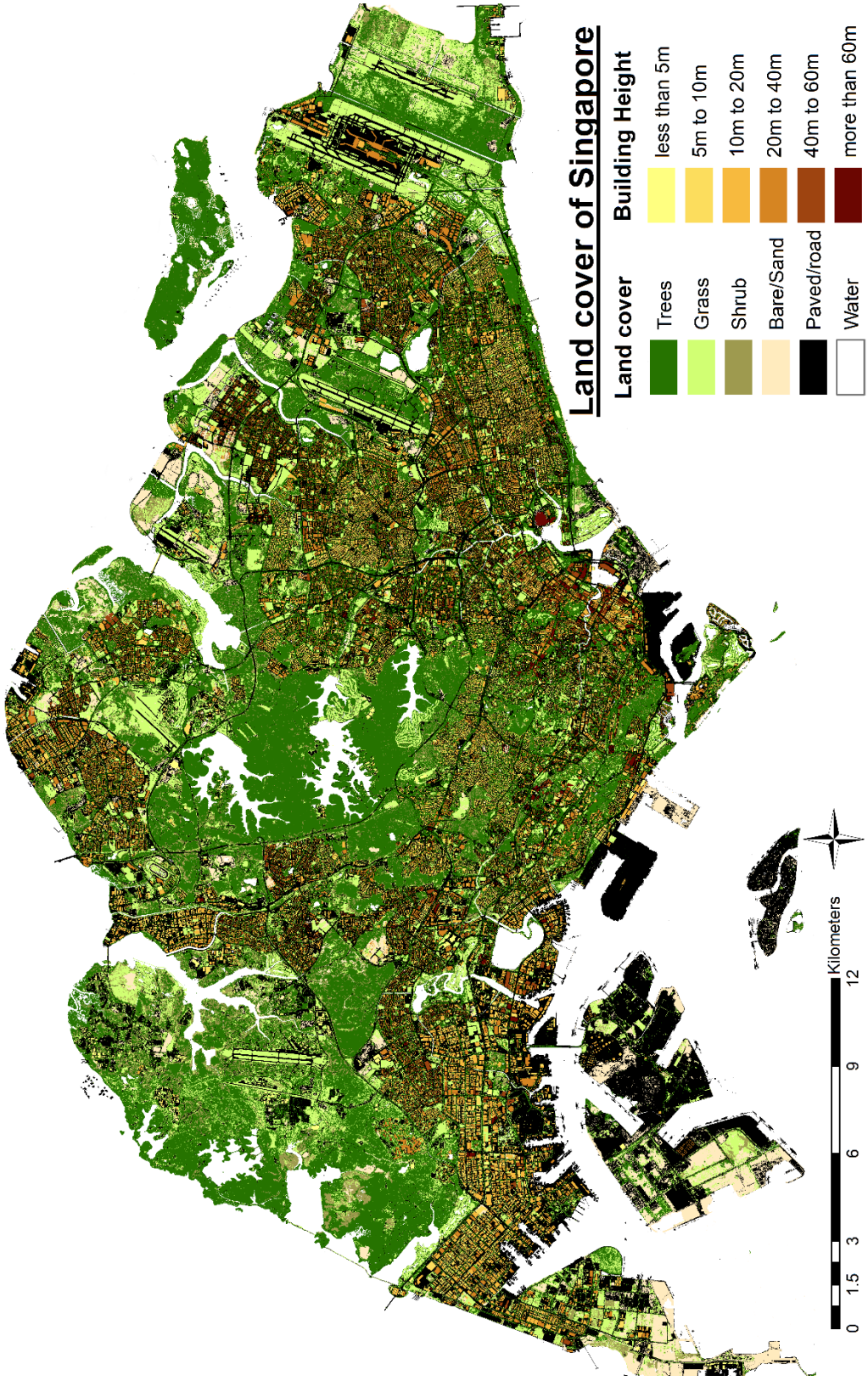

Figure A3. Land cover map of Singapore.

D. Spectral Reflectance of Construction Materials and Vegetation (from DART Database)

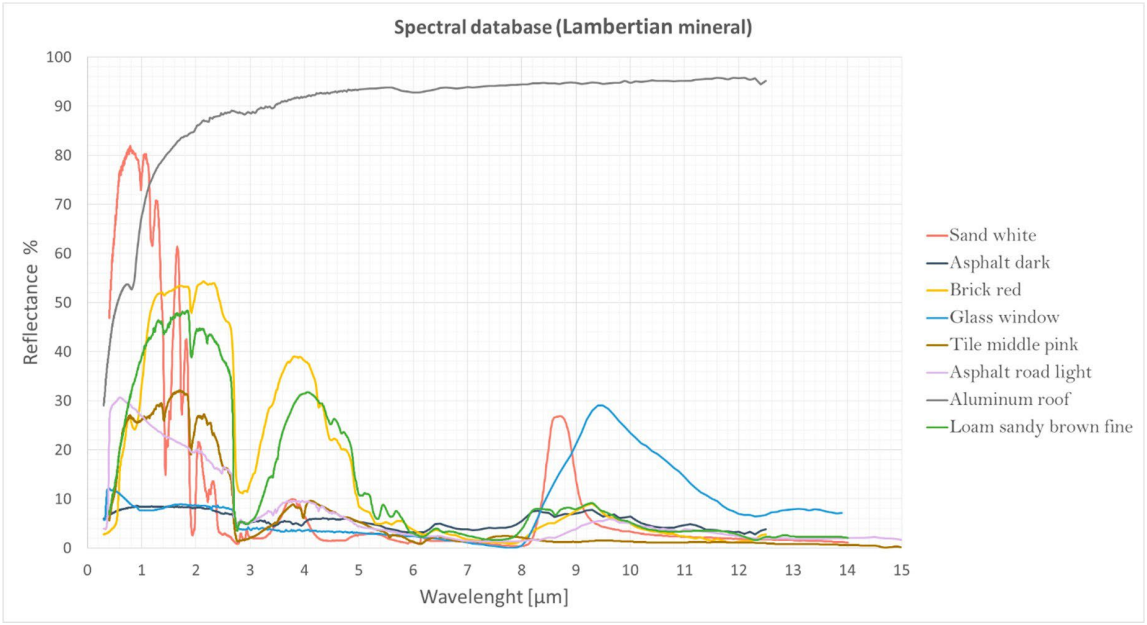

Figure A4. Spectral reflectance of construction materials from DART database

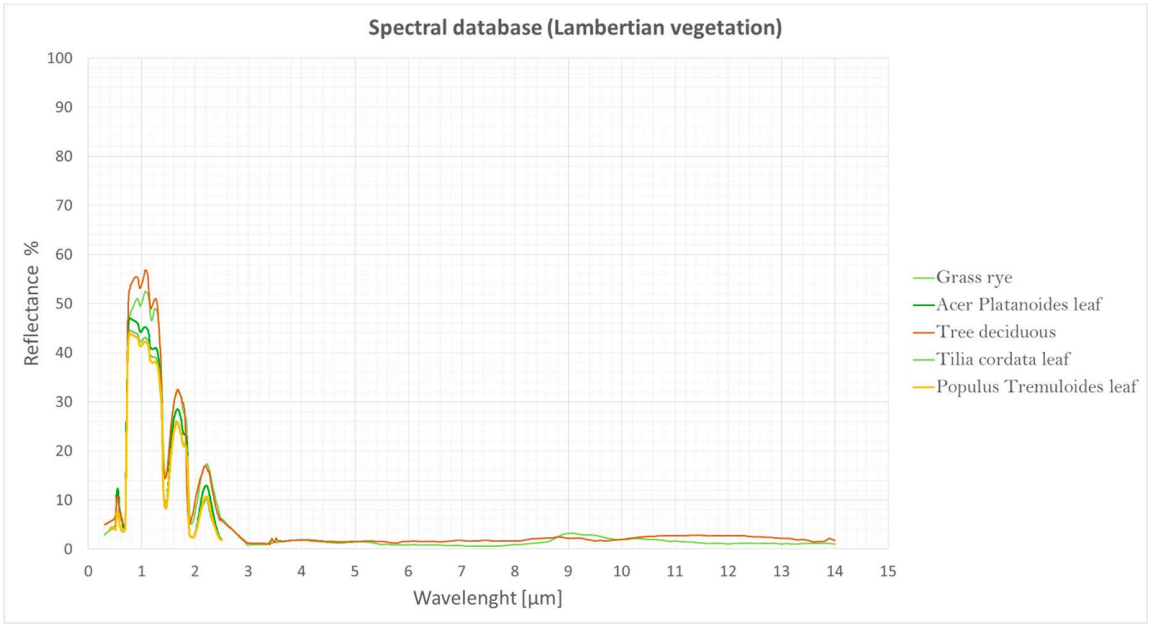

Figure A5. Spectral reflectance of vegetation from DART database

E. Effect of Different Ground Cover Materials on the Absorbed Shortwave Radiation by Ground and Buildings for Residential High Rise and Secondary Forest Typologies

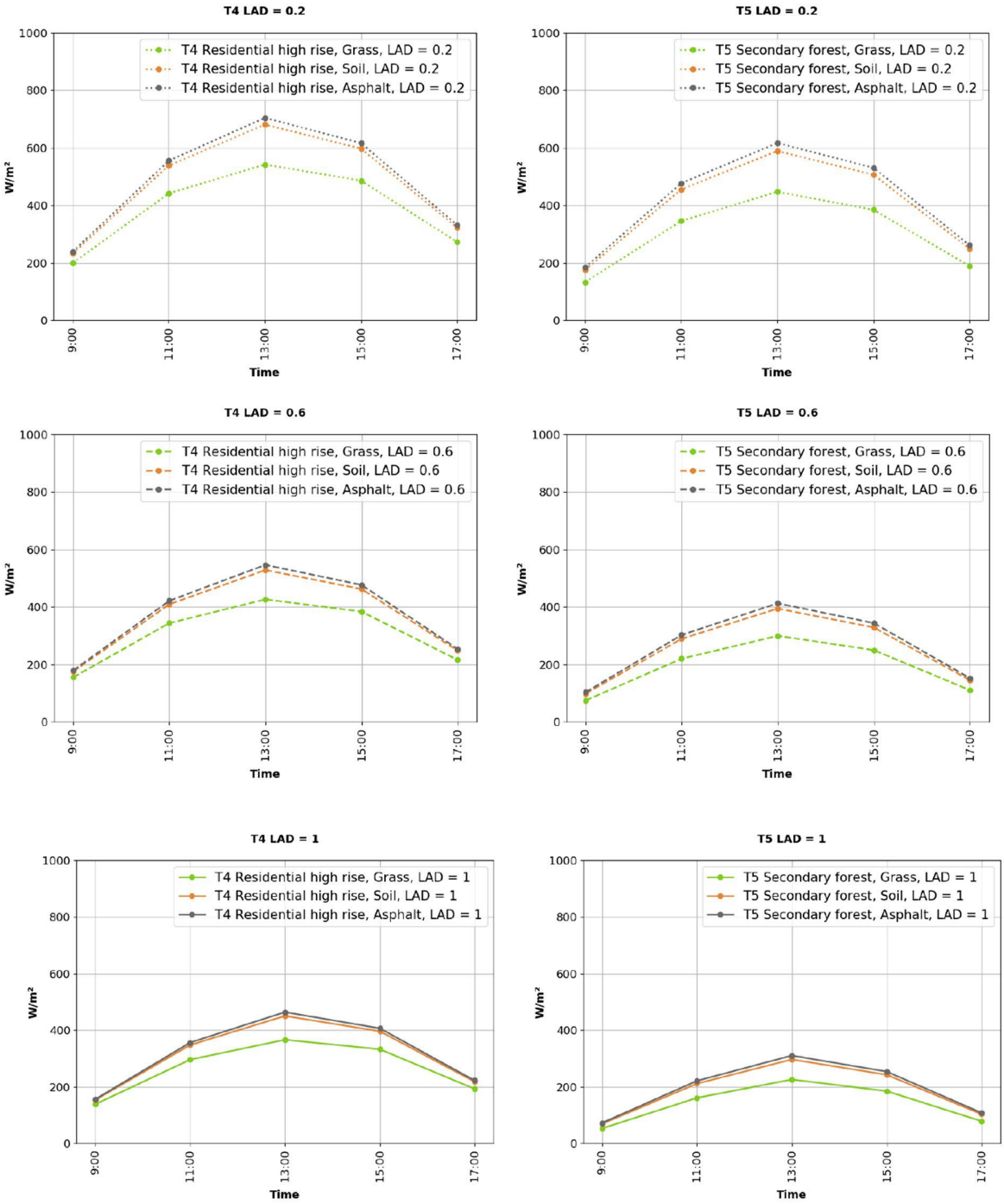

Figure A6. Effect of different ground cover materials on the absorbed shortwave radiation by ground and buildings for T4 and T5 typologies.

F. Simulation Results Summary

Typology	Ground cover	LAD				Code	Absorbed by buildings and ground at 13:00	Difference
T5	Grass				1.0	T5-G-1.0	225.53	0.00
T5	Soil				1.0	T5-S-1.0	296.55	71.02
T5	Grass			0.6		T5-G-0.6	299.43	73.90
T5	Asphalt				1.0	T5-A-1.0	310.33	84.80
T4	Grass				1.0	T4-G-1.0	366.09	140.56
T5	Soil			0.6		T5-S-0.6	394.27	168.74
T5	Asphalt			0.6		T5-A-0.6	412.54	187.01
T4	Grass			0.6		T4-G-0.6	426.28	200.75
T4	Soil		0.2			T4-S-0.2	446.97	221.44
T5	Grass		0.2			T5-G-0.2	446.97	221.44
T4	Soil				1.0	T4-S-1.0	450.37	224.84
T4	Asphalt				1.0	T4-A-1.0	463.89	238.36
T4	Soil			0.6		T4-S-0.6	528.25	302.72
T4	Grass		0.2			T4-G-0.2	541.84	316.31
T4	Asphalt			0.6		T4-A-0.6	546.30	320.77
T5	Soil		0.2			T5-S-0.2	589.02	363.49
T3	Asphalt			0.6		T3-A-0.6	602.90	377.37
T5	Asphalt		0.2			T5-A-0.2	617.07	391.54
T2	Asphalt			0.6		T2-A-0.6	702.42	476.89
T4	Asphalt		0.2			T4-A-0.2	704.40	478.87
T1	Asphalt				1.0	T1-A-1.0	708.37	482.85
T1	Asphalt			0.6		T1-A-0.6	740.34	514.81
T1	Asphalt		0.2			T1-A-0.2	795.37	569.84
T5	Asphalt	0.0				T5-A-0.0	798.48	572.95
T2	Asphalt	0.0				T2-A-0.0	820.65	595.13
T4	Asphalt	0.0				T4-A-0.0	837.20	611.67
T3	Asphalt	0.0				T3-A-0.0	838.16	612.63
T1	Asphalt	0.0				T1-A-0.0	838.19	612.66

Figure A7. Absorbed radiation by buildings and ground at 13:00 [W/m^2].

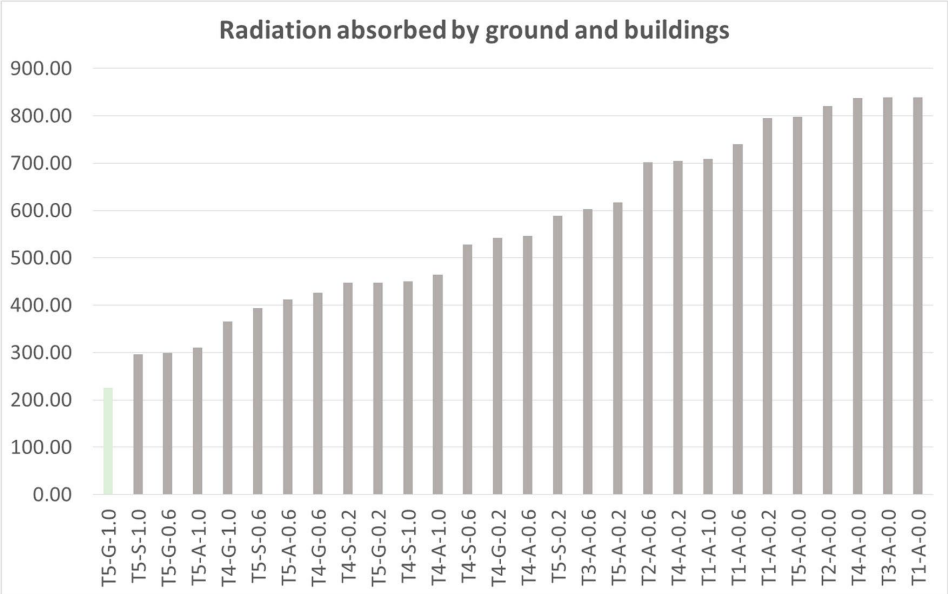

Figure A8. Simulation results ranked in terms of absorption by ground and buildings. The green indicates the scene with trees of LAD = 1 over grass is being used as a base case for comparison.

Appendix Chapter 3. Modelling Mean Radiant Temperature Distribution in Urban Landscapes Using DART

A. Remote Sensing Inputs, Level of Detail and Recommended Scene Settings for Simulation

Table A1. Remote Sensing Inputs, Level of Detail and Recommended Scene Settings for Simulation.

Data source	Scale of study	LOD buildings	LOD vegetation	Scene dimensions	Cell size (x,y)	Cell size (z)	Reference
VHR satellite imagery (WorldView2)	Town	1.1 - 1.2	location, approx. height and volume (cube)	1000 m * 1000 m	2 m - 5 m	1 m or 2 m	ie. Dissegna et al. 2019
	Neighbourhood	1.1 - 1.2		500 m * 500 m	1 m - 2 m	1 m	
Aerial LiDAR Scanning	Town	2	location, accurate height and volume (rounded)	1000 m * 1000 m	2 m - 5 m	1 m or 2 m	ie. Urech et al. 2020
	Neighbourhood	2.1		500 m * 500 m	1 m - 2 m	1 m	
	Building	2.1		<100 m * 100 m	0.5 m - 1 m	0.5 m - 1 m	
3-D Objects of architectural designs	Neighbourhood	2	location, accurate height and volume (rounded)	500 m * 500 m	1 m - 2 m	1 m	Created with any 3-D modelling software
	Building	3.1	n/a	<100 m * 100 m	0.5 m - 1 m	0.5 m - 1 m	
	Tree	n/a	Explicit shape	50 m * 50 m	0.25 m - 0.5 m	0.25 m - 0.5 m	Laubwerk
Hybrid ALS/3-D designs	Town	1.1 - 1.2	location, accurate height and volume (rounded)	1000 m * 1000 m	2 m - 5 m	1 m or 2 m	ie. Urech et al. 2020
	Neighbourhood	up to 1.3		500 m * 500 m	1 m - 2 m	1 m	
	Building	up to 3.2		<100 m * 100 m	0.5 m - 1 m	0.5 m - 1 m	

Remarks: regardless on the source, the different surface materials have to be grouped in order to be linked to their respective spectral properties found within the DART database. For more information on LOD visit: https://osmbuildings.org/blog/2018-02-28_level_of_detail/

Table A2. Estimated Computation Times for One Time-Step Simulations.

Scale	Scene dimensions (m)	cell size (m)	Shortwave (DART)	Longwave (DART)	Tmrt calculation (Python code)	Total
Tree	30 x 30 x 20	0.5 (x,y,z)	9'	100'	2'	111'
Building	100 x 100 x 20	1 (x,y,z)	12'	138'	3'	153'
Neighbourhood	1000 x 1000 x 30	2 (x,y) 1 (z)	450'	5175'	112'	5737'

*PC characteristics: 128 GB RAM, CPU Intel® Xeon® E5-1650 v3 @ 3.50GHz. 6 Cores, 12 Logical processors.

Table A3. Characteristics of Remote Sensing Inputs.

Remote sensing products	Provider	Characteristics	Reference
WorldView2 imagery	Digital Globe	Ten high-resolution WorldView2 images (8-band, 2 m pixel size). Used to derive land cover map.	Dissegna et al. 2019
Building footprint data	Openstreetmap		
Digital surface model (DSM)	AW3D	Derived from photogrammetric reconstruction of Digital Globe stereo satellite images. Nominal resolution of the DSM dataset is 1m for the urban areas and 5m for the densely vegetated area. Used to derive a digital terrain model (DTM), buildings and vegetation heights.	
2014 Aerial LiDAR of Singapore	Singapore Land Authority	Obtained using the Optech Pegasus HA500 sensor with a planar density of 30 points/m².	Urech et al. 2020
Terrestrial LiDAR Scanning (TLS)	SEC/SMART field campaign	Field measurements of leaf area density derived from TLS point cloud collected using Leica P40 sensor.	Wei et al. 2020

B. DART Parameters for Longwave Simulations.

Table A4. DART Parameters for Longwave Simulations.

Flux-tracking			
		Radiation-Radiative method	*Flux Tracking*
		Atmosphere radiative transfer TOA<->BOA	*Radiative transfer simulation*
Flux tracking parameters			*Sparse voxel acceleration: NO*
Products			*Radiation budget products only*
Spectral interval	Spectral band	Longwave	*Central Wavelength 25, Bandwidth 50*
Products			
	Radiative Budget	…	*3D INTR, ABS, SCAR*
		Radiative budget unit	*W/m2*
		Radiative budget components	*Irradiance - Six directions*
		Scene element components	
Direction input parameters			
		Sun angles or date	*Exact date*
		Year	*20xx*
		Month	*xx*
		Day	*xx*
		Hours	**To be set in sequence launcher tool*
		Local time	*yes*
		Time Zone (UTC)	*8 (For Singapore)*
Optical and temperatures properties			
Lambertian	Building walls	Property name	*Building walls*
		2D lambertian database	*Lambertian_mineral.db*
		2D lambertian model	*Sand white*
Lambertian	Glass	Property name	*Glass*
		2D lambertian database	*Lambertian_mineral.db*
		2D lambertian model	*glass_window*
Lambertian	Aluminium Roof	Property name	*Aluminium roof*
		2D lambertian database	*Lambertian_mineral.db*
		2D lambertian model	*aluminium_window*
Lambertian	Badminton Court	Property name	*Badminton Court*
		2D lambertian database	*Lambertian_mineral.db*
		2D lambertian model	*concrete_brown*
Lambertian	Stem	Property name	*Stem*
		2D lambertian database	*Lambertian_mineral.db*
		2D lambertian model	*Bark_deciduous*
Lambertian	Grass	Property name	*Grass*
		2D lambertian database	*Lambertian_mineral.db*
		2D lambertian model	*Grass_rye*
Vegetation	Tree leaf	Vegetation property name	*Tree leaf*
		3D vegetation database	*Lambertian_Vegetation.bd*
		3D vegetation model	*leaf_deciduous*
Temperature	Thermal function	Temperature (Mean and Delta)	*Hourly mean and deltas obtained from energy balance model for each scene component (Appendix C1).*

Atmosphere			
		Gas optical properties	*Tropical*
		Gas temperature profile	*Tropical*
		Gas O3 and other gases vertical profile	*Tropical*
		Redefine temperature profile	✓
		Altitude	*1.5m*
		Temperature [K]	*Specific temperature at each time step (Appendix C1)*
Aerosol	Aerosol properties	Aerosol optical properties	*Tropical_urbav5*
		Aerosol vertical profile	*Urbanv5*
		Aerosol Henyey Greenstein parameters	*Urbanv5*

Table A5. DART Parameters for Shortwave Simulations.

Flux-tracking			
		Radiation-Radiative method	*Flux Tracking*
		Atmosphere radiative transfer TOA<->BOA	*Analytic model*
Flux -tracking parameters			*Sparse voxel acceleration: NO*
Products			*Radiation budget products only*
Spectral interval	Spectral band	Shortwave	*Central Wavelength 1.4, Bandwidth 2.2*
Products			
	Radiative Budget	…	*3D INTR,ABS, SCAR*
		Radiative budget unit	*W/m2*
		Radiative budget components	*Irradiance - Six directions*
		Scene element components	
Direction input parameters			
		Sun angles or date	*Exact date*
		Year	*20xx*
		Month	*xx*
		Day	*xx*
		Hours	**To be set in sequence launcher tool*
		Local time	*yes*
		Time Zone (UTC)	*8 (For Singapore)*
Optical and temperatures properties			
Lambertian	Building walls	Property name	*Building walls*
		2D lambertian database	*Lambertian_mineral.db*
		2D lambertian model	*Sand white*
Lambertian	Glass	Property name	*Glass*
		2D lambertian database	*Lambertian_mineral.db*
		2D lambertian model	*glass_window*
Lambertian	Aluminium Roof	Property name	*Aluminium roof*
		2D lambertian database	*Lambertian_mineral.db*
		2D lambertian model	*aluminium_window*
Lambertian	Badminton Court	Property name	*Badminton Court*
		2D lambertian database	*Lambertian_mineral.db*
		2D lambertian model	*concrete_brown*
Lambertian	Stem	Property name	*Stem*
		2D lambertian database	*Lambertian_mineral.db*
		2D lambertian model	*Bark_deciduous*
Lambertian	Grass	Property name	*Grass*
		2D lambertian database	*Lambertian_mineral.db*
		2D lambertian model	*Grass_rye*
Vegetation	Tree leaf	Vegetation property name	*Tree leaf*
		3D vegetation database	*Lambertian_Vegetation.bd*
		3D vegetation model	*leaf_deciduous*
Temperature		Mean temperature	

	Thermal function	Delta temperature	*Hourly mean and deltas obtained from energy balance model for each scene component (Appendix C1).*
Atmosphere			
		Gas optical properties	*Tropical*
		Gas temperature profile	*Tropical*
		Gas O3 and other gases vertical profile	*Tropical*
Aerosol	Aerosol properties	Aerosol optical properties	*Tropical_urbav5*
		Aerosol vertical profile	*Urbanv5*
		Aerosol Henyey Greenstein parameters	*Urbanv5*
		AOD multiplicative factor	*Retrieved from Aeronet for each time step of the simulation date (Appendix C2).*

C. DART Parameters for Longwave Simulations.

Table A6. DART Parameters for Longwave Simulations.

	Longwave Sequence Parameters												
	Sequence name	seq_0	seq_1	seq_2	seq_3	seq_4	seq_5	seq_6	seq_7	seq_8	seq_9	seq_10	seq_11	seq_12
	Time	7:00	8:00	9:00	10:00	11:00	12:00	13:00	14:00	15:00	16:00	17:00	18:00	19:00
	Badminton court	299.15	300.65	304.65	309.15	314.15	314.15	315.15	318.15	316.65	313.15	312.15	310.65	307.65
	Delta	0	1	7	14	20	20	22	26	25	18	16	15	11
Surface temperatures (K)	Glass windows	299.15	301.15	303.65	306.15	309.15	307.65	307.15	308.15	308.65	309.65	308.65	306.15	303.15
	Delta	0	2	5	8	12	7	4	6	9	11	9	6	0
	Walls	299.15	300.65	302.15	308.15	313.15	312.65	311.15	316.15	316.65	312.65	311.65	310.15	307.65
	Delta	0	1	2	12	18	17	14	22	25	17	15	14	11
	Aluminum roof	299.15	300.65	302.15	303.65	306.15	308.65	311.65	312.15	311.15	310.15	308.15	305.65	302.65
	Delta	0	1	2	3	6	9	13	14	14	12	8	5	1
	Grass	299.15	301.15	304.15	305.15	306.15	307.15	308.15	307.15	307.15	306.15	305.15	304.15	302.15
	Delta	0	2	6	6	6	6	6	6	6	6	4	2	0
	Leaves	299.15	301.15	304.15	305.15	306.15	307.15	308.15	307.15	307.15	306.15	305.15	304.15	302.15
	Delta	0	2	6	6	6	6	6	6	6	6	4	2	0
	Trunk	299.15	301.15	303.15	304.15	306.15	305.15	304.15	304.15	305.15	306.15	305.15	304.15	302.15
	Delta	0	2	4	4	6	4	2	2	4	6	4	2	0
	Air temperature * (K)	299.51	300.06	301.01	301.48	303.5	303.75	304.55	306.28	305.31	305.08	304.58	304.25	303.15

* Measured from a Vaisala weather station mounted next to radiometers.

Table A7. DART Parameters for Shortwave Simulations.

Shortwave Sequence Parameters													
Sequence name	seq_0	seq_1	seq_2	seq_3	seq_4	seq_5	seq_6	seq_7	seq_8	seq_9	seq_10	seq_11	seq_12
Time	7:00	8:00	9:00	10:00	11:00	12:00	13:00	14:00	15:00	16:00	17:00	18:00	19:00
AOD multiplicative factor *	0.171	0.172	0.185	0.192	0.361	0.422	0.337	0.340	0.297	0.211	0.214	0.158	0.185

* Obtained from NASA AERONET for Singapore for simulation date 29.02.2020.

D. Spectral Signatures of Construction Materials and Vegetation

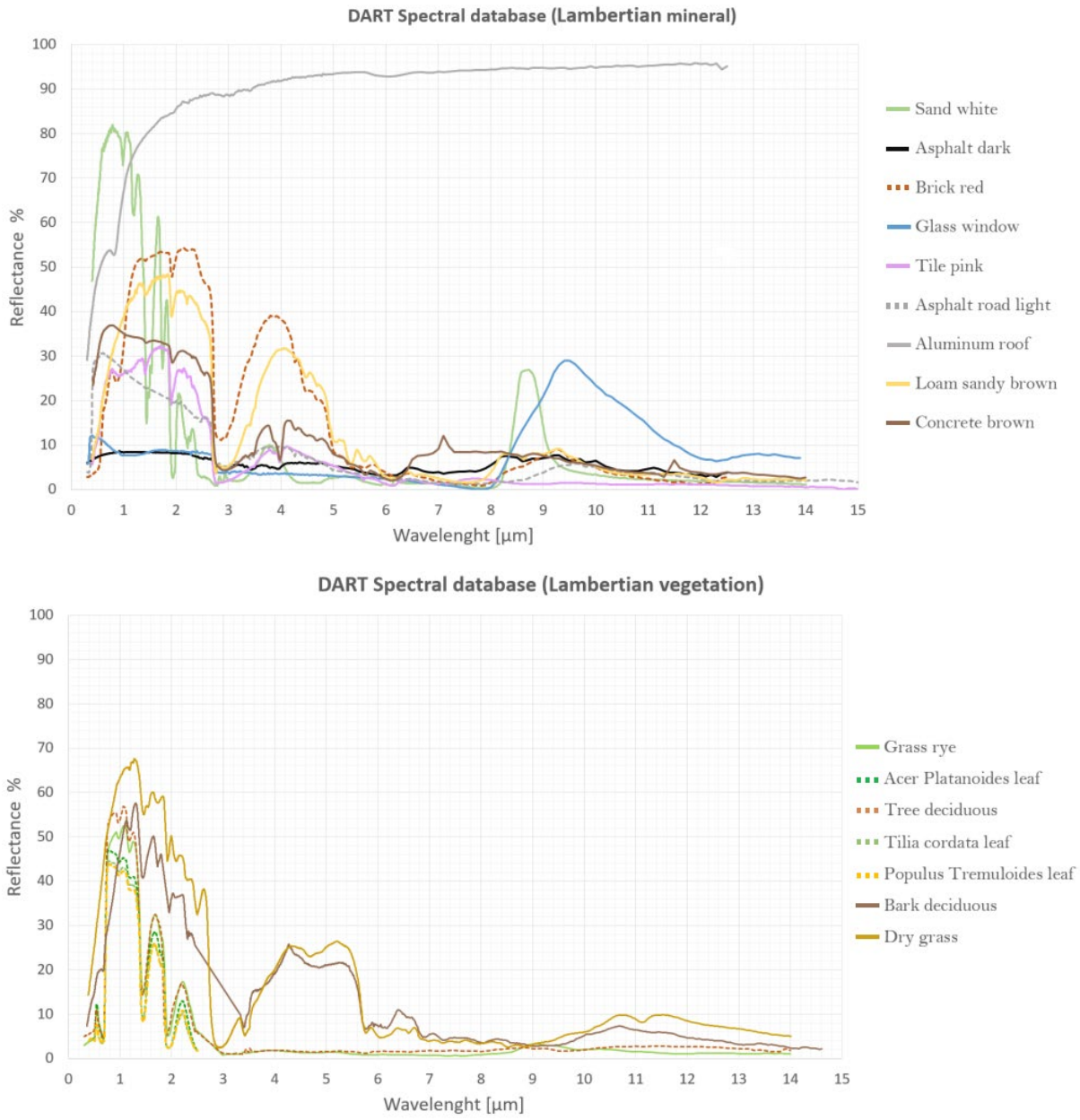

Figure A1. Spectral Signatures of Construction Materials and Vegetation (from DART Database).

E. Sensitivity to Changing LAI

Sensitivity to Changing LAI at 16:00			
LAI	Average Tmrt under canopy [°C]		
	Khaya S.	Albizia S.	Tabebuia R.
0.1	33.15	48.81	49.34
0.5	30.27	44.33	45.89
1.5	28.25	38.05	40.46
3.5	26.84	33.78	34.4
5.5	25.89	30.32	31.7
Tmrt outside canopy shade is 64.1 °C			

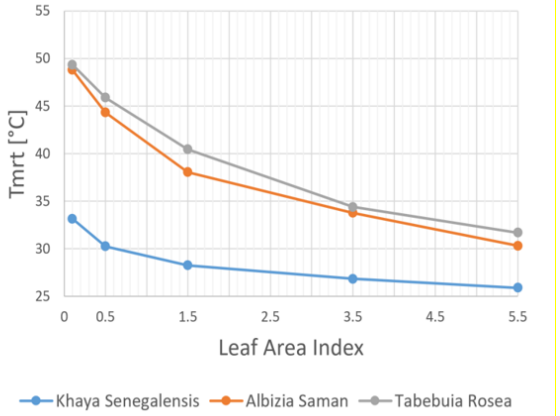

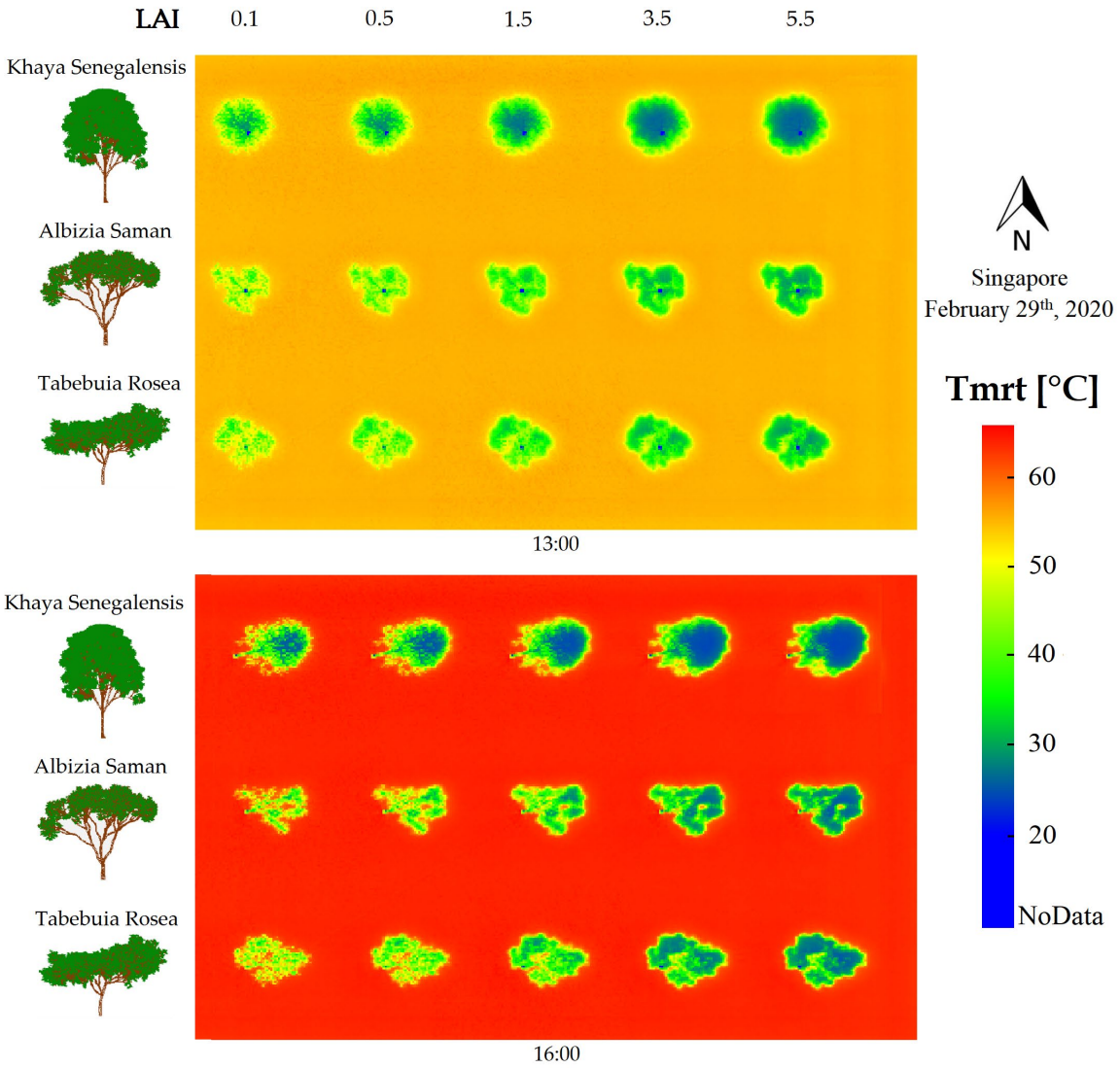

Figure A2. (**a**) Sensitivity to Changing LAI at 16:00 (**b**) Visualization of Tmrt at pedestrian level under different tree species with changing LAI.

F. Sensitivity to Changing Surface Temperatures of Different Ground Material

Table A8. Sensitivity to Changing Surface Temperatures of Different Ground Materials at 16:00.

Sensitivity to Changing Surface Temperatures of Different Ground Materials at 16:00								
80 m × 80 m scene with one building (W:10 m × L:20 m × H:15 m)	Surface temperature concrete building	312.65 K						
	Surface temperature ground	20 °C	25 °C	30 °C	35 °C	40 °C	50 °C	60 °C
	Surface temperature ground (K)	293.15	298.15	303.15	308.15	313.15	323.15	333.15
	Tmrt (°C) Grass	57.53	59.37	61.20	63.08	65.03	*	*
	Tmrt (°C) Concrete	60.01	61.67	63.38	65.16	66.99	70.84	74.91
	Tmrt (°C) Asphalt Light	59.75	61.47	63.24	65.08	66.98	70.95	75.16
	Tmrt (°C) Asphalt Grey	57.29	59.00	60.78	62.62	64.51	68.49	72.69
	Tmrt (°C) Asphalt Dark	52.60	54.51	56.49	58.62	60.73	65.12	69.75

* Omitted Tmrt values since a surface temperature above 40 °C for grass is unrealistic.

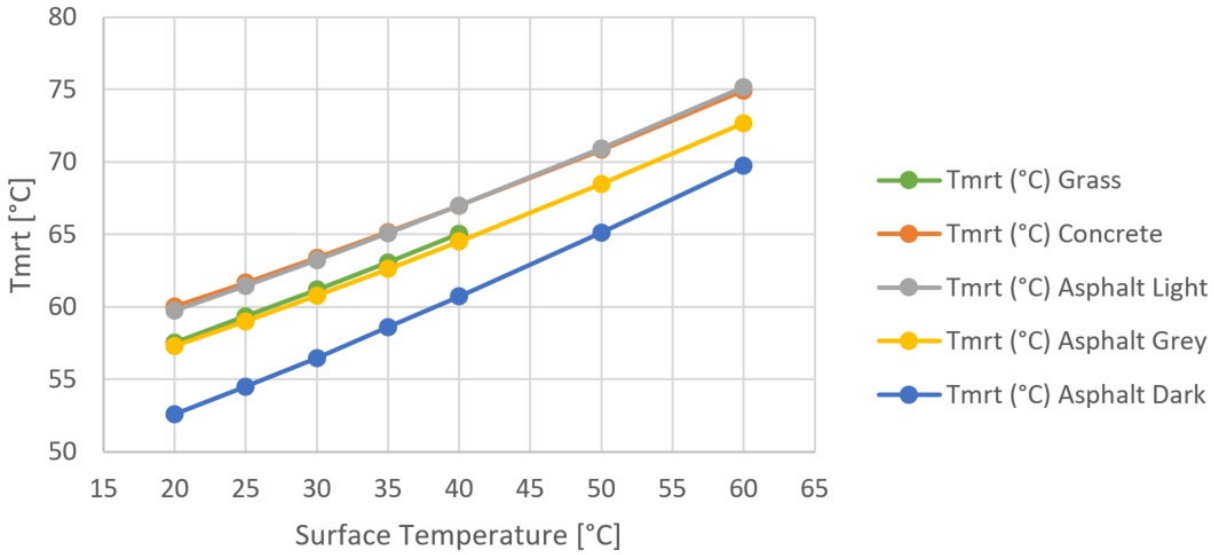

Figure A3. Sensitivity to Changing Surface Temperatures of Different Ground Material.

Appendix G. Sensitivity to Changing Wall Material

Table A9. Sensitivity to Changing Wall Material (16:00).

Sensitivity to Changing Wall Material (16:00)	
Surface temperature ground * (Asphalt road light)	303.15 K Delta: 8
Surface temperature white concrete wall and roof *	303.15 K Delta: 8
Surface temperature glass *	303.15 K Delta: 8
Temperature range	26–34 °C
Tmrt at 0.5 m from sunlit white concrete wall	79.39 °C
Tmrt at 0.5 m from sunlit white concrete—glass wall	68.59 °C
Tmrt at 0.5 m from sunlit glass wall	64.47 °C

* Assumed surface temperature.

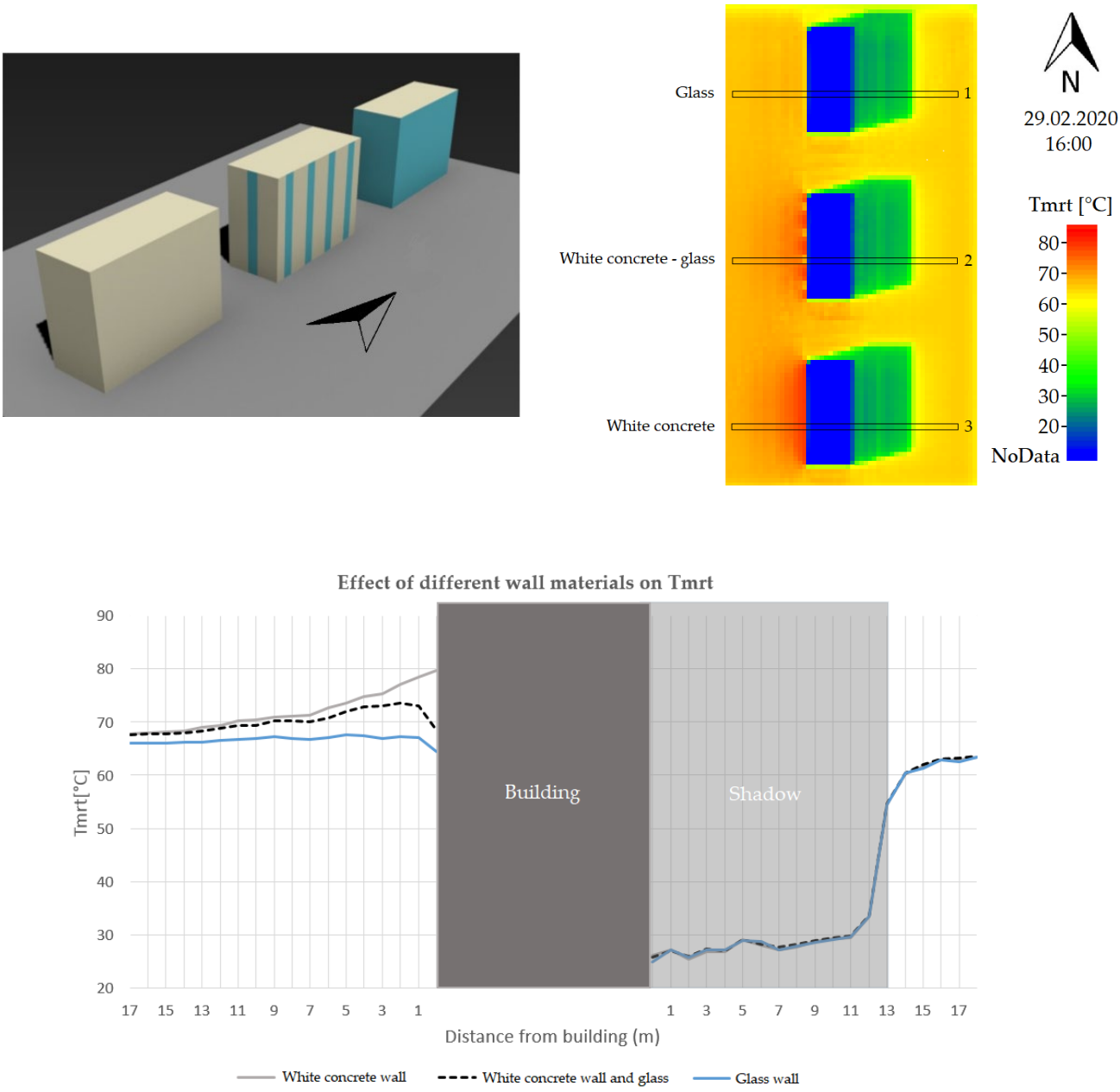

Figure A4. (**a**,**b**) Sensitivity to Changing Wall Material. (**c**) Plot showing the values corresponding to the cells comprised in the black rectangles 1, 2, 3 on each of the three buildings.

Appendix Chapter 4. Automatic delineation of individual tree crowns in a tropical urban park: assessment of a new deep learning algorithm over different spectral and spatial resolutions

A. Summary of results – Delineation accuracy

Left side: The Dice coefficient (DSC) gives a measure of the overlap between predicted tree crowns and ground truth; Recall indicates the fraction of predicted instances matching the ground truth dataset; Precision indicates the fraction of predicted instances that are actual trees in the ground truth.

Right side: Number of overlaps (predicted vs ground truth) and their frequencies. **One-to-one match** (bars in 1): predicted segmentation vs ground truth (blue); ground truth vs predicted segmentation (orange). Number of **false positives:** (blue bar in zero). Number of **false negatives** (orange bar in zero). **Over-segmentation** (blue bars 2- 10)**:** number of predicted crowns overlapping each individual ground truth tree crown. **Under-segmentation** (orange bars 2- 10)**:** number of crowns in the ground truth overlapping with each individual crown in the prediction dataset.

Satellite imagery

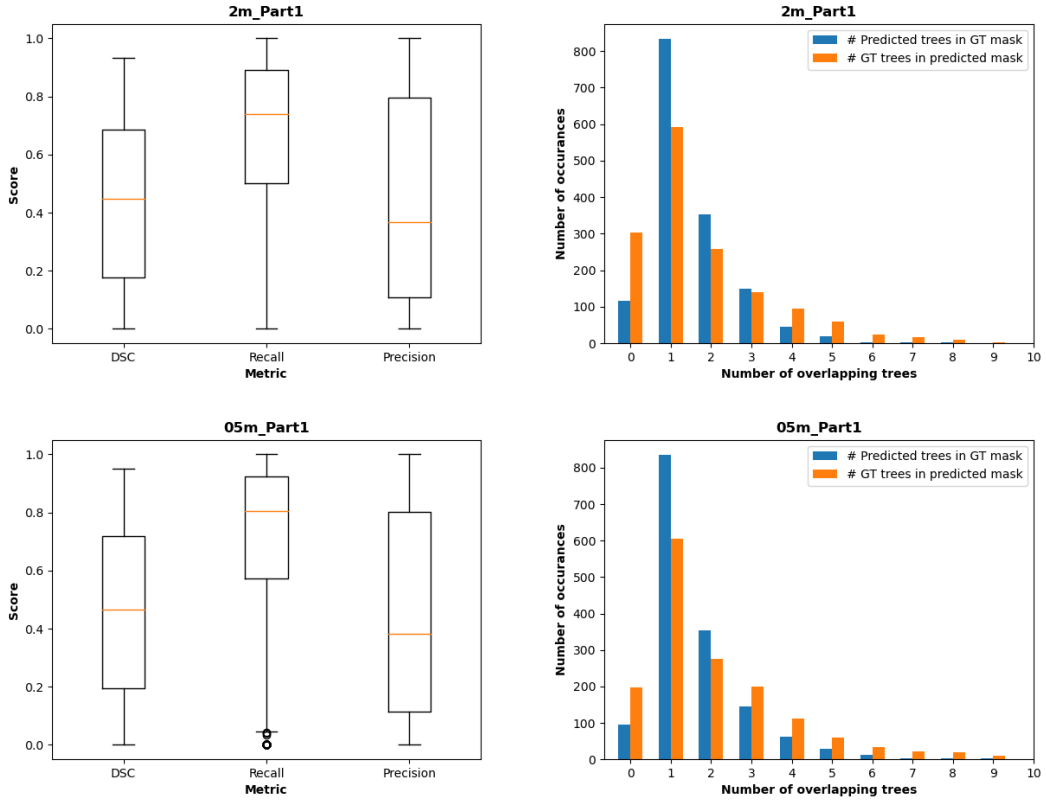

Hyperspectral Imagery

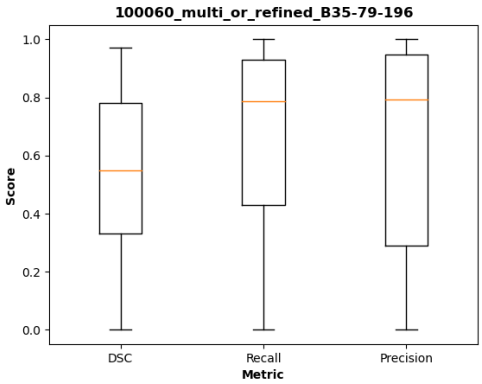

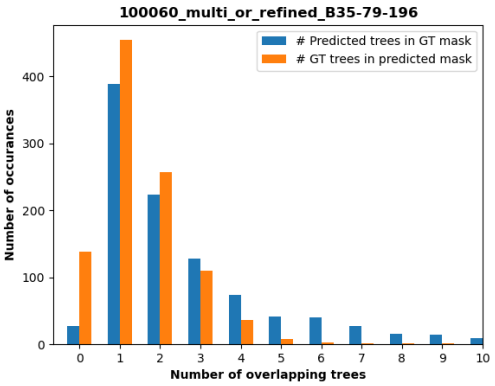

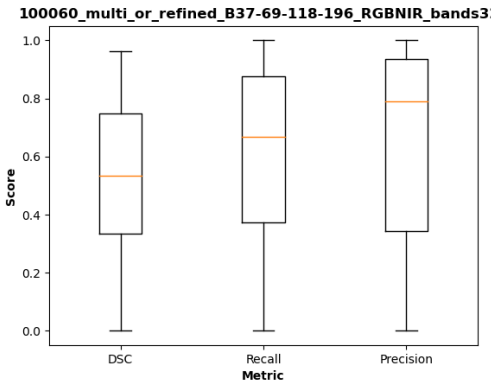

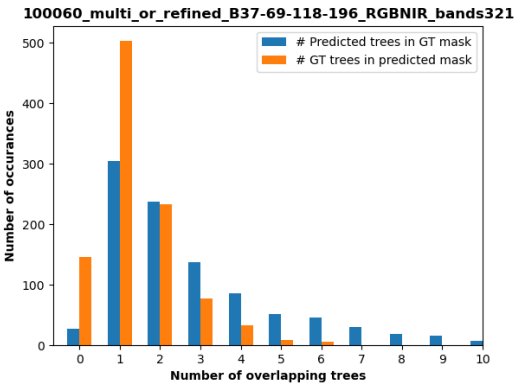

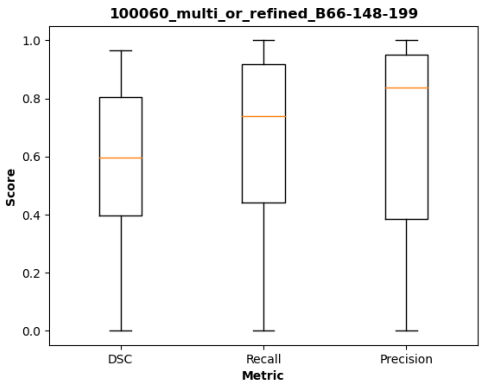

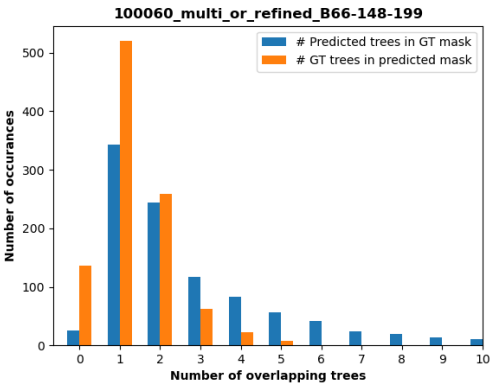

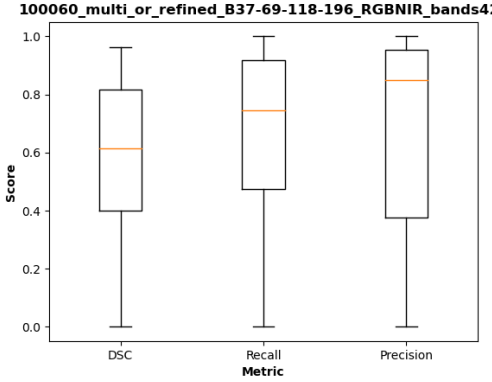
100060_multi_or_refined_B37-69-118-196_RGBNIR_bands421
Score
Metric
DSC
Recall
Precision

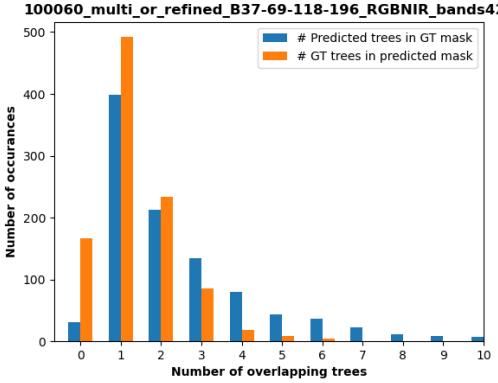
100060_multi_or_refined_B37-69-118-196_RGBNIR_bands421
Predicted trees in GT mask
GT trees in predicted mask
Number of occurances
Number of overlapping trees

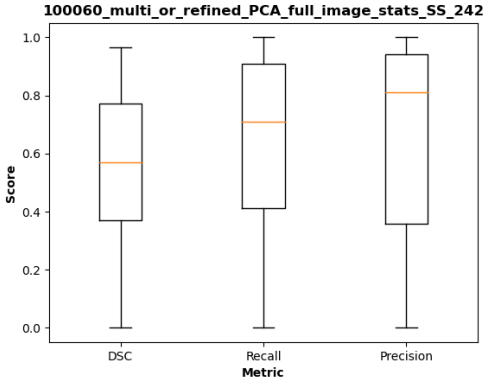
100060_multi_or_refined_PCA_full_image_stats_SS_242
Score
Metric
DSC
Recall
Precision

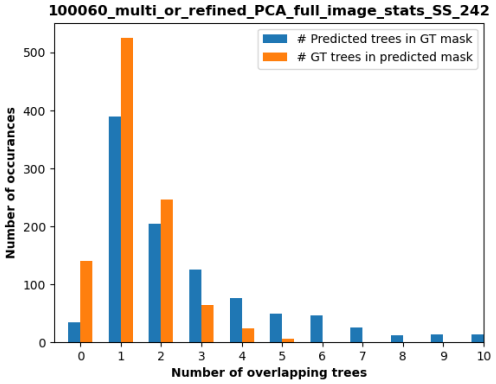
100060_multi_or_refined_PCA_full_image_stats_SS_242
Predicted trees in GT mask
GT trees in predicted mask
Number of occurances
Number of overlapping trees

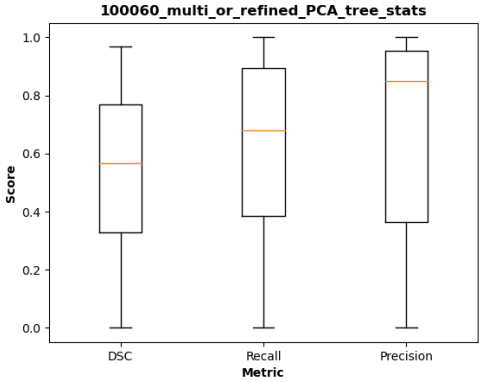
100060_multi_or_refined_PCA_tree_stats
Score
Metric
DSC
Recall
Precision

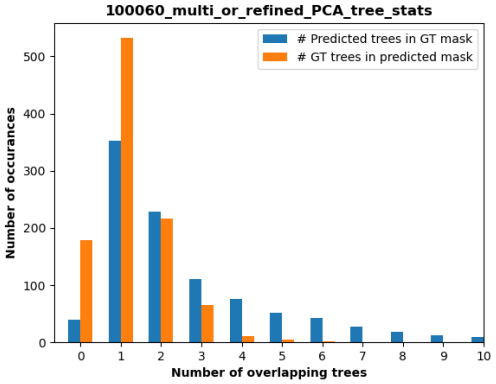
100060_multi_or_refined_PCA_tree_stats
Predicted trees in GT mask
GT trees in predicted mask
Number of occurances
Number of overlapping trees

B. Visualization of results

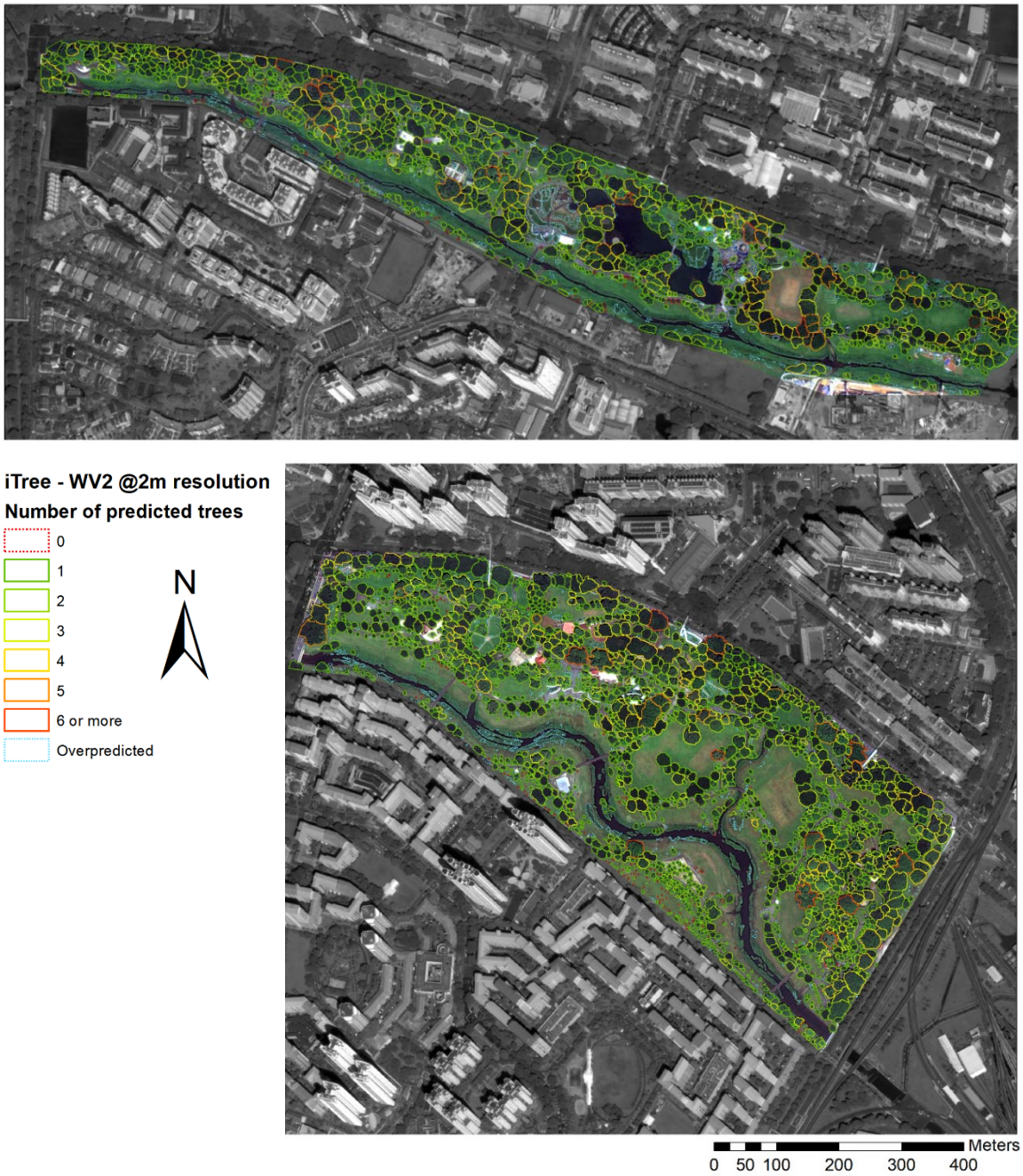

Visualization of the number of predicted trees overlapping each manually delineated crown for WV2 image at 2 m resolution.

C. Visual comparison of delineation outputs

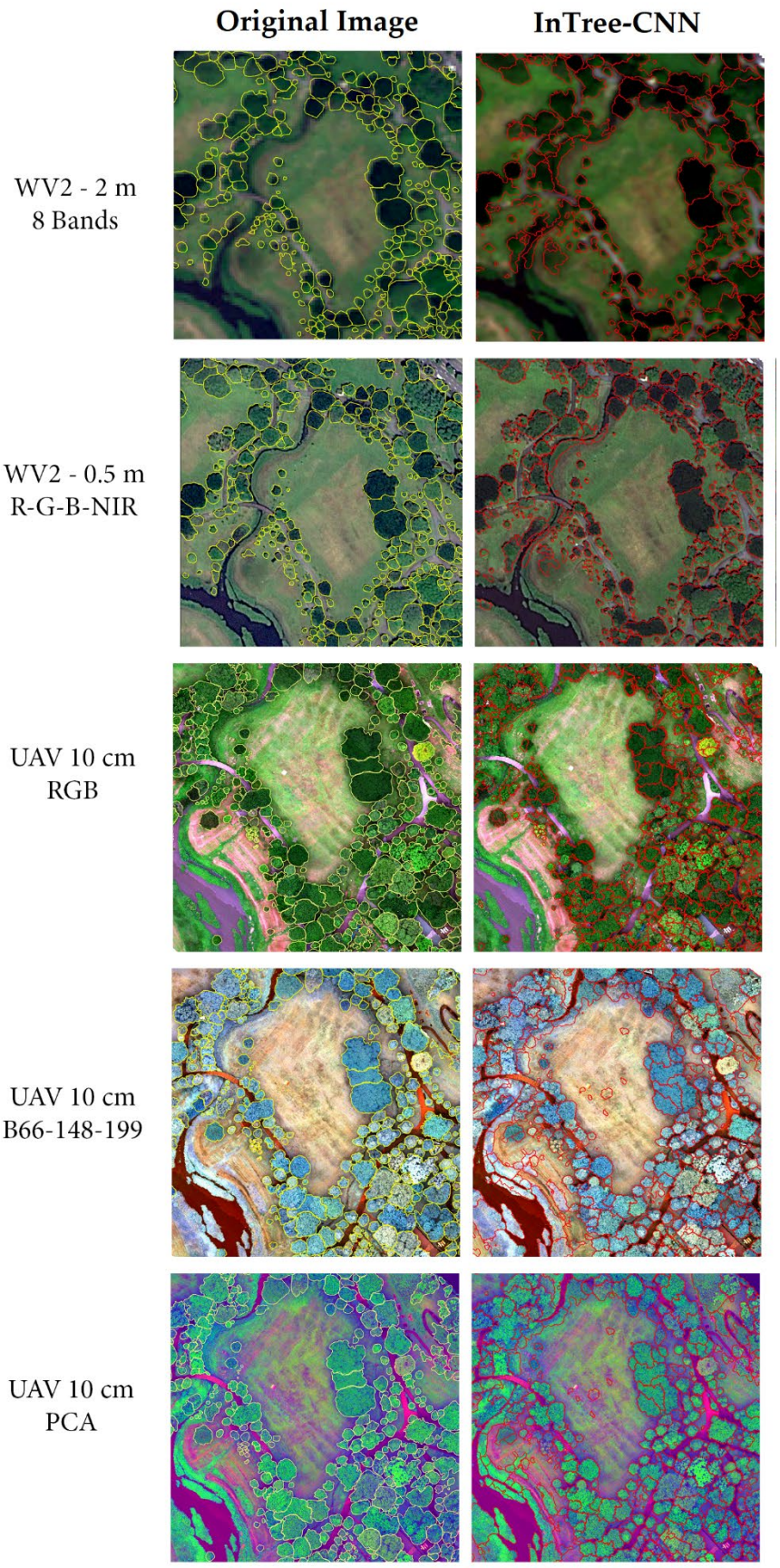

7. References

1. Patz, D. Engelberg, J.L. The effects of changing weather on public health. *Annu. Rev. Public Heal.* **2000**, 271–307.
2. Grimm, N.B.; Faeth, S.H.; Golubiewski, N.E.; Redman, C.L.; Wu, J.; Bai, X.; Briggs, J.M.; Grimm, N.B.; Faeth, S.H.; Golubiewski, N.E.; et al. Global Change and the Ecology of Cities. *Science (80-.).* **2008**, *319*, 756–760.
3. Georgi, J.N.; Dimitriou, D. The contribution of urban green spaces to the improvement of environment in cities: Case study of Chania, Greece. *Build. Environ.* **2010**, *45*, 1401–1414.
4. Akbari, H. Shade trees reduce building energy use and CO2 emissions from power plants. *Environ. Pollut.* **2002**, *116*, 119–126.
5. OKE, T.R. The energetic basis of the urban heat island. *Quart. J. R. Met. Soc.* **1982**, *108*.
6. Nice, K.A.; Coutts, A.M.; Tapper, N.J. Urban Climate Development of the VTUF-3D v1 . 0 urban micro-climate model to support assessment of urban vegetation in fl uences on human thermal comfort. *Urban Clim.* **2018**, 1–25.
7. Myint, S.W.; Brazel, A.; Okin, G.; Buyantuyev, A. Combined Effects of Impervious Surface and Vegetation Cover on Air Temperature Variations in a Rapidly Expanding Desert City. *GIScience Remote Sens.* **2010**, *47*, 301–320.
8. Simpson, J.R. Improved estimates of tree-shade effects on residential energy use. *Energy Build.* **2002**, *34*, 1067–1076.
9. Xiao, Q.; McPherson, E.G.; Ustin, S.L.; Grismer, M.E. A new approach to modeling tree rainfall interception. *J. Geophys. Res.* **2000**, *105*, 29173–29188.
10. McPherson, E.G.; Simpson, J.R.; Xiao, Q.; Wu, C. Million trees Los Angeles canopy cover and benefit assessment. *Landsc. Urban Plan.* **2011**, *99*, 40–50.
11. Singapore, N.P. *One million trees movement - Media Factsheet*; **2020**.
12. Richards, D.; Fung, T. K.; Meili, N.; Song, X. P.; Dissegna, M. A.; Drillet, Z.; Urech, P.R.W.; Edwards, P. An ecosystem service design loop for using vegetation to mitigate the urban heat island effect; **2019**.
13. Urech, P.R.W.; Dissegna, M.A.; Girot, C.; Grêt-Regamey, A. Point cloud modeling as a bridge between landscape design and planning. *Landsc. Urban Plan.* **2020**, *203*, 103903.
14. Meili, N.; Dissegna, M. A.; Urech P.R.W.; Mughal, O.; Richards, D.; Drillet, Z.; Edwards, P. Assessment of Ecosystem Services with New Tools and Data. In *Future Cities Laboratory: Indicia 03*; Lars Müller Publishers, **2020**.
15. Voogt, J.A.; Oke, T.R. Thermal remote sensing of urban climates. **2002**, *86*, 370–384.
16. Aghamolaei, R.; Azizi, M.; Aminzadeh, B. A comprehensive review of outdoor thermal comfort in urban areas : Effective parameters and approaches. **2023**.
17. Semeraro, T.A. Planning of Urban Green Spaces : An Ecological Perspective on Human Benefits. *Land* **2021**, 1–25.
18. Lai, D.; Liu, W.; Gan, T.; Liu, K.; Chen, Q. A review of mitigating strategies to improve the thermal environment and thermal comfort in urban outdoor spaces. *Sci. Total Environ.* **2019**,

661, 337–353.

19. Kondo, K.; Mabon, L.; Bi, Y.; Chen, Y.; Hayabuchi, Y. Balancing conflicting mitigation and adaptation behaviours of urban residents under climate change and the urban heat island effect. *Sustain. Cities Soc.* **2021**, *65*, 102585.

20. Sari, D.P. A Review of How Building Mitigates the Urban Heat Island in Indonesia and Tropical Cities. **2021**, 653–666.

21. Taleghani, M.; Sailor, D.; Ban-Weiss, G.A. Micrometeorological simulations to predict the impacts of heat mitigation strategies on pedestrian thermal comfort in a Los Angeles neighborhood. *Environ. Res. Lett.* **2016**, *11*.

22. Bruse, M. Huttner, S. Numerical modeling of the urban climate - a preview on ENVI-MET 4.0. *seventh Int. Conf. Urban Clim.* **2009**, 1–4.

23. Lindberg, F.; Holmer, B.; Thorsson, S. SOLWEIG 1.0 - Modelling spatial variations of 3D radiant fluxes and mean radiant temperature in complex urban settings. *Int. J. Biometeorol.* **2008**, *52*, 697–713.

24. Dissegna, M.A.; Yin, T.; Wei, S.; Richards, D.; Grêt-Regamey, A. 3-D reconstruction of an urban landscape to assess the influence of vegetation in the radiative budget. *Forests* **2019**, *10*, 1–19.

25. Gastellu-Etchegorry, J. Modeling Radiative Transfer in Heterogeneous 3-D Vegetation Canopies. *Remote Sens. Environ.* **1996**, *58*, 131–156.

26. Gastellu-Etchegorry, J. Discrete Anisotropic Radiative Transfer (DART 5) for Modeling Airborne and Satellite Spectroradiometer and LIDAR Acquisitions of Natural and Urban Landscapes. *Remote Sens.* **2015**, 1667–1701.

27. Gastellu-Etchegorry, J.P.; Lauret, N.; Yin, T.; Landier, L.; Kallel, A.; Malenovský, Z.; Al Bitar, A.; Aval, J.; Benhmida, S.; Qi, J.; et al. DART: Recent advances in remote sensing data modeling with atmosphere, polarization, and chlorophyll fluorescence. *IEEE J. Sel. Top. Appl. Earth Obs. Remote Sens.* **2017**, *10*, 2640–2649.

28. Widlowski, J.; Pinty, B.; Lopatka, M.; Atzberger, C.; Buzica, D.; Chelle, M.; Disney, M.; Gerboles, M.; Gobron, N.; Grau, E.; et al. The fourth radiation transfer model intercomparison (RAMI-IV): Proficiency testing of canopy reflectance models with ISO-13528. *J. Geophys. Res. Atmos* **2013**, *118*, 6869–6890.

29. Asner, G.P.; Townsend, P.A.; Martin, R.E.; Chadwick, K.D. Forest Biophysical and Biochemical Properties from Hyperspectral and LiDAR Remote Sensing. **2015**, 429–448.

30. Aasen, H. State-of-the-art in UAV remote sensing survey - First insights into applications of UAV sensing systems. *Int. Arch. Photogramm. Remote Sens. Spat. Inf. Sci. - ISPRS Arch.* **2017**, *42*, 1–4.

31. Smigaj, M.; Gaulton, R.; Barr, S.L.; Suárez, J.C. Uav-Borne Thermal Imaging for Forest Health Monitoring: Detection of Disease-Induced Canopy Temperature Increase. *ISPRS - Int. Arch. Photogramm. Remote Sens. Spat. Inf. Sci.* **2015**, *XL-3/W3*, 349–354.

32. Nolan, A.P.; Connell, M.G.O. Estimation of crop water stress in a nectarine orchard using high-resolution imagery from unmanned aerial vehicle (UAV). **2015**, 1413–1419.

33. Zarco-Tejada, P.J.; González-Dugo, V.; Berni, J.A.J. Fluorescence, temperature and narrow-band indices acquired from a UAV platform for water stress detection using a micro-hyperspectral imager and a thermal camera. *Remote Sens. Environ.* **2012**, *117*, 322–337.

34. Primicerio, J.; Di Gennaro, S.F.; Fiorillo, E.; Genesio, L.; Lugato, E.; Matese, A.; Vaccari, F.P. A flexible unmanned aerial vehicle for precision agriculture. *Precis. Agric.* **2012**, *13*, 517–523.

35. Honkavaara, E.; Kaivosoja, J.; Mäkynen, J.; Pellikka, I.; Pesonen, L.; Saari, H.; Salo, H.; Hakala, T.; Marklelin, L.; Rosnell, T. Hyperspectral Reflectance Signatures and Point Clouds for Precision Agriculture By Light Weight Uav Imaging System. *ISPRS Ann. Photogramm. Remote Sens. Spat. Inf. Sci.* **2012**, *I–7*, 353–358.

36. Mäkynen, J.; Saari, H.; Holmlund, C.; Mannila, R.; Antila, T. Multi- and hyperspectral UAV imaging system for forest and agriculture applications. **2012**, *8374*, 837409.

37. Merino, L.; Caballero, F.; Martínez-De-Dios, J.R.; Maza, I.; Ollero, A. An unmanned aircraft system for automatic forest fire monitoring and measurement. *J. Intell. Robot. Syst. Theory Appl.* **2012**, *65*, 533–548.

38. Nevalainen, O.; Honkavaara, E.; Tuominen, S.; Viljanen, N.; Hakala, T.; Yu, X.; Hyyppä, J.; Saari, H.; Pölönen, I.; Imai, N.N.; et al. Individual tree detection and classification with UAV-Based photogrammetric point clouds and hyperspectral imaging. *Remote Sens.* **2017**, *9*.

39. Cao, J.; Leng, W.; Liu, K.; Liu, L.; He, Z.; Zhu, Y. Object-Based Mangrove Species Classification Using Unmanned Aerial Vehicle Hyperspectral Images and Digital Surface Models. *Remote Sens.* **2018**, *10*, 89.

40. Wang, J.; Chen, X.; Cao, L.; An, F.; Chen, B.; Xue, L.; Yun, T. Individual rubber tree segmentation based on ground-based LiDAR data and faster R-CNN of deep learning. *Forests* **2019**, *10*, 1–20.

41. Horcher, A.; Visser, R.J.M. Unmanned Aerial Vehicles: Applications for Natural Resource Management and Monitoring. *Mach. People, Interface* **2004**, 5.

42. Wei, S.; Yin, T.; Dissegna, M.A.; Whittle, A.J.; Ow, G.L.F.; Yusof, M.L.M.; Lauret, N.; Gastellu-Etchegorry, J.P. An assessment study of three indirect methods for estimating leaf area density and leaf area index of individual trees. *Agric. For. Meteorol.* **2020**, *292–293*, 108101.

43. Grau, E.; Durrieu, S.; Fournier, R.; Gastellu-etchegorry, J.; Yin, T. Estimation of 3D vegetation density with Terrestrial Laser Scanning data using voxels . A sensitivity analysis of influencing parameters. *Remote Sens. Environ.* **2017**, *191*, 373–388.

44. Bournez, E.; Landes, T.; Saudreau, M.; Kastendeuch, P.; Najjar, G. From TLS point clouds to 3D models of trees: A comparison of existing algorithms for 3D tree reconstruction. *Int. Arch. Photogramm. Remote Sens. Spat. Inf. Sci. - ISPRS Arch.* **2017**, *42*, 113–120.

45. Béland, M.; Widlowski, J.L.; Fournier, R.A.; Côté, J.F.; Verstraete, M.M. Estimating leaf area distribution in savanna trees from terrestrial LiDAR measurements. *Agric. For. Meteorol.* **2011**, *151*, 1252–1266.

46. Béland, M.; Widlowski, J.; Fournier, R.A.; Verstraete, M.M. Estimating leaf area distribution in savanna trees from terrestrial LiDAR measurements. *Agric. For. Meteorol.* **2011**, *151*, 1252–1266.

47. Asner, G.P.; Clark, J.K.; Mascaro, J.; Galindo García, G.A.; Chadwick, K.D.; Navarrete Encinales, D.A.; Paez-Acosta, G.; Cabrera Montenegro, E.; Kennedy-Bowdoin, T.; Duque, Á.; et al. High-resolution mapping of forest carbon stocks in the Colombian Amazon. *Biogeosciences* **2012**, *9*, 2683–2696.

48. van Leeuwen, M.; Nieuwenhuis, M. Retrieval of forest structural parameters using LiDAR remote sensing. *Eur. J. For. Res.* **2010**, *129*, 749–770.

49. Kong, F.; Yan, W.; Zheng, G.; Yin, H.; Cavan, G.; Zhan, W. Agricultural and Forest Meteorology Retrieval of three-dimensional tree canopy and shade using terrestrial laser scanning (TLS) data to analyze the cooling effect of vegetation. *Agric. For. Meteorol.* **2016**, *217*, 22–34.

50. Berger, K.; Pablo, J.; Caicedo, R.; Martino, L.; Wocher, M.; Hank, T. A Survey of Active Learning for Quantifying Vegetation Traits from Terrestrial Earth Observation Data. **2021**, 1–23.

51. Verrelst, J.; Malenovský, Z.; Van der Tol, C.; Camps-Valls, G.; Gastellu-Etchegorry, J.P.; Lewis, P.; North, P.; Moreno, J. Quantifying Vegetation Biophysical Variables from Imaging Spectroscopy Data: A Review on Retrieval Methods. *Surv. Geophys.* **2019**, *40*, 589–629.

52. Meili, N.; Acero, J.A.; Peleg, N.; Manoli, G.; Burlando, P.; Fatichi, S. Vegetation cover and plant-trait effects on outdoor thermal comfort in a tropical city. *Build. Environ.* **2021**, *195*.

53. Li, Y.; Song, Y. Optimization of vegetation arrangement to improve microclimate and thermal comfort in an urban park. *Int. Rev. Spat. Plan. Sustain. Dev.* **2019**, *7*, 18–30.

54. Park, C.Y.; Lee, D.K.; Krayenhoff, E.S.; Heo, H.K.; Hyun, J.H.; Oh, K.; Park, T.Y. Variations in pedestrian mean radiant temperature based on the spacing and size of street trees. *Sustain. Cities Soc.* **2019**, *48*, 1–9.

55. Abdollahzadeh, N.; Biloria, N. Outdoor thermal comfort: Analyzing the impact of urban configurations on the thermal performance of street canyons in the humid subtropical climate of Sydney. *Front. Archit. Res.* **2021**, *10*, 394–409.

56. Lindberg, F.; Onomura, S.; Grimmond, C.S.B. Influence of ground surface characteristics on the mean radiant temperature in urban areas. *Int. J. Biometeorol.* **2016**, *60*, 1439–1452.

57. Zhen, Z.; Benromdhane, N.; Kallel, A.; Wang, Y.; Regaieg, O.; Boitard, P.; Landier, L.; Chavanon, E.; Lauret, N.; Guilleux, J.; et al. DART: a 3D radiative transfer model for urban studies. *2023 Jt. Urban Remote Sens. Event, JURSE 2023* **2023**, 3–6.

58. Sievers, O. CNN-based Methods for Tree Species Detection in UAV images. **2022**.

59. Singapore: Subdivision (Planning Areas and Subzones) - Population Statistics, Charts and Map. **2020**, 100990.

60. Roth, M.; Jansson, C.; Velasco, E. Multi-year energy balance and carbon dioxide fluxes over a residential neighbourhood in a tropical city. *Int. J. Climatol.* **2017**, *37*, 2679–2698.

61. Dhanabalan, S.; *Speech by S Dhanabalan, Minister for National Development at the opening of the park network system, Kallang river Phase I*; **1992**.

62. Mukrimaa, S.S.; Fahyuni, E.F.; Yulia Citra, A.; Schulz, N.D.; Taniredja, T.; Faridli, E.M.; Harmianto, S. Bringing Kallang River into Bishan Park. *J. Penelit. Pendidik. Guru Sekol. Dasar* **2016**, *6*, 128.

63. Landier, L.; Gastellu-Etchegorry, J.P.; Al Bitar, A.; Chavanon, E.; Lauret, N.; Feigenwinter, C.; Mitraka, Z.; Chrysoulakis, N. Calibration of urban canopies albedo and 3D shortwave radiative budget using remote-sensing data and the DART model. *Eur. J. Remote Sens.* **2018**, *51*, 739–753.

64. Gros, A.; Bozonnet, E.; Inard, C. Modelling the radiative exchanges in urban areas: A review. *Adv. Build. Energy Res.* **2011**, *5*, 163–206.

65. Govaerts, Y.M.; Verstraete, M.M. Raytran: A Monte Carlo ray-tracing model to compute light

scattering in three-dimensional heterogeneous media. *IEEE Trans. Geosci. Remote Sens.* **1998**, *36*, 493–505.

66. Disney, M.I.; Lewis, P.E.; Bouvet, M.; Prieto-Blanco, A.; Hancock, S. Quantifying surface reflectivity for spaceborne lidar via two independent methods. *IEEE Trans. Geosci. Remote Sens.* **2009**, *47*, 3262–3271.

67. Kobayashi, H.; Iwabuchi, H. A coupled 1-D atmosphere and 3-D canopy radiative transfer model for canopy reflectance, light environment, and photosynthesis simulation in a heterogeneous landscape. *Remote Sens. Environ.* **2008**, *112*, 173–185.

68. Govaerts, Y.; Verstraete, M.M. Modeling the scattering of light in three-dimensional canopies: contribution of a Monte Carlo ray tracing approach. *Conf. Proc. Second Top. Symp. Comb. Opt. Earth Atmos. Sens.* **1995**, 31–34.

69. Widlowski, J.L.; Taberner, M.; Pinty, B.; Bruniquel-Pinel, V.; Disney, M.; Fernandes, R.; Gastellu-Etchegorry, J.P.; Gobron, N.; Kuusk, A.; Lavergne, T.; et al. Third Radiation Transfer Model Intercomparison (RAMI) exercise: Documenting progress in canopy reflectance models. *J. Geophys. Res. Atmos.* **2007**, *112*, 1–28.

70. Widlowski, J.; Mio, C.; Disney, M.; Adams, J.; Andredakis, I.; Atzberger, C.; Brennan, J.; Busetto, L.; Chelle, M.; Ceccherini, G.; et al. The fourth phase of the radiative transfer model intercomparison (RAMI) exercise : Actual canopy scenarios and conformity testing. **2015**, *169*, 418–437.

71. Li, X.; Koh, T.; Panda, J.; Norford, L.K. Impact of urbanization patterns on the local climate of a tropical city , Singapore : An ensemble study. *J. Geophys. Res.Atmos.* **2016**, 4386–4403.

72. Chow, W.T.L.; Roth, M. Temporal dynamcs of the urban heat island of Singapore. *Int. J. Clim.* **2006**, *2260*, 2243–2260.

73. Updike, T. and C.C. Radiometric Use of WorldView-2 Imagery Technical Note. *DigitalGlobe* **2010**, 1–17.

74. Visual Information Solutions, I. FLAASH Module User's Guide. **2006**.

75. ITT Visual Information Solutions *Workflow Tools in ENVI Whitepaper*.

76. Vosselman, G. Slope based filtering of laser altimetry data. *Int. Arch. Photogramm. Remote Sens. Spat. Inf. Sci.* **2000**, *XXXIII/3*, 935–942.

77. Lee, S.; Wolberg, G.; Shin, S.Y. Scattered data interpolation with multilevel b-splines. *IEEE Trans. Vis. Comput. Graph.* **1997**, *3*, 228–244.

78. Béland, M.; Widlowski, J.L.; Fournier, R.A. A model for deriving voxel-level tree leaf area density estimates from ground-based LiDAR. *Environ. Model. Softw.* **2014**, *51*, 184–189.

79. Liang, S.; Li, X.; Wang, J. Chapter 12 - Fraction of Absorbed Photosynthetically Active Radiation by Green Vegetation. In *Advanced Remote Sensing*; **2012**.

80. Yuan, C.; Shan, R.; Zhang, Y.; Li, X.X.; Yin, T.; Hang, J.; Norford, L. Multilayer urban canopy modelling and mapping for traffic pollutant dispersion at high density urban areas. *Sci. Total Environ.* **2019**, *647*, 255–267.

81. Mughal, M.O.; Li, X.; Yin, T.; Martilli, A.; Brousse, O.; Dissegna, M.A.; Norford, L.K. High-resolution, multi-layer modelling of Singapore's urban climate incorporating local climate zones. *J. Geophys. Res. Atmos.* **2019**.

82. Fanger, P.O. Thermal comfort. In *Danish Technical Press.*; **1970**.

83. Thorsson, S.; Rocklöv, J.; Konarska, J.; Lindberg, F.; Holmer, B.; Dousset, B.; Rayner, D. Mean radiant temperature - A predictor of heat related mortality. *Urban Clim.* **2014**, *10*, 332–345.

84. Höppe, P. The physiological equivalent temperature – a universal index for the biometeorological assessment of the thermal environment. **1999**, *2466*, 71–75.

85. Jendritzky, G. De Dear, R. Havenith, G. Institutional Repository UTCI - why another thermal index ? *Int. J. Biometeorol.* **2012**, *56*, 421–428.

86. Staiger, H.; Laschewski, G.; Grätz, A. The perceived temperature – a versatile index for the assessment of the human thermal environment . Part A : scientific basics. *Int J Biometeorol* **2012**, 165–176.

87. Golasi, I.; Salata, F.; de Lieto Vollaro, E.; Coppi, M. Complying with the demand of standardization in outdoor thermal comfort: a first approach to the Global Outdoor Comfort Index (GOCI). *Build. Environ.* **2018**, *130*, 104–119.

88. Lai, D.; Lian, Z.; Liu, W.; Guo, C.; Liu, W.; Liu, K.; Chen, Q. A comprehensive review of thermal comfort studies in urban open spaces. *Sci. Total Environ.* **2020**, *742*, 140092.

89. Modest, M.F. *Radiative Heat Transfer*; 1993.

90. Matzarakis, A.; Rutz, F.; Mayer, H. Modelling radiation fluxes in simple and complex environments: Basics of the RayMan model. *Int. J. Biometeorol.* **2010**, *54*, 131–139.

91. Verein Deutscher Ingenieure VDI 3787. In; 2008 ISBN 5662422001.

92. Hoppe, P.; Mayer, H. Planungsrelevante Bewertung der thermischen Komponente des Stadtklimas. *Landschaft und Stadt* **1987**, *19*, 22–30.

93. Krayenhoff, E.S.; Voogt, J.A. A microscale three-dimensional urban energy balance model for studying surface temperatures. **2007**, 433–461.

94. Huang, J.; Cedeño-Laurent, J.G.; Spengler, J.D. CityComfort+: A simulation-based method for predicting mean radiant temperature in dense urban areas. *Build. Environ.* **2014**, *80*, 84–95.

95. Mitraka, Z.; Chrysoulakis, N.; Doxani, G.; Frate, F. Del; Berger, M. Urban Surface Temperature Time Series Estimation at the Local Scale by Spatial-Spectral Unmixing of Satellite Observations. **2015**, 4139–4156.

96. Chrysoulakis, N.; Grimmond, S.; Feigenwinter, C.; Lindberg, F.; Gastellu-Etchegorry, J.P.; Marconcini, M.; Mitraka, Z.; Stagakis, S.; Crawford, B.; Olofson, F.; et al. Urban energy exchanges monitoring from space. *Sci. Rep.* **2018**, *8*, 1–8.

97. Morrison, W.; Yin, T.; Lauret, N.; Guilleux, J.; Kotthaus, S.; Gastellu-etchegorry, J.; Norford, L.; Grimmond, S. Remote Sensing of Environment Atmospheric and emissivity corrections for ground-based thermography using 3D radiative transfer modelling. *Remote Sens. Environ.* **2020**, *237*, 111524.

98. Landier, L.; Al Bitar, A.; Lauret, N.; Gastellu-Etchegorry, J.P.; Aubert, S.; Mitraka, Z.; Feigenwinter, C.; Parlow, E.; Heldens, W.; Kotthaus, S.; et al. 3D modeling of radiative transfer and energy balance in urban canopies combined to remote sensing acquisitions. *Int. Geosci. Remote Sens. Symp.* **2016**, *2016-Novem*, 6738–6741.

99. Chen, Y.; Chen, C.; Matzarakis, A.; Liu, J.; Lin, T. Modeling of mean radiant temperature based on comparison of airborne remote sensing data with surface measured data. *Atmos. Res.* **2016**,

174–175, 151–159.

100. Gastellu-Etchegorry, J.P.; Martin, E.; Gascon, F. DART: A 3D model for simulating satellite images and studying surface radiation budget. *Int. J. Remote Sens.* **2004**, *25*, 73–96.

101. Béland, M.; Widlowski, J.L.; Fournier, R.A. A model for deriving voxel-level tree leaf area density estimates from ground-based LiDAR. *Environ. Model. Softw.* **2014**, *51*, 184–189.

102. Richardson, J.J.; Moskal, L.M.; Kim, S. Modeling approaches to estimate effective leaf area index from aerial discrete-return LIDAR. *Agric. For. Meteorol.* **2009**, *149*, 1152–1160.

103. Zheng, G.; Ma, L.; Eitel, J.U.H.; He, W.; Magney, T.S.; Moskal, L.M.; Li, M. Retrieving Directional Gap Fraction, Extinction Coefficient, and Effective Leaf Area Index by Incorporating Scan Angle Information from Discrete Aerial Lidar Data. *IEEE Trans. Geosci. Remote Sens.* **2017**, *55*, 577–590.

104. Authority., S.L. *2014 Aerial LiDAR of Singapore*; **2014**.

105. Morrison, W.; Kotthaus, S.; Grimmond, C.S.B.; Inagaki, A.; Yin, T.; Gastellu-Etchegorry, J.P.; Kanda, M.; Merchant, C.J. A novel method to obtain three-dimensional urban surface temperature from ground-based thermography. *Remote Sens. Environ.* **2018**, *215*, 268–283.

106. Meili, N.; Manoli, G.; Burlando, P.; Bou-Zeid, E.; Chow, W.T.L.; Coutts, A.M.; Daly, E.; Nice, K.A.; Roth, M.; Tapper, N.J.; et al. An urban ecohydrological model to quantify the effect of vegetation on urban climate and hydrology (UT&C v1.0). *Geosci. Model Dev.* **2020**, *13*, 335–362.

107. Holmer, B.; Lindberg, F.; Rayner, D.; Thorsson, S. How to transform the standing man from a box to a cylinder – a modified methodology to calculate mean radiant temperature in field studies and models. **2015**.

108. Dirmhirn, I. *Das Strahlungsfeld im Lebensraum*; Akademische Verlagsgesellschaft: Frankfurt, **1964**.

109. Höppe, P. *Die Energiebilanz des Menschen*; Universitat Munchen, Meteorologisches Institut: Munich, Germany, **1984**; Volume 49.

110. Höppe, P. Ein neues Verfahren zur Bestimmung der mittleren Strahlungstemperatur in Freien. *Wetter und Leb.* **1992**, *44*, 147–151.

111. Kipp & Zonen *Instruction manual for Kipp & Zonen CNR 4 net radiometer*; **2008**.

112. Vaisala User Guide Vaisala Weather Transmitter WXT530 Series. **2017**.

113. Campbell Scientific *BlackGlobe Temperature Sensor for Heat Stress user Manual*; **2015**.

114. Y. Wang, J. Grimaldi, L. Landier, E. Chavanon, J.P.G.-E. Introduction of clouds in DART model. *Int. Arch. Photogramm.* **2020**, *XLIII*, 843–848.

115. Kotthaus, S.; Smith, T.E.L.; Wooster, M.J.; Grimmond, C.S.B. ISPRS Journal of Photogrammetry and Remote Sensing Derivation of an urban materials spectral library through emittance and reflectance spectroscopy. *ISPRS J. Photogramm. Remote Sens.* **2014**, *94*, 194–212.

116. Gastellu-Etchegorry, J.P. 3D modeling of satellite spectral images, radiation budget and energy budget of urban landscapes. *Meteorol. Atmos. Phys.* **2008**, *102*, 187–207.

117. Skidmore, A.K.; Coops, N.C.; Neinavaz, E.; Ali, A.; Schaepman, M.E.; Paganini, M.; Kissling, W.D.; Vihervaara, P.; Darvishzadeh, R.; Feilhauer, H.; et al. Priority list of biodiversity metrics to observe from space. *Nat. Ecol. Evol.* **2021**, *5*, 896–906.

118. Zheng, Z.; Zeng, Y.; Schneider, F.D.; Zhao, Y.; Zhao, D.; Schmid, B.; Schaepman, M.E.; Morsdorf, F. Mapping functional diversity using individual tree-based morphological and physiological traits in a subtropical forest. *Remote Sens. Environ.* **2021**, *252*, 112170.

119. Wojnowski, W.; Wei, S.; Li, W.; Yin, T.; Li, X.X.; Ow, G.L.F.; Yusof, M.L.M.; Whittle, A.J. Comparison of absorbed and intercepted fractions of PAR for individual trees based on radiative transfer model simulations. *Remote Sens.* **2021**.

120. McGee, J.; Day, S.; Wynne, R.; White, B. Using Geospatial Tools to Assess the Urban Tree Canopy : Decision Support for Local Governments. **2012**.

121. Ucar, Z.; Bettinger, P.; Merry, K.; Akbulut, R.; Siry, J. Urban Forestry & Urban Greening Estimation of urban woody vegetation cover using multispectral imagery and LiDAR. *Urban For. Urban Green.* **2018**, *29*, 248–260.

122. Parmehr, E.G.; Amati, M.; Taylor, E.J.; Livesley, S.J. Estimation of urban tree canopy cover using random point sampling and remote sensing methods. *Urban For. Urban Green.* **2016**, *20*, 160–171.

123. Erker, T.; Wang, L.; Lorentz, L.; Stoltman, A.; Townsend, P.A. Remote Sensing of Environment A statewide urban tree canopy mapping method. *Remote Sens. Environ.* **2019**, *229*, 148–158.

124. Wagner, F.H.; Ferreira, M.P.; Sanchez, A.; Hirye, M.C.M.; Zortea, M.; Gloor, E.; Phillips, O.L.; de Souza Filho, C.R.; Shimabukuro, Y.E.; Aragão, L.E.O.C. Individual tree crown delineation in a highly diverse tropical forest using very high resolution satellite images. *ISPRS J. Photogramm. Remote Sens.* **2018**, *145*, 362–377.

125. Miraki, M.; Sohrabi, H.; Fatehi, P.; Kneubuehler, M. Individual tree crown delineation from high-resolution UAV images in broadleaf forest. *Ecol. Inform.* **2021**, *61*, 101207.

126. Alonzo, M.; Bookhagen, B.; Roberts, D.A. Urban tree species mapping using hyperspectral and lidar data fusion. *Remote Sens. Environ.* **2014**, *148*, 70–83.

127. Yao, W.; Krull, J.; Krzystek, P.; Heurich, M. Sensitivity analysis of 3D individual tree detection from LiDAR point clouds of temperate forests. *Forests* **2014**, *5*, 1122–1142.

128. Zhen, Z.; Quackenbush, L.J.; Zhang, L. Trends in automatic individual tree crown detection and delineation-evolution of LiDAR data. *Remote Sens.* **2016**, *8*, 1–26.

129. Chenari, A.; Erfanifard, Y.; Dehghani, M.; Pourghasemi, H.R. Woodland mapping at single-tree levels using object oriented classification of unmanned aereal veihcle (UAV) images. **2017**, *XLII*, 7–10.

130. Feng, X.; Li, P. A Tree Species Mapping Method from UAV Images over Urban Area Using Similarity in Tree-Crown Object Histograms. **2019**.

131. Baena, S.; Moat, J.; Whaley, O.; Boyd, D.S. Identifying species from the air : UAVs and the very high resolution challenge for plant conservation. **2017**, 1–21.

132. Baatz, M.; Schape, A. Multiresolution Segmentation : an optimization approach for high quality multi-scale image segmentation. **2000**.

133. Dalponte, M.; Frizzera, L.; Gianelle, D. Individual tree crown delineation and tree species classification with hyperspectral and LiDAR data. *PeerJ* **2019**.

134. Dalponte, M.; Reyes, F.; Kandare, K.; Gianelle, D. Delineation of individual tree crowns from ALS and hyperspectral data: A comparison among four methods. *Eur. J. Remote Sens.* **2015**, *48*, 365–382.

135. Kattenborn, T.; Leitloff, J.; Schiefer, F.; Hinz, S. Review on Convolutional Neural Networks (CNN) in vegetation remote sensing. *ISPRS J. Photogramm. Remote Sens.* **2021**, *173*, 24–49.

136. Lee, J.; Cai, X.; Lellmann, J.; Dalponte, M.; Malhi, Y.; Butt, N.; Morecroft, M.; Schonlieb, C.B.; Coomes, D.A. Individual Tree Species Classification from Airborne Multisensor Imagery Using Robust PCA. *IEEE J. Sel. Top. Appl. Earth Obs. Remote Sens.* **2016**, *9*, 2554–2567.

137. Sun, W.; Du, Q. Hyperspectral band selection: A review. *IEEE Geosci. Remote Sens. Mag.* **2019**, *7*, 118–139.

138. Weinstein, B.G.; Marconi, S.; Bohlman, S.A.; Zare, A.; Singh, A.; Graves, S.J.; White, E.P. A remote sensing derived data set of 100 million individual tree crowns for the national ecological observatory network. *Elife* **2021**, *10*, 1–18.

139. Brandt, M.; Tucker, C.J.; Kariryaa, A.; Rasmussen, K.; Abel, C.; Small, J.; Chave, J.; Rasmussen, L.V.; Hiernaux, P.; Diouf, A.A.; et al. An unexpectedly large count of trees in the West African Sahara and Sahel. *Nature* **2020**, *587*, 78–82.

140. Torres, D.L.; Feitosa, R.Q.; Happ, P.N.; La Rosa, L.E.C.; Junior, J.M.; Martins, J.; Bressan, P.O.; Gonçalves, W.N.; Liesenberg, V. Applying fully convolutional architectures for semantic segmentation of a single tree species in urban environment on high resolution UAV optical imagery. *Sensors (Switzerland)* **2020**, *20*, 1–20.

141. Dos Santos, A.; Junior, J.M.; Araújo, M.S.; Robledo, D.; Martini, D.; Tetila, E.C.; Siqueira, H.L.; Aoki, C.; Eltner, A.; Matsubara, E.T.; et al. Assessment of CNN-Based Methods for Individual Tree Detection on Images Captured by RGB Cameras Attached to UAVs. **2019,** 1–11.

142. Li, Y.; Zhang, H.; Xue, X.; Jiang, Y.; Shen, Q. Deep learning for remote sensing image classification : A survey. **2018**, 1–17.

143. Li, W.; Fu, H.; Yu, L.; Cracknell, A. Deep Learning Based Oil Palm Tree Detection and Counting for High-Resolution Remote Sensing Images. Remote Sens. **2017**, *9*, 22..

144. Weinstein, B.G.; Marconi, S.; Bohlman, S.; Zare, A.; White, E. Individual Tree-Crown Detection in RGB Imagery Using Semi-Supervised Deep Learning Neural Networks. **2019**, 1–13.

145. Natesan, S.; Armenakis, C.; Vepakomma, U.; Engineering, G.; Science, S. RESNET-Based tree species classification using UAV images. **2019**, *XLII*, 10–14.

146. Reichstein, M.; Camps-Valls, G.; Stevens, B.; Jung, M.; Denzler, J.; Carvalhais, N.; Prabhat Deep learning and process understanding for data-driven Earth system science. *Nature* **2019**, *566*, 195–204.

147. Chen, L.; Papandreou, G.; Member, S.; Kokkinos, I.; Murphy, K.; Yuille, A.L. DeepLab : Semantic Image Segmentation with Deep Convolutional Nets , Atrous Convolution , and Fully Connected CRFs. **2017,** 1–14.

148. Ronneberger, O.; Fischer, P.; Brox, T. U-Net Convolutional Networks for Biomedical Image Segmentation.; **2015**.

149. Badrinarayanan, V.; Handa, A.; Cipolla, R. SegNet: A Deep Convolutional Encoder-Decoder Architecture for Robust Semantic Pixel-Wise Labelling. **2015**.

150. Jegou, S.; Drozdzal, M.; Vazquez, D.; Romero, A.; Bengio, Y. The One Hundred Layers Tiramisu : Fully Convolutional DenseNets for Semantic Segmentation. **2017**.

151. Fricker, G.A.; Ventura, J.D.; Wolf, J.A.; North, M.P.; Davis, F.W.; Franklin, J. A convolutional neural network classifier identifies tree species in mixed-conifer forest from hyperspectral

imagery. *Remote Sens.* **2019**, *11*.

152. Kattenborn, T.; Eichel, J.; Fassnacht, F.E. Convolutional Neural Networks enable efficient , accurate and fine- grained segmentation of plant species and communities from high-resolution UAV imagery. *Sci. Rep.* **2019**, 1–9.

153. Jiang, S.; Yao, W.; Heurich, M. Dead wood detection based on semantic segmentation of VHR Aerial CIR imagery using optimized FCN-DENSENET. **2019**, *XLII*, 18–20.

154. Liu, L.; Coops, N.C.; Aven, N.W.; Pang, Y. Mapping urban tree species using integrated airborne hyperspectral and LiDAR remote sensing data. *Remote Sens. Environ.* **2017**, *200*, 170–182.

155. Hartling, S.; Sagan, V.; Sidike, P.; Maimaitijiang, M.; Carron, J. Urban tree species classification using a worldview-2/3 and liDAR data fusion approach and deep learning. *Sensors (Switzerland)* **2019**, *19*, 1–23.

156. Wallace, L.; Sun, Q. (Chayn); Hally, B.; Hillman, S.; Both, A.; Hurley, J.; Martin Saldias, D.S. Linking urban tree inventories to remote sensing data for individual tree mapping. *Urban For. Urban Green.* **2021**, *61*, 127106.

157. Braga, J.R.G.; Peripato, V.; Dalagnol, R.; Ferreira, M.P.; Tarabalka, Y.; Aragão, L.E.O.C.; de Campos Velho, H.F.; Shiguemori, E.H.; Wagner, F.H. Tree crown delineation algorithm based on a convolutional neural network. *Remote Sens.* **2020**, *12*, 1–27.

158. Chiang, C.; Barnes, C.; Angelov, P.; Jiang, R. Deep Learning-Based Automated Forest Health Diagnosis From Aerial Images. **2020**, *8*.

159. He, K.; Gkioxari, G.; Dollar, P.; Girshick, R. Mask R-CNN. *Proc. IEEE Int. Conf. Comput. Vis.* **2017**, *2017-Octob*, 2980–2988.

160. Yu, K.; Hao, Z.; Post, C.J.; Mikhailova, E.A.; Lin, L.; Zhao, G.; Tian, S.; Liu, J. Comparison of Classical Methods and Mask R-CNN for Automatic Tree Detection and Mapping Using UAV Imagery. *Remote Sens.* **2022**, *14*.

161. Hickman, S.H.M.; Ball, J.G.C.; Jackson, T.D.; Koay, X.J.; Hirst, J.; Jay, W.; Aubry-Kientz, M.; Vincent, G.; Coomes, D.A. Accurate tropical forest individual tree crown delineation from RGB imagery using Mask R-CNN. *bioRxiv* **2022**, 2022.07.10.499480.

162. Najman, L.; Schmitt, M. Watershed of a Continuous Function To cite this version : HAL Id : hal-00622129. **2014**, *38*, 99–112.

163. Mills, G. Urban climatology: History, status and prospects. *Urban Clim.* **2014**, *10*, 479–489.

164. Yang, A.S.; Juan, Y.H.; Wen, C.Y.; Chang, C.J. Numerical simulation of cooling effect of vegetation enhancement in a subtropical urban park. *Appl. Energy* **2017**, *192*, 178–200.

165. Meili, N.; Acero, J.A.; Peleg, N.; Manoli, G.; Burlando, P.; Fatichi, S. Vegetation cover and plant-trait effects on outdoor thermal comfort in a tropical city. *Build. Environ.* **2021**, *195*, 107733.

166. Fang, H.; Li, S.; Zhang, Y.; Wei, S.; Wang, Y. New insights of global vegetation structural properties through an analysis of canopy clumping index, fractional vegetation cover, and leaf area index. *Sci. Remote Sens.* **2021**, *4*, 100027.

167. Acero, J.A.; Dissegna, A.; Tan, Y.S.; Tan, A.; Norford, L.K. Outdoor performance of the black globe temperature sensor on a hot and humid tropical region. *Environ. Technol. (United Kingdom)* **2023**, *44*, 961–973.

168. Middel, A.; Nazarian, N.; Demuzere, M.; Bechtel, B. Urban Climate Informatics: An Emerging Research Field. *Front. Environ. Sci.* **2022**, *10*, 1–15.

169. Ghamisi, P.; Member, S.; Rasti, B.; Yokoya, N.; Wang, Q.; Bernhard, H.; Bruzzone, L.; Bovolo, F.; Member, S.; Atkinson, P.M. Multisource and Multitemporal Data Fusion in Remote Sensing. **2018**.

170. Xu, H.; Wang, C.C.; Shen, X. 3D Tree Reconstruction in Support of Urban Microclimate. **2021**.

171. Caliot, C.; Schoetter, R.; Forest, V.; Eymet, V.; Chung, T. Model of Spectral and Directional Radiative Transfer in Complex Urban Canopies with Participating Atmospheres. *Boundary-Layer Meteorol.* **2023**, *186*, 145–175.

172. Alvarez-Vanhard, E.; Corpetti, T.; Houet, T. UAV & satellite synergies for optical remote sensing applications: A literature review. *Sci. Remote Sens.* **2021**, *3*, 100019.

173. Verrelst, J.; Malenovský, Z.; Van der Tol, C.; Camps-Valls, G.; Gastellu-Etchegorry, J.P.; Lewis, P.; North, P.; Moreno, J. Quantifying Vegetation Biophysical Variables from Imaging Spectroscopy Data: A Review on Retrieval Methods. *Surv. Geophys.* **2019**, *40*, 589–629.

174. Wang, T.; Gan, V.J.L. Automated joint 3D reconstruction and visual inspection for buildings using computer vision and transfer learning. *Autom. Constr.* **2023**, *149*, 104810.

175. Zhang, Y.; Zhang, C.; Chen, S.; Chen, X. Automatic reconstruction of building façade model from photogrammetric mesh model. *Remote Sens.* **2021**, *13*.

176. Rodríguez-santiago, A.L.; Arias-aguilar, J.A.; Takemura, H. A Deep Learning Architecture For 3D Mapping Urban Landscapes. **2021**.

177. Al Bitar, A.; Landier, L.; Guilleron, J.; Lauret, N.; Gastellu-Etchegorry, J.P.; Tiangang, Y.; Feigenwinter, C.; Mitraka, Z.; Chrysoulakis, N. Assessing Urban canopies 3D radiative and Energy Budgets with remote sensing and DART model. *2017 Jt. Urban Remote Sens. Event, JURSE 2017* **2017**, 1–5.

178. Ammar, A.; Koubaa, A.; Benjdira, B. Deep-learning-based automated palm tree counting and geolocation in large farms from aerial geotagged images. Agronomy. **2021**;11(8).

179. Ocer, N.E.; Kaplan, G.; Erdem, F.; Kucuk Matci, D.; Avdan, U. Tree extraction from multi-scale UAV images using Mask R-CNN with FPN. Remote Sens Lett. **2020**;11(9):847–56.

180. Zamboni, P.; Junior, J.M.; Silva, J.A.; Miyoshi, G.T.; Matsubara, E.T.; Nogueira, K. et al. Benchmarking anchor-based and anchor-free state-of-the-art deep learning methods for individual tree detection in rgb high-resolution images. Remote Sens. **2021**;13(13).

181. Braga, J.R.G.; Peripato, V.; Dalagnol, R.; Ferreira, M.P.; Tarabalka, Y.; Aragão, L.E.O.C. et al. Tree crown delineation algorithm based on a convolutional neural network. Remote Sens. **2020**;12(8).

182. Weinstein, B.G.; Marconi, S.; Bohlman, S.; Zare, A.; White, E. Individual tree-crown detection in rgb imagery using semi-supervised deep learning neural networks. Remote Sens. **2019**;11(11).

183. Salliou, N.; Arborino, T.; Nassauer, J.I.; Salmeron, D.; Urech, P.; Vollmer, D.; Grêt-Regamey, A. Science-design loop for the design of resilient urban landscapes. *Socio-Environmental Syst. Model.* **2023**, *5*, 18543.

184. Fung, T.K.; Richards, D.R.; Leong, R.A.T.; Ghosh, S.; Tan, C.W.J.; Drillet, Z.; Leong, K.L.; Edwards, P.J. Litter decomposition and infiltration capacities in soils of different tropical

urban land covers. *Urban Ecosyst.* **2022**, *25*, 21–34.

185. Song, X.P.; Richards, D.R.; Tan, P.Y. Using social media user attributes to understand human–environment interactions at urban parks. *Sci. Rep.* **2020**, *10*, 1–11.

186. Song, X.P.; Richards, D.R.; He, P.; Tan, P.Y. Does geo-located social media reflect the visit frequency of urban parks? A city-wide analysis using the count and content of photographs. *Landsc. Urban Plan.* **2020**, *203*, 103908.

187. Drillet, Z.; Fung, T.K.; Leong, R.A.T.; Sachidhanandam, U.; Edwards, P.; Richards, D. Urban vegetation types are not perceived equally in providing ecosystem services and disservices. *Sustain.* **2020**, *12*.

188. Bartesaghi Koc, C.; Osmond, P.; Peters, A. Evaluating the cooling effects of green infrastructure: A systematic review of methods, indicators and data sources. *Sol. Energy* **2018**, *166*, 486–508.

189. Irfeey, A.M.M.; Chau, H.W.; Sumaiya, M.M.F.; Wai, C.Y.; Muttil, N.; Jamei, E. Sustainable Mitigation Strategies for Urban Heat Island Effects in Urban Areas. *Sustain.* **2023**, *15*.

8. Acknowledgements

This research was carried out within the "Ecosystem Services in Urban Landscapes" research group of the "Future Cities Laboratory" at the Singapore-ETH Centre with close collaboration with Singapore-MIT Alliance for Research and Technology (SMART, Singapore).